Mixtures of Multipoles—Should They Be in Your EM Toolbox?

RICHARD W. ZIOLKOWSKI (Life Fellow, IEEE)

Global Big Data Technologies Centre, School of Electrical and Data Engineering, University of Technology Sydney, Ultimo, NSW 2007, Australia

CORRESPONDING AUTHOR: R. W. ZIOLKOWSKI (e-mail: richard.ziolkowski@uts.edu.au)

ABSTRACT Multipole expansions are an essential analysis tool in the foundations of the descriptions of the electromagnetic fields radiated by electric and magnetic sources. Nevertheless, practical antenna systems generally rely on them as an academic explanation, not as a fundamental building block. An overview of the recent surge in interest in multipole sources and their fields to achieve useful radiated and scattered fields with, for example, high directivities in preferred directions is given. Topics include Huygens sources, dielectric-based Mie-tronics, edge-singularity multipoles, and exotic metamaterial-inspired superdirective lenses and radiators. While there has been a never-ending stream of physics publications, little has happened in the engineering electromagnetics community. I will try to answer the title with examples that may stimulate interest in the field.

INDEX TERMS Antennas, antenna theory, directive antennas, electromagnetics, electromagnetic fields.

I. INTRODUCTION

AS WE continue to move into researching and fielding yet newer and newer generations of wireless technologies, i.e., fifth-generation (5G) [1]–[3], sixth-generation (6G) [4], [5], and now even beyond [6], [7], the importance of high directivity beams to ensure meeting their anticipated performance characteristics has increased significantly. Not only base station systems, but also user terminals must now consider antennas with higher and higher directivities to compensate for the requirements for reduced physical power, increased propagation losses faced at higher frequencies, and low probability of intercept (LPI) to attain secure communications. They represent the key antenna technology for supporting high data transmission rates, improved signal-to-interference-plus-noise ratios, increased spectral and energy efficiencies, and versatile beam shaping and pointing. Thus, they hold the great promise of serving as critical infrastructure that will enable future wireless ecosystems.

Information transfer technologies in general are a critical main focus for many researchers in academia, industry and government. However, there remain many other applied electromagnetics efforts that would benefit from similar advances in performance characteristics of radiating and scattering systems in addition to the next mobile, hand-held communications platform. Whether it is battery-free environments; embedded sensor networks and other remote sensing elements; energy storage and delivery systems; or simply person/product identification elements for medical/shipping purposes, it is critical to tailor the spatial and temporal distributions of the electromagnetic (EM) fields that facilitate these applications to achieve high performance with both low energy consumption and cost.

One straightforward strategy to achieve highly directive, narrow beams is to employ arrays of significant size. In particular, let the radiating system be either an aperture antenna (continuous current distribution) whose effective area is A_{eff} or an array of radiating elements (set of discrete currents) distributed in A_{eff}. If the total efficiency (i.e., taking into account the material losses, mis-match losses, polarization mis-match, ...) of the system is e_{total}, then its maximum gain, G_{max}, is related to its maximum directivity, D_{max}, as $G_{max} = e_{total} \times D_{max}$. Thus, if there are no losses, then the upper bound on the gain of the antenna system uniformly driven at the excitation wavelength λ is fundamentally related to its effective area, A_{eff} through its directivity as [8], [9]:

$$D_{\mathrm{3D,ub}} = 4\pi \frac{A_{eff}}{\lambda^2} \qquad (1)$$

Consequently, a larger effective aperture will provide a higher directivity. Note that if the aperture is circular with radius R, then $D_{3D,ub} = 4\pi(\pi R^2)/\lambda^2 = (kR)^2$ when kR is large. This expression for a uniformly illuminated circular aperture was first noted by Harrington [10], [11]. Recall as well that for a given aperture size, an antenna will deliver its largest directivity if it is uniformly excited. A typical electrically small dipole has a directivity of 1.76 dB and its half-wavelength counterpart only has a directivity of 2.16 dB. A simple half-wavelength linearly polarized microstrip patch and its much larger ground plane can readily obtain a directivity of 6 dB. On the other hand, a 10 m parabolic reflector operating at 3 GHz has a directivity of approximately 50 dB [9].

Eq. (1) also tells us immediately that moving to higher frequencies, i.e., to shorter wavelengths, for a specified aperture size also yields a higher directivity. The efforts on millimeter-wave (mmWave) systems to meet 5G and beyond promised features immediately benefit from this fact. Moreover, if the aperture is enclosed in a minimum sphere of radius a, then the half-power (3-dB) beamwidth of its main beam is proportional to $\lambda/(2a)$. Thus, a smaller wavelength also yields a smaller width of its main beam for a given aperture size.

There is yet another manner in which to achieve higher directivities. As has been shown by a number of authors, e.g., [12]–[14], the fields in a region of free space outside of a spherical surface that encloses all of the electric and magnetic currents driven at a specific frequency can be expanded in a series of electric and magnetic multipole fields represented by (vector) spherical harmonics. In particular, their three-dimensional (3D) electromagnetic fields in that exterior region can be expressed in terms of a series of orthogonal basis wave functions of the form $h_\ell^{(2)}(kr)\,Y_\ell^m(\theta,\phi)$, where $h_\ell^{(2)}(kr)$ is the spherical Hankel function of the second kind and order ℓ, and $Y_\ell^m(\theta,\phi)$ is the associated Legendre polynomial of degree ℓ and order m and where $1 \leq \ell \leq \infty$ and $|m| \leq \ell$. Then, as shown by Harrington [10], [11], if these sources can only produce multipoles of significant amplitude up to order N, the maximum directivity that can be obtained and, hence, gain when there are no losses, is

$$D_{N,\max}^{3D} = N^2 + 2N \qquad (2)$$

This limit is obtained when the electric and magnetic multipoles of order N occur at the same frequency. Therefore, by properly exciting higher order modes, one can in principle achieve very high directivities from a fixed source region.

Harrington [10], [11] postulated that if all the sources are contained within a sphere of minimum radius a cannot support the large magnitudes associated with the wave functions with $ka > N$, those higher order multipoles (HOMs) cannot be accessed effectively. The maximum directivity is then readily associated with the wave function properties and the antenna size by taking the highest order multipole

as $N = ka$. It then takes the form:

$$D_{\max} = (ka)^2 + 2\,ka \qquad (3)$$

It is noted that the identification of $N = ka$ has been considered from several points of view. One can treat the enclosing sphere as a waveguide in which $ka = N$ is the cutoff between propagating and evanescent spherical modes [15]. One can also consider $a = N/k$ as representing the maximal extent of the important reactive fields [16]. Moreover, it was recognized [16] that R of the significant reactive fields of an antenna (or scatterer) is the same as the radius of the maximum possible effective area of the antenna (or the radius of the maximum possible total scattering cross section of a scatterer). This effective radius can be much larger than that of the sphere circumscribing the physical antenna (scatterer) for resonant antennas (scatterers). This physical effect was discussed in regards to light capture by a particle in [17], [18] and has been recognized in many other scenarios such in electrically small wireless power transfer (WPT) rectennas [19]. It can be argued that this enhanced total scattering cross-section of a resonant scatterer or receiving capture area of a rectenna is obtained by their interactions with both the fundamental and higher order spherical harmonic modes present in the incident field which locally stimulate its own fundamental and HOMs. Most of these stimulated modes simply reside near the intended target and do not effectively convert the incident energy into fields that would propagate away from the sources induced in them, i.e., many of these HOMs represent the reactive fields of the target. The HOMs would have little impact on their responses if the incident beam were strictly truncated to the physical size of the scatterer, i.e., the target would then have restricted access to them.

This connection between the reactive fields and an antenna's directivity follows naturally if one recalls that the lower bound on the quality factor derived by Chu [20] takes the form [21]:

$$Q_{Chu} = \frac{1}{(ka)^3} + \frac{1}{ka} \qquad (4)$$

Note that (4) is the value for a lossless system since if the efficiency of an antenna is η_{ant}, then its quality factor $Q = \eta_{ant} Q_{Chu}$ [22]. Because the 3-dB fractional bandwidth (FBW) is $FBW \sim 2/Q_{LB}$ [23], a high Q radiating system has a narrow bandwidth and, hence, is considered to have reactive fields of substantial extent.

Nevertheless, while (2) is well-founded, the bound (3) must be called into question at least when the antenna is electrically small [15]. It does not recover the known infinitesimal Huygens dipole antenna (HDA) result, i.e., with $N = 1$, $D_{\max} = 3$. As a consequence, there have been interesting heuristic derivations and discussions of the maximum directivity in relation to the electrical size of an antenna [15], [24], [25], particularly for non-superreactive antennas (e.g., not for superdirective antennas which generally have extremely high Q values) when taking into account

the radiation Q of the modes [26]. The main emphasis in the latter is the use of the radiation-Q of the spherical modes as a measure of how difficult it is to excite the HOMs in comparison to the lower-order ones. As will be discussed below, there are many superdirective HOM-based systems which demonstrate that these size-directivity bounds prove ineffective.

This article will emphasize the use of multipole concepts to achieve high directivities from radiating and scattering systems. As will be discussed in Section II, multipoles are being used in the physics and optics communities to describe and enhance the properties of metamaterials and passive and active nanophotonic systems. The rapid advance of optics-emphasized Mie-tronic systems that take advantage of both electric and magnetic multipoles is an example. Section III will briefly highlight those higher frequency systems having unidirectional properties. The discussion is then pointed back in Section IV to dipole-based antenna designs that have obtained unidirectional properties. In particular, the physics and engineering electromagnetics of HDAs are presented. Unidirectional multipole radiating systems are then considered in Section V. Both two- and three-dimensional concepts are explored. Several methods of designing multipole systems, e.g., wire, aperture-edge, and single-port based antennas, are described in Section VI. Their unique characteristics and potential advantages, as well as realistic cautionary issues associated with them, are emphasized. Superdirective multipole examples are presented in both Sections V and VI. Conclusions are given in Section VII.

In direct response to a reviewer's question, I am indeed surprised that the engineering electromagnetics community has not given more serious consideration to multipole-based structures to achieve the demand for systems with high directivity and other functionalities. As a result, the reader will actually experience a "quasi-review", i.e., not only will the noted topics be discussed and supported with many references, but several multipolar examples not published previously will also be presented. Their inclusion along with the review material hopefully serves a main purpose of this article – the hope that I can convince the reader that multipole concepts are indeed worth the time and efforts for consideration to address some of the insatiable high directivity goals of the NextG transmitting and receiving systems.

II. MULTIPOLE PHYSICS AND ENGINEERING

For many of us, we have learned of multipole expansions, i.e., cylindrical and spherical harmonic representations, of the electromagnetic fields radiated by finite sources and scattered by finite-sized objects when excited by an incident wave field in our graduate studies of advanced electromagnetic theory [9], [27]–[31]. This is particularly true when studying the canonical problems of the scattering of plane waves from metal and dielectric cylinders and spheres (Mie Theory). This classic EM approach with nearly a century of international contributions has been a foundational building block of understanding a variety of practical problems and

of developing the tools to model them. The practical applications are quite varied; they include, for example, radar cross sections [28], [32], [33], near-field scanning [34]–[36], back-door aperture coupling [37]–[41], material responses [42] and short-pulse driven antennas [43], [44]. On the other hand, the physics community is generally exposed to multipole analyses in classic texts such as [13]. It has recently rediscovered their usefulness and has embraced their application to a number of problems of current interest. For instance, several multipolar simulation software packages related to multipolar nanophotonics are now available [45], [46].

A. METAMATERIALS AND METASURFACES

Recall that a bulk metamaterial (MTM) could be described as a multilayered structure in which each layer consists of unit cells formed with metallic or dielectric inclusions in a dielectric background [47]. A metasurface (MTS) would then be described as a "single layer" of those unit cells [48]. While the unit cells were originally called by many different names, e.g., artificial molecules [49], [50], they are generally termed meta-atoms now. The responses of an excited meta-atom are either electric or magnetic or some combination of them.

To be considered as a metamaterial with homogenized effective electric and magnetic material properties, the unit cell size Λ should be $\Lambda \leq \lambda/10$. Consequently, the inclusions within the unit cell can be considered to be electrically small antennas/scatterers [51], [52]. Consequently, a majority of the analytical analyses of metamaterials in its first decade relied on electric and magnetic dipole approximations. However, as a more detailed understanding of the responses of a metamaterial were desired, it has become recognized that higher order terms can play a significant role.

Some early MTM works from the engineering electromagnetic community considered canonical-shaped structures involving double positive (DPS), double negative (DNG) and single negative (SNG), i.e., both epsilon negative (ENG) and mu negative (MNG), media using Mie-theory multipolar expansions to simply understand dipole and higher order mode physics associated with negative materials [53]–[56] and their potential antenna [57], super-scattering [53], [58]–[60], and cloaking [61] applications. Nevertheless, the majority characterized the response of more complex inclusions, unit cells, and the resulting MTMs with numerical computational electromagnetics (CEM) simulations, particularly for potential practical applications. The physics and optics communities began using multipolar field decompositions to analyze the electric and magnetic responses of isolated meta-atoms, mainly simple and complex shaped nanoparticles in a host dielectric medium, in more detail [62], [63] for the design and characterization of terahertz (THz) and optical meta-structures. There has even been a return to the transition matrix (T-matrix) approach [64] to describe the scattering from arbitrarily shaped particles [65]. As metasurfaces evolved

as the more practical MTM topic, multipolar analyses of general hybrid metal–dielectric MTSs and their scattering responses [66], [67] and Huygens MTSs in particular [68] have proven quite useful.

B. PASSIVE NANOPHOTONICS

Aside from the *Gedankenexperiment* known as the perfect lens [69] that was the focus of much early MTM research, one major optical MTM property that has drawn continued, significant interest is the realization of metamaterial-inspired magnetic responses at optical frequencies [70]. Because of very small wavelengths at visible frequencies, the meta-atoms of optical MTMs and MTSs are generally nano-particles (NPs). The multipolar approach has been used to understand the early use of metallic and other nano-antenna/nano-scatterer NP-based inclusions tailored for this purpose [71]. Several recent reviews of the effectiveness of the multipolar analysis approach for nanophotonic applications exist and include, for instance, [72], [73].

Because of the large losses associated with metals at optical frequencies, the use of high dielectric constant (HDC) materials to achieve magnetic responses has taken on a research life of its own. The advantages of dielectric-only-based metamaterials in comparison to their metallic counterparts at optical frequencies also include the better potential for fabrication. After the recognition [74] that a periodic array of magneto-dielectric spheres could achieve DNG properties, several first uses of Mie theory and the resonances it predicts to model the responses arising in HDC spheres based on polaritonic and plasmonic media were used to model and understand THz, infrared (IR) and optical MNG MTMs [75], [76]. Related MNG and DNG MTM and MTS studies based on Mie resonances with dielectric-only materials also were reported in the microwave and then millimeter wave, THz, and optical regimes [77]–[81].

Recall that a wavelength λ_0 in free-space becomes $\lambda_m = \lambda_0/\sqrt{\varepsilon_r}$ in a dielectric medium with relative permittivity ε_r. One of the detrimental issues of the original considerations of the microwave versions of dielectric-only resonators in the MTM/MTS designs was the need for extremely large dielectric constants (several $10's$ [77] to even $1000's$ [78]) to facilitate the unit cell sizes required to make the meta-structure thin or compact enough for a practical application. Because of the larger loss tangents of HDC materials generally, the net outcome was a meta-structure with large intrinsic losses. The difference between the microwave and optical systems is this spatial scale issue. At optical frequencies, there are a number of materials with dielectric constants on the order of 10 with very small loss tangents, e.g., the relative permittivity of silicon (Si) (the usual choice) and gallium arsenide (GaAs) (another typical one) [82] at 1.0 μm is 12.76 - j 0.0036 and 12.06–j 0, respectively. Because the size of optical nanoparticles can be physically much smaller than the wavelength, their use as scatterers alone or as inclusions in a unit cell does not suffer the same dramatic loss issue. As noted, dielectric losses are significantly less than

metallic ones at optical frequencies. On the other hand, multipolar meta-structure examples where the losses are desirable include, for example, color displays [83], high-Q filters [84] and perfect absorbers [67], [85].

C. ACTIVE NANOPHOTONICS

Because of the large losses associated with metals at optical frequencies, there have been a number of works that have investigated the inclusion of gain media in meta-structures to overcome them [86]–[92]. My students, collaborators and I have used the multipolar approach to consider the scattering and radiating responses of canonical core-shell and other multilayered spherical [86], [93]–[97], and circular cylindrical [98]–[100] nanoparticles with and without gain material embedded in them. They have been based primarily on combinations of ENG (metals at optical frequencies) and DPS (dielectrics) substrates. They have been excited by plane waves, by line sources, and by Hertzian dipoles to mimic actual quantum emitters. The approach has been extended to elliptical cylinders [101]. Much of this work has been reviewed recently in [99], [102].

Related meta-applications modeled with the multipolar approach have been quite varied. They include active optical MTMs [103], quantum emitters coupled with nanowire optical antennas [104], and nonlinear responses of optical meta-structures [105]–[107],

D. MIE-TRONICS

Interest in all-dielectric multipolar results at optical frequencies based on combinations of electric and magnetic resonances has surged in the last decade. Since many of the basic inclusions have been spherical or cylindrical in shape and they have been excited with plane waves or Hertzian dipoles, Mie theory analyses have been at the forefront of describing the physics of their resonant responses. Reports have addressed their meta-properties, both linear and nonlinear, and their subsequent meta-applications, e.g., [82], [105], [107]–[113]. In fact, a large segment of the physics and optics meta-communities has even adopted the term "Mie-tronics" [114] in analogy with the "meta-tronics" label [115], [116].

While the use of meta-atoms allows one to engineer magnetic permeability and subsequent responses by achieving strong resonances in meta-structures made from nonmagnetic materials, it is also possible to engineer the spatial and temporal dispersion and nonlocal effects as well. Another key difference between using HDC materials rather than metals and semiconductors to manipulate light at the nanoscale is that the deep-subwavelength nanostructures made from them can support a large number of different resonances. Moreover, their properties can be tailored because of their sensitivities to the geometries of the meta-structures. Consequently, there are more new terms often used these days rather than simply signifying MTMs and relying on average/effective parameters, including meta-optics or meta-photonics.

Furthermore, there are many terms being used to describe simply the presence of several nearby, overlapping strong and weak resonances and the subsequent physical effects arising from them. They include, for instance, Fano resonances and anapoles, the latter being closely linked to toroidal multipoles, e.g., [117]–[121]. However, it has been rather conclusively shown that toroidal multipoles are higher order corrections in the long wavelength approximation of the exact multipoles and that there are no independent toroidal degree of freedom in electromagnetics. Thus, there are no spectroscopic resonances of a "new third kind" [73], [122].

E. COMBINED MULTIPOLAR EFFECTS

Electric and magnetic multipole interferences have attracted a lot of interest in the last decade, particularly in conjunction with Mie-tronics and the recognition that extraordinary performance can be obtained. Huygens MTSs are combinations of tiny, properly designed electric and magnetic elements whose scattered field interfere to yield "zero" backscattering or forward scattering. Even though the HOMs are more sensitive to the geometries of optical nanostructures and have narrower bandwidths, their combinations yield useful physics that can be engineered to attain wave front shaping, beam control, and scattering enhancements/mitigation. The HOM effects have been considered in both single particle [123]–[126] and particle arrays in the form of MTSs [66], [67], [113], [127]–[130]. One common aspect of many of these investigations has been to achieve high directivity.

III. DIRECTIONAL MULTIPOLAR HIGHER FREQUENCY FIELDS

The interference of the fields arising from combinations of electric and magnetic dipole and HOMs has led to a number of very interesting studies of controlling the fields radiated from or scattered by nano-structures. The engineering electromagnetics community [9], [131], [132] originally recognized the combination of independently driven electric dipole and loop (magnetic dipole) antennas as a Huygens source primarily as an ideal feed for parabolic reflector antennas. Similarly, higher order hybrid modes of a corrugated horn were found to radiate a pattern with the polarization properties of a Huygens source [132]. In contrast, the physics community most often refers to the seminal paper by Kerker *et al.* [133] in which the introduction of magnetic properties in a small sphere was shown to facilitate unidirectional forward or backward scattering. Basically, the conditions derived required balanced electric and magnetic dipole scattering responses, i.e., the excited small particle responded as a Huygens source. Again, the use of the HDC materials avoids the difficulty of fielding low loss magnetic materials from microwaves to optical frequencies.

It is important to recognize that the optical theorem tells us that forward scattering components of a directional-multipolar structure must collectively suppress the incident field and construct a new wavefront that can have a different phase to that of the background field in order to achieve zero forward-scattering or back-scattering effects [134], [135]. The scattering contributions from the various multipoles have non-negligible contributions relative to the incident field and influence the interplay between the relative absorption and scattering cross-sections [136].

The unidirectional scattering of electromagnetic waves in the backward and forward direction, termed Kerkers' first (forward dominant) and second (backwards dominant) conditions, respectively, is a prominent feature of sub-wavelength dielectric structures in which the strong electric and magnetic resonances have enabled unique opportunities for efficient manipulation of light-matter interactions. While Kerker's conditions emphasized the dipole responses, their generalization to HOMs has been a primary recent feature in all-dielectric nanophotonics investigations [137]–[141]. They have also played a major role in describing the directional scattering properties of all-dielectric MTSs, including Huygens MTSs [68], [142]–[144].

Kerker or Huygens source-based approaches have shown that the coherent excitation of combined sets of electric and magnetic multipoles (EMMs) lead to enhanced directivities. Single particle examples include [109], [145]–[155]. The efficacy of the EMM approach has also been demonstrated with the design of a multilayered nanoparticle that achieves lasing with a maximum directivity in the forward direction and a null in the backward direction, i.e., a Huygens source nanoparticle laser [156]. The overlap of a single very high order EMM was considered, for example, in [157]. Examples of arrays of EMM particles as MTSs include [68], [127], [130], [144], [158].

Several classic antenna approaches [9] to achieving higher directivity at optical frequencies have been reported. These include Yagi-Uda nanoantennas [159], [160] and nanoantenna arrays [161], [162]. The former yield electrically large systems. The latter yield higher maximum directivity values or higher front-to-back ratio (FTBR) values, but have multiple large sidelobes or broad radiation patterns. In contrast, one aspect of the physics/optics interest in multipolar fields is that a single *highly subwavelength* element could conceptually produce needle–like radiated field performance. While the remainder of this article will emphasize forward-directed unidirectional concepts and example systems, superbackscattering responses of dielectric single [135] particles and dimers [163] via their electric and magnetic dipole and quadrupolar responses, as well as of arrays with specially engineered antennas [164], [165] have been demonstrated.

IV. UNIDIRECTIONAL HUYGENS DIPOLE ANTENNAS

A simple perspective on how unidirectionality arises from a set of propagating electric and magnetic multipolar fields is that cancellation in either the forward or backward direction occurs when their magnitudes are about the same and their parities (phases) provide the appropriate constructive or destructive interference. A very important aspect of electric

and magnetic multipoles in this sense is the orthogonality of their vector patterns. Another is the fact that the parities of electric and magnetic modes interchange with increasing multipole order. To understand these concepts better, let us consider the basic HDA, i.e., a combination of a balanced pair of electric and magnetic dipole elements that produces a unidirectional field.

Consider an ideal elemental HDA located at the coordinate origin. Let the electric and magnetic dipole current densities, $\vec{J}$ and $\vec{K}$, respectively, be oriented along the $+$y and $-$x directions as shown in Fig. 1. This choice makes the $+$z-axis as the preferred broadside direction, i.e., $\hat{y} \times -\hat{x} = +\hat{z}$. Let the moments of these current densities be $I_e \ell_e$ and $I_m \ell_m$, respectively. Assume their amplitudes are a balanced pair, i.e., with $I_e \ell_e = I_0 \ell$ and $I_m \ell_m = \eta I_0 \ell$. In their far field, their electric fields are then [166]:

$$\vec{E}_{\omega,J}^{ff}(\vec{r}) = j\,\omega\mu\,I_0\ell\,\frac{e^{-jkr}}{4\pi r}\left(\hat{r} \times \hat{r} \times \hat{y}\right)$$

$$\vec{E}_{\omega,K}^{ff}(\vec{r}) = -j\,\omega\mu\,I_0\ell\,\frac{e^{ikr}}{4\pi r}\left(\hat{r} \times \hat{x}\right) \tag{5}$$

Along the $+$z-axis, $\hat{r} = +\hat{z}$ and $\hat{r} \times \hat{r} \times \hat{y} = -\hat{y}$ and $\hat{r} \times -\hat{x} = -\hat{y}$. On the other hand, along the $-$z-axis, $\hat{r} = -\hat{z}$ and $\hat{r} \times \hat{r} \times \hat{y} = -\hat{y}$ and $\hat{r} \times -\hat{x} = +\hat{y}$. Thus, the electric fields in the far field of the electric and magnetic dipoles have the same polarity along the $+$z-axis and opposite polarities along the $-$z-axis. Consequently, they add along the $+$z-axis and cancel along the $-$z-axis.

More generally, with the radial unit vector written in terms of Cartesian coordinates, one has

$$\hat{r} \times \hat{x} = \cos\theta\hat{y} - \sin\theta\sin\phi\hat{z}$$
$$\hat{r} \times \hat{r} \times \hat{x} = -\left(\sin^2\theta\sin^2\phi + \cos^2\theta\right)\hat{x}$$
$$+ \sin\theta\sin\phi\cos\phi\hat{y} + \sin\theta\cos\theta\cos\phi\hat{z}$$
$$\hat{r} \times \hat{y} = -\cos\theta\hat{x} + \sin\theta\cos\phi\hat{z}$$
$$\hat{r} \times \hat{r} \times \hat{y} = \sin^2\theta\sin\phi\cos\phi\hat{x}$$
$$- \left(\sin^2\theta\cos^2\phi + \cos^2\theta\right)\hat{y} + \sin\theta\cos\theta\sin\phi\hat{z}$$

Their combinations form the HDA. The explicit far-field expressions of the HDA's radiated fields follow straightforwardly:

$$\vec{E}_{\omega,\text{total}}^{ff}(\vec{r}) = j\,\omega\mu\,I_0\ell\,\frac{e^{-jkr}}{4\pi r}\vec{\mathcal{P}}(\theta,\phi)$$

$$\vec{H}_{\omega,\text{total}}^{ff}(\vec{r}) = \frac{1}{\eta}\hat{r} \times \vec{E}_{\omega,\text{total}}^{ff}(\vec{r}) \tag{6}$$

where the angular variation of the pattern vector field is:

$$\vec{\mathcal{P}}_{\text{HDA}}(\theta,\phi) = \left[\left(\hat{r} \times \hat{r} \times \hat{y}\right) - \left(\hat{r} \times \hat{x}\right)\right]$$
$$= \sin^2\theta\sin\phi\cos\phi\hat{x}$$
$$- \left(\cos^2\theta + \sin^2\theta\cos^2\phi + \cos\theta\right)\hat{y}$$
$$+ (\sin\theta\sin\phi + \sin\theta\cos\theta\sin\phi)\hat{z} \tag{7}$$

In the yz-plane with $\phi = \pi/2$ one then has

$$\vec{\mathcal{P}}_{\text{HDA}}(\theta,\phi = \pi/2) = -(1 + \cos\theta)\left[\cos\theta\hat{y} - \sin\theta\hat{z}\right] \tag{8}$$

Similarly, in the zx-plane with $\phi = 0$ one also has

$$\vec{\mathcal{P}}_{\text{HDA}}(\theta,\phi = 0) = -(1 + \cos\theta)\hat{y} \tag{9}$$

The noted differences along the $+$z ($\theta = 0$) and $-$z directions ($\theta = \pi$) follow immediately. Moreover, the cardioid factor: $(1 + \cos\theta)$, which is characteristic of a Huygens source field, is recognized immediately, i.e., the total of the opposite polarity fields generated by the balanced electric and magnetic dipole pair is null along the negative z-axis and is increased by a factor of 2 along the $+$z-axis.

The corresponding time-averaged Poynting's vector and the total power radiated are given by the well-known expressions

$$\vec{S}_{\text{total}}(\vec{r}) = \frac{1}{2}\text{Re}\left\{\vec{E}_{\omega,\text{total}}^{ff}(\vec{r}) \times \left[\vec{H}_{\omega,\text{total}}^{ff}(\vec{r})\right]^*\right\}$$

$$= \frac{1}{2\eta}|\vec{E}_{\omega}^{ff}(\vec{r})|^2 \tag{10}$$

$$P_{\text{total}}^{rad} = \oiint_{S_\infty^2} d\Omega\ \hat{r} \cdot \vec{S}_{\text{total}}(\vec{r}) \tag{11}$$

where * denotes the complex conjugate; S_∞^2 is the sphere (S^2) centered on the origin and whose radius is infinitely large; and the infinitesimal solid angle $d\Omega = r_\infty^2 \sin\theta\,d\theta\,d\phi$. The directivity follows as

$$D(\theta,\phi) = \frac{r_\infty^2 \vec{S}_{\text{total}}(\vec{r}) \cdot \hat{r}}{P_{\text{total}}^{rad}/4\pi} \tag{12}$$

i.e., it is the ratio of the far-field radiation intensity in a specific direction to the radiation intensity averaged over all directions [9]. It is readily verified that

$$\left|\vec{\mathcal{P}}_{\text{HDA}}(\theta,\phi)\right|^2 = (1 + \cos\theta)^2 \tag{13}$$

i.e., $|\mathcal{P}|$ is independent of ϕ. Thus, the directivity of a balanced pair of electric and magnetic dipoles simplifies to

$$D(\theta,\phi) = \frac{2\left|\vec{\mathcal{P}}_{\text{HDA}}(\theta,\phi)\right|^2}{\int_0^\pi \left|\vec{\mathcal{P}}_{\text{HDA}}(\theta,\phi)\right|^2 \sin\theta d\theta}$$

$$= \frac{3}{4}(1 + \cos\theta)^2 \tag{14}$$

Consequently, the Huygens directivity patterns are omnidirectional in the azimuthal plane. Moreover, the maximum directivity of the electric-magnetic dipole pair ($\mathcal{N} = 1$), which is along the positive z-axis, is 3, twice the value of either dipole alone confirming the Harrington result [10], [11]: $D_{max} = \mathcal{N}^2 + 2 \times \mathcal{N} = 1^2 + 2 \times 1 = 3$.

A comparison of the directivity patterns of an ideal electric dipole and an HDA is provided in Fig. 1. They were calculated with a MATLAB program using the explicit Cartesian unit vector expressions. The integrals of the total radiated power in both cases were calculated numerically. The bi-directional figure-eight pattern of the dipole element in the principle vertical plane containing the dipole (E-plane) and
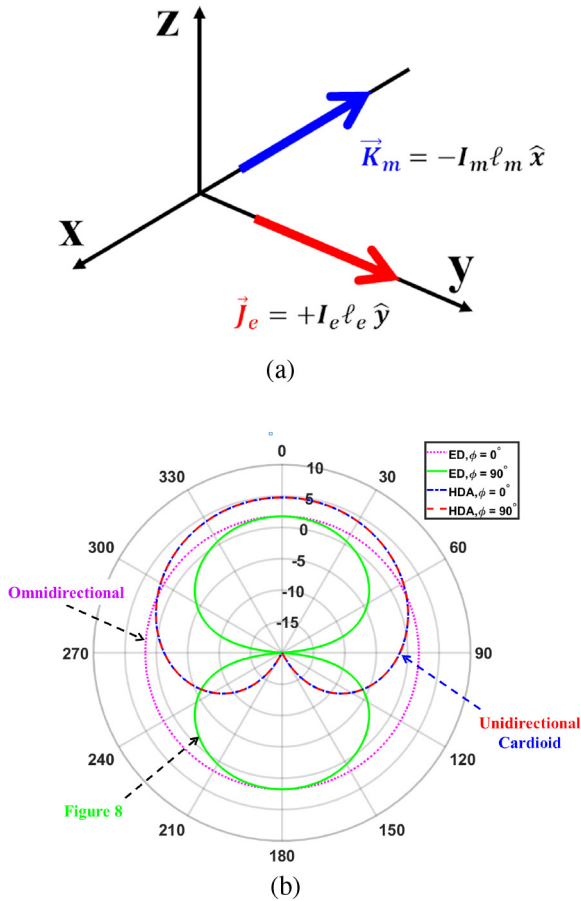
(a)

(b)

FIGURE 1. Comparison of the directivity patterns of an electric dipole and of an ideal HDA. (a) Source configuration with the electric dipole along the y-axis (red) and the magnetic dipole along the −x-axis (blue). (b) Directivity patterns. $\theta = 0°$ is the broadside direction along the +z-axis.

the omnidirectional pattern in the principal vertical plane orthogonal to it are clearly identified. The unidirectional cardioid patterns radiated by the HDA are identical in both principle planes as was demonstrated analytically. The peak directivity of the electric dipole and the HDA are 1.76 and 4.77 dB, respectively, i.e., the unidirectional patterns have a factor of 3 dB (2 times) larger peak directivity than the bidirectional ones. These basic concepts extend naturally to the HOMs.

V. UNIDIRECTIONAL MULTIPOLE RADIATING SYSTEMS

The concept of superdirectivity has permeated the physics and applied physics literature repeatedly since Oseen discussed the concept of "needle radiation" almost a century ago [167], [168]. As demonstrated in both 2D [169] and 3D [168], true needle radiation in a LTI (linear, time-invariant, isotropic) region of space can be obtained if one superimposes the multipoles associated with the orthogonal complete basis function expansion of the Helmholtz operator with the proper weights. In fact, the completeness relation of the multipolar basis functions tells us that this is possible. If the set of those basis functions is finite, it will be said that a "needle-like" beam is attained.
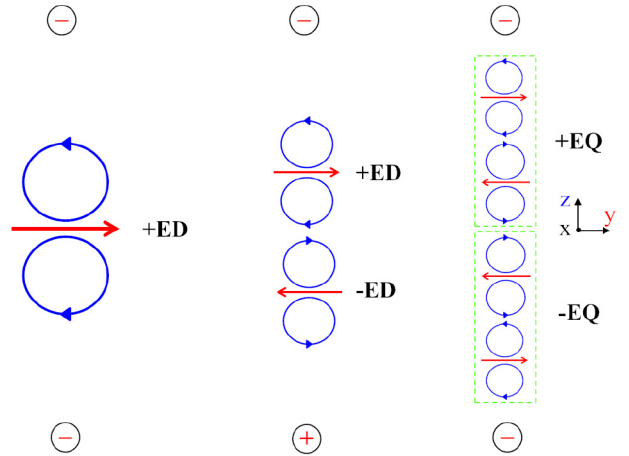

FIGURE 2. Comparison of the ED, EQ and EQ fields constructed with electric current moments with the same orientation parallel to the horizontal direction. Each current generation multipole is obtained as a pair of the previous generation with opposite orientation. The polarity of the net field for each multipole generation is indicated with respect to the vertical direction.

### A. 3D MULTIPOLE CONSTRUCTION

To better appreciate the interest in HOMs for enhanced directivity systems, several examples are considered. The first is to remind ourselves how a multipole can be formed with dipole elements. In fact, the basic concept is well-understood from how a dipole itself is formed from a pair of positive and negative charges. Each charge radiates a monopole field. However, when they are placed in very close proximity, their opposite polarity leads to a cancellation of their monopole fields, leaving the well-known dipole field as the net result. In a similar fashion, a multipole of order N can be formed by a pair of (N − 1)-multipoles with opposite polarity. Because the distance between these two elements is taken to be very small, the result is effectively a directional derivative with respect to the separation direction [13], [34], [35], [170].

To further understand this construction, consider the left column in Fig. 2. An electric dipole is represented by an electric current element pointed along the positive y-axis. The electric field that it radiates along the z-axis has the same polarity in the upper and lower hemispheres along the y-direction as discussed in the HDA analysis. Now take a magnetic current (magnetic dipole) along the -x-axis as illustrated in Fig. 1. Similarly, as discussed above, the electric field it radiates along the z-axis has the opposite polarity in the upper and lower hemispheres as depicted in Fig. 2. The combination – the Huygens dipole – radiates the cardioid directivity pattern presented alone in Fig. 3. Its peak directivity is 4.77 dB along the z-axis and its FTBR $= D_{\text{dipole}}(\theta = 0°)/D_{\text{dipole}}(\theta = 180°)$, is infinite.

Now consider two electric dipole elements that point in opposite directions along the y-axis and that are centered along the z-axis with a separation distance $\Delta z/2$ with respect to the origin, where Δz is very small in comparison to the wavelength. This arrangement is illustrated in the center column of Fig. 2. The angular distribution of the electric
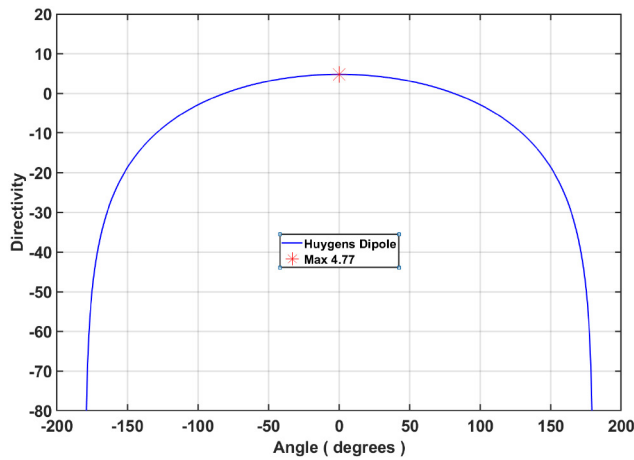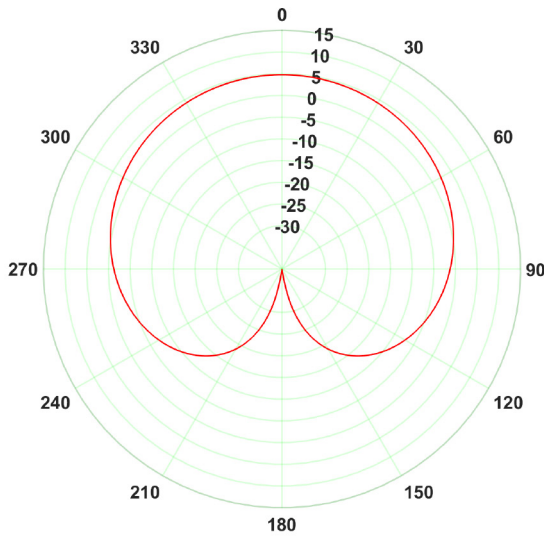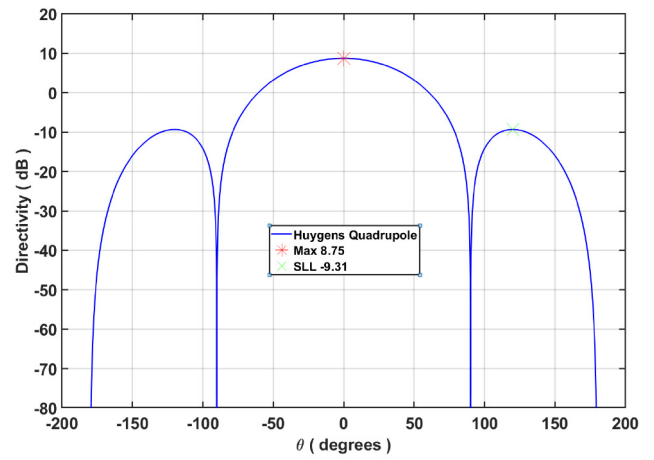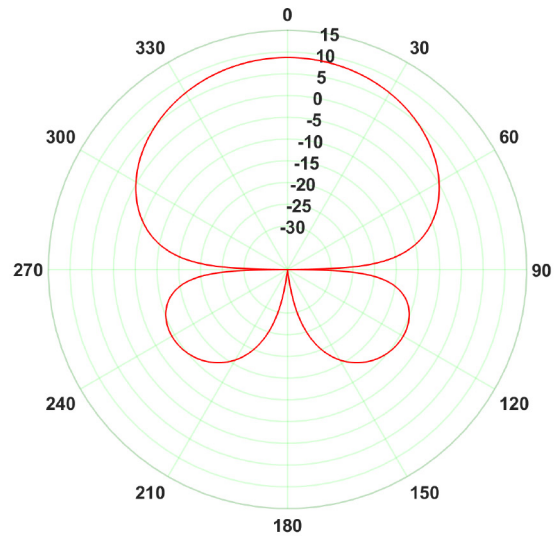
FIGURE 3. Huygens dipole patterns. (a) Linear plot. (b) Polar plot.

FIGURE 4. Huygens quadrupole patterns. (a) Linear plot. (b) Polar plot.

field generated by this two element array in its far-field is proportional to:

$$\left[e^{+jk_0 \cos\theta \Delta z/2} - e^{-jk_0 \cos\theta \Delta z/2} \right] \times \{\text{Dip. Elem. Patt.}\}$$
$$= 2j \sin\left[\left(\frac{k_0 \Delta z}{2} \right) \cos\theta \right] \times \{\text{Dip. Elem. Patt.}\}$$
$$\approx (jk_0 \Delta z) \cos\theta \times \{\text{Dipole Element Pattern}\} \quad (15)$$

The result is basically the z-derivative of the two-dipole pattern. One immediately sees that the electric field that the pair radiates along the z-axis has the opposite polarity with respect to the y-axis in the upper and lower hemispheres; i.e., for $\theta = 0$ and $\theta = \pi$. With two magnetic current elements properly paired with the electric ones, the electric field radiated by these oppositely oriented magnetic dipoles has the same polarity along the y-axis in the upper and lower hemispheres. The combination of the two electric and two magnetic dipoles yields the Huygens quadrupole directivity

pattern presented in Fig. 4. As indicated, its peak directivity is 8.75 dB along the z-axis and the sidelobe level (SLL) is 18.06 dB below that peak value. The FTBR remains infinite. Note that it is null along the entire xy-plane where $\theta = \pi/2$.

Now consider two electric quadrupole elements along the z-axis that are separated by the distance $\Delta z/2$ with respect to the origin and are pointing in opposite directions along the y-axis, where Δz is very small in comparison to the wavelength. This arrangement is illustrated in the right column of Fig. 2. The angular distribution of the electric field generated by this two element array in its far-field is proportional to:

$$\left[e^{+jk_0 \cos\theta \Delta z/2} - e^{-jk_0 \cos\theta \Delta z/2} \right] \times \{\text{Quad. Elem. Patt.}\}$$
$$= 2j \sin\left[\left(\frac{k_0 \Delta z}{2} \right) \cos\theta \right] \times \{\text{Quad. Elem. Patt.}\}$$
$$\approx (jk_0 \Delta z) \cos\theta \times \{\text{Quadrupole Element Pattern}\}$$
$$= (jk_0 \Delta z)^2 \cos^2\theta \times \{\text{Dipole Element Pattern}\} \quad (16)$$
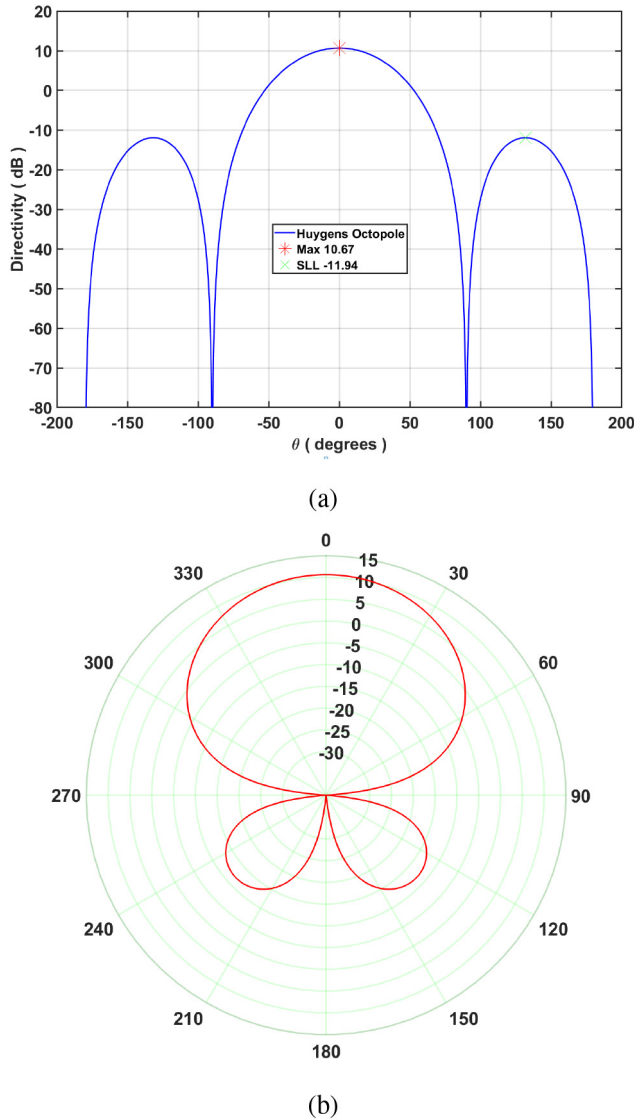
(a)

(b)

FIGURE 5. Huygens octopole patterns. (a) Linear plot. (b) Polar plot.

The result is basically two z-derivatives of the two-quadrupole pattern. One immediately sees that now the electric field the pair radiates along the z-axis has the same polarity along the y-direction in the upper and lower hemispheres. The corresponding pair of magnetic dipoles radiates electric fields along the z-axis with the opposite polarity along the y-axis in the upper and lower hemispheres. The combination of the four electric and four magnetic dipoles yields the Huygens octopole directivity pattern presented in Fig. 5. As indicated, its peak directivity is 10.67 dB along the z-axis and the sidelobe level (SLL) is 22.61 dB below that peak value. The FTBR is infinite. Note that it is again null along the entire xy-plane where $\theta = \pi/2$.

As shown in [168], the far-field electric and magnetic fields of a Huygens (M+1)-multipole formed with this

difference procedure would have the form

$$\vec{E}_\omega^{ff}(\vec{r}) = i\,\omega\mu I\ell\,\frac{e^{ikr}}{4\pi r}(1+\cos\theta)\mathcal{P}_M(\theta)$$
$$\times \left[\cos\phi\hat{\theta} - \sin\phi\hat{\phi}\right]$$
$$\vec{H}_\omega^{ff}(\vec{r}) = i\,\omega\mu\,\frac{I\ell}{\eta}\,\frac{e^{ikr}}{4\pi r}(1+\cos\theta)\mathcal{P}_M(\theta)$$
$$\times \left[\sin\phi\hat{\theta} + \cos\phi\hat{\phi}\right] \quad (17)$$

where $\mathcal{P}_M \propto \cos^M\theta$ for $M = 0, 1, \dots$ Thus, the directivity takes the form

$$D(\theta, \phi) = \frac{2\mathcal{P}_M^2(\theta)\left|\vec{\mathcal{P}}_{\text{HDA}}(\theta, \phi)\right|^2}{\int_0^\pi \mathcal{P}_M^2(\theta)\left|\vec{\mathcal{P}}_{\text{HDA}}(\theta, \phi)\right|^2 \sin\theta d\theta} \quad (18)$$

Note that the factor of 2 in the numerator arises, as it did in the ideal HDA version, from the azimuthal symmetry of the radiated fields which yields 2π from the ϕ integration in the denominator and its subsequent division by 4π. Also note that if it was only an electric multipole or a magnetic multipole, the $\cos\phi$ and $\sin\phi$ terms in their element vector patterns would introduce a factor of $1/2$ into the total power radiated. The presence of both yields the sum $(1/2 + 1/2) = 1$.

As the di-quad-octo–pole examples illustrate, there is an immediate increase in the directivity when a HOM is employed; and, yet, it is also clear that the added benefit begins to decrease as M increases. To understand this point more clearly, the angle dependence of the ℓ-th term of the spherical harmonic expansion that yields the maximum along the z-axis is proportional to the associated Legendre polynomial of degree ℓ and order 1: $P_\ell^1(\cos\theta)$ and yields the terms $P_\ell(\cos\theta)\cos\phi$ and $P_\ell(\cos\theta)\sin\phi$, where P_ℓ is the Legendre polynomial of degree ℓ. Thus, the directivity of such a Huygens multipole would be proportional to $|P_\ell(\cos\theta)|^2$. Referring to the discussion of a single ℓ-th multipole in [146], its directivity increases as $(2\ell + 1)/2$. The corresponding directivity of a Huygens multipole then increases only as $2\ell + 1$. Thus, the increase from one multipole to the next is only 2. For example, if $\ell = 10$, the directivity of the next HOM with degree 11 only increases from 21 to 23.

However, if one could arrange a source that radiates all of the first N multipoles with the appropriate amplitude weights to achieve a needle-like beam, then accounting for the normalization of the associated Legendre polynomials, its pattern takes the form [168]:

$$\mathcal{P}_{N,\text{needle}}(\theta) \propto \sum_{\ell=1}^{N}\left[\frac{2\ell+1}{4\pi}\right]P_\ell(\cos\theta) \quad (19)$$

The directivity is then:

$$D_{\text{Needle}}(\theta, \phi) = \frac{2\mathcal{P}_{N,\text{needle}}^2(\theta)}{\int_0^\pi \mathcal{P}_{N,\text{Needle}}^2(\theta)\sin\theta d\theta} \quad (20)$$
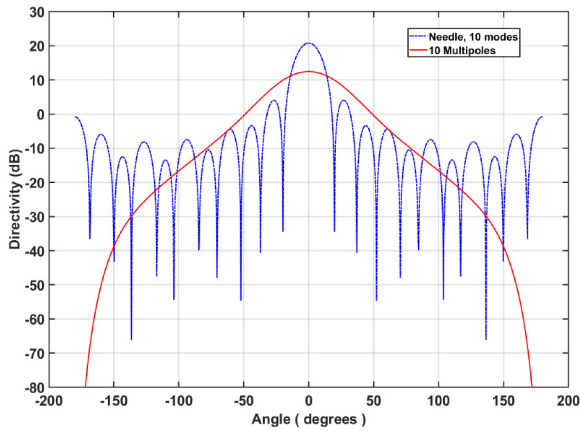
FIGURE 6. Comparison of the directivity of the 10-element needle and difference-constructed multipole systems.

In addition, if balanced electric- and magnetic-source fields are radiated, the directivity of the resulting Huygens system becomes

$$D_{\text{Needle total}}^{N} = 2D_{\text{Needle}} = 2\left[\sum_{\ell=1}^{N}(2\ell+1)/2\right] = N^2 + 2N \quad (21)$$

i.e., Harrington's limit is attained. Thus, the directivity benefit from a source properly radiating N multipoles to one radiating $N+1$ multipoles is $2N+3$, which is large if N is. For instance, if $N = 10$, then the directivity of the $N = 11$ multipole modes increases from 120 to 143, an increase of 23 (13.62 dB). In comparison, the corresponding pattern of a Huygens source consisting of all of the first N Huygens multipoles formed by the difference construction with appropriate amplitude weights becomes

$$\mathcal{P}_{N,\text{difference}}(\theta) = \sum_{n=1}^{N}(\cos\theta)^{(n-1)} = \left\{\frac{1-\cos^N\theta}{1-\cos\theta}\right\} \quad (22)$$

Thus, its directivity is:

$$D_{\text{Difference,total}}(\theta, \phi)$$
$$= \frac{2\mathcal{P}_{N,\text{difference}}^2(\theta)\left|\vec{\mathcal{P}}_{\text{HDA}}(\theta, \phi)\right|^2}{\int_0^{\pi}\mathcal{P}_{N,\text{difference}}^2(\theta)\left|\vec{\mathcal{P}}_{\text{HDA}}(\theta, \phi)\right|^2\sin\theta\, d\theta} \quad (23)$$

The directivity patterns for $N = 10$ multipoles of the needle and difference cases is presented in Fig. 6. The peak directivity in the needle-like case was calculated to be 20.8 dB (120.0), in total agreement with the Harrington bound: $10^2 + 2 \times 10 = 120$. This outcome follows naturally from (19) and (21) since $P_\ell(\theta = 0) = 1$. The peak in the difference case is 12.44 dB (17.56). While it clearly has a smaller peak directivity than the needle-like case, the very appealing aspect of the difference-constructed multipole case is the complete absence of any sidelobes. The number of sidelobes in the needle case increases as the

degree ℓ increases. Thinking about how directivity is calculated, the absence of the many sidelobe nulls found in the needle case is responsible for the smaller peak value, i.e., the denominator is much larger in the difference case. The actual bound in the needle case occurs because power is lost to those many sidelobes. While the peak of the needle beam's directivity increases quadratically and its width decreases [168] as N increases, its backlobe does not decrease at a similar rate because $P_\ell(\theta = \pi) = (-1)^\ell$. For the even mode case presented, the backlobe is -0.78 dB (0.835) and, hence, the FTBR is only 21.58 dB (144), which is not significantly different from the peak directivity. From an applications point-of-view, the lack of sidelobes in the difference-constructed set of Huygens HOMs case and having the FTBR $= \infty$ are quite appealing properties for a number of EM applications.

B. CYLINDRICAL MULTIPOLE PHENOMENA

The well-known complex analytical representations of 3D field structures lead to a less transparent understanding of the basic EM associated with multipoles. The math associated with cylindrical versions is notationally simpler and, hence, concepts are often more readily ascertained. Consequently, the explicit representations of a 2D cylindrical configuration are reviewed in order to describe in detail the relevant features of several unidirectional designs.

As demonstrated in [169], one can achieve a 2D needle field. In fact, a highly subwavelength superdirective system was attained with a metamaterial-inspired multilayered cylindrical structure and facilitated by a multipolar design approach. A number of works have since duplicated the concept [171] and have suggested ways to improve upon the original approach [172]–[174] and others have extended the concept to spherical versions [175], [176]. In all of these cases, the driven source has been taken to be in the exterior of the multilayered structure. Since one can argue that the meta-structure excited by an exterior source acts like a lens or wavefront transformation element, the cylindrical case in which the source is in the core of the multilayered meta-structure is discussed as an actual antenna configuration here. All of the cases to be presented were developed in terms of an arbitrary wavelength, were double checked with specific wavelengths both large and small, and, hence, are suitable (in principle) for any wavelength, from RF to optical. Superdirective results are presented to demonstrate the potential of multipolar designs for highly directive applications.

1) GENERAL PROBLEM CONFIGURATION

The general two-dimensional (2D) canonical problem of interest is an $N + 1$ region configuration. It consists of a circularly cylindrical core of radius r_1 (Region 1) covered with $N-1$ concentric layers, and Regions ℓ with outer radius r_ℓ, $\ell = 2, \ldots, N$. This N region structure is embedded in an infinite ambient host LTI medium (Region $N + 1$). A cylindrical coordinate system, (ρ, ϕ, z), is introduced. The axes of the cylinders coincide with its z-axis.
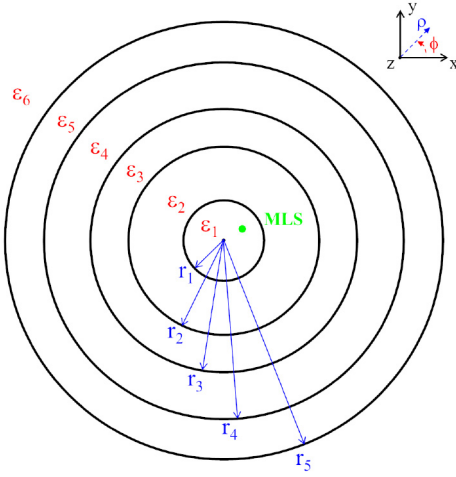
FIGURE 7. Concentric six region, 5 dielectric layer, superdirective cylindrical antenna configuration.

Region ℓ with $\ell = 1, 2, \ldots, N$, is characterized by the permittivity ε_ℓ and permeability μ_ℓ. Assuming the $\exp(j\omega t)$ time dependence throughout, the wavenumber and impedance in each layer are, respectively, $k_\ell = \omega\sqrt{\varepsilon_\ell\,\mu_\ell}$ and $\eta_\ell = \sqrt{\mu_\ell/\varepsilon_\ell}$. The excitation is taken to be a magnetic line source (MLS) located in Region 1 and parallel to the z-axis. Consequently, the problem is 2D and only TE^z polarized fields are considered. The three relevant electromagnetic field components are thus (H_z, E_ρ, E_ϕ). In fact, only the H_z component of the field and derivatives of it are needed to characterize the TE^z source and scattered fields. The main steps of the analytical solution of this canonical problem are described below and follow the well-known separation of variables boundary value problem solution approach, e.g., in [177].

2) SPECIFIC PROBLEM CONFIGURATION

A cross section of the specific 2D configuration is depicted in Fig. 7. It is a 5-layer, 6 region case. Each layer is assumed to be a dielectric medium and, thus, $\mu_\ell = \mu_0$ for $\ell = 1, \ldots, 5$. The permittivity of each layer is labeled as ε_ℓ. The exterior region is taken to be free space. Thus, $\varepsilon_6 = \varepsilon_0$ and $\mu_6 = \mu_0$. The MLS is defined by the constant magnetic current $I_{\mathrm{MLS}} = 1.0\,[V]$. It is characterized by the frequency f_0 and the corresponding free-space wavelength $\lambda_0 = c/f_0$, where c is the speed of light in vacuum: $c = 1/\sqrt{\epsilon_0\mu_0}$. Consequently, the free-space wave number and impedance are $k_0 = \omega\sqrt{\varepsilon_0\mu_0} = 2\pi/\lambda_0$ and $\eta_0 = \sqrt{\mu_0/\varepsilon_0}$, respectfully.

3) ANALYSIS

The details associated with the analytical solution and numerical results of the superdirective cylinder problem are presented. It is first shown that the offset magnetic line source radiates the multipolar fields necessary to excite those of the metastructure. The corresponding scattered fields in cylindrical harmonics are given. The solution process is briefly described. Several cases are discussed. The superdirective ones are emphasized.

4) SOURCE

The magnetic field generated by an MLS in an unbounded LTI medium characterized by permittivity ϵ_{MLS}, permeability μ_{MLS}, and wavenumber k_{MLS} is given by the Green's function-based expression [9], [30]

$$\boldsymbol{H}_{\mathrm{MLS}}(\boldsymbol{\rho}) = -\hat{z}I_{\mathrm{MLS}}(\omega)\frac{\omega\epsilon_{\mathrm{MLS}}}{4}H_0^{(2)}(k_{\mathrm{MLS}}|\boldsymbol{\rho} - \boldsymbol{\rho_s}|) \quad (24)$$

where $H_0^{(2)}(\cdot)$ denotes the Hankel function of second kind and order zero, and $|\boldsymbol{\rho}-\boldsymbol{\rho_s}| = \sqrt{\rho^2 + \rho_s^2 - 2\rho\rho_s\cos(\phi - \phi_s)}$ is the radial distance from the MLS location (ρ_s, ϕ_s) to an arbitrary observation point (ρ, ϕ). The multipolar nature of the MLS field when it is located away from the origin of the coordinate systems is obtained by applying the addition theorem for Hankel functions [29, Appendix D, p. 591]. One finds

$$H_0^{(2)}(k\,|\boldsymbol{\rho} - \boldsymbol{\rho_s}|) = \begin{cases} \sum_{n=-\infty}^{\infty} J_n(k\,\rho)H_n^{(2)}(k\,\rho_s)e^{jn(\phi-\phi_s)} \\ \qquad \text{for } \rho \leq \rho_s \\ \sum_{n=-\infty}^{\infty} J_n(k\,\rho_s)H_n^{(2)}(k\,\rho)e^{jn(\phi-\phi_s)} \\ \qquad \text{for } \rho \geq \rho_s \end{cases}$$

$$(25)$$

where $J_n(\cdot)$ denotes the Bessel function of the first kind and order n. Through application of (25) to (24), the magnetic field radiated by the MLS in terms of cylindrical wave functions originating at the origin becomes

$$\boldsymbol{H}_{\mathrm{MLS}}(\rho, \phi) = -\hat{z}I_{\mathrm{MLS}}(\omega)\frac{\omega\epsilon_{\mathrm{MLS}}}{4}$$
$$\times \begin{cases} \sum_{n=-\infty}^{\infty} J_n(k_{\mathrm{MLS}}\rho)H_n^{(2)}(k_{\mathrm{MLS}}\rho_s)e^{jn(\phi-\phi_s)} \text{ for } \rho \leq \rho_s \\ \sum_{n=-\infty}^{\infty} J_n(k_{\mathrm{MLS}}\rho_s)H_n^{(2)}(k_{\mathrm{MLS}}\rho)e^{jn(\phi-\phi_s)} \text{ for } \rho \geq \rho_s \end{cases}$$

$$(26)$$

It is advantageous for numerical implementation of these expressions to fold the summation over n, which ranges from $-\infty$ to ∞, to the range from 0 to ∞. The complex exponential can be written as

$$\sum_{n=-\infty}^{\infty} e^{jn(\phi-\phi_n)} = \sum_{n=0}^{\infty} \tau_n \cos[n(\phi - \phi_s)], \quad (27)$$

where we have introduced the Neumann number:

$$\tau_n = \begin{cases} 1 & \text{for } n = 0 \\ 2 & \text{otherwise} \end{cases} \quad (28)$$

Consequently, with the connection relations: $J_{-n}(z) = (-1)^n J_n(x)$ and $H_{-n}^{(2)}(z) = (-1)^n H_n^{(2)}(x)$, (26) can be rewritten as

$$\boldsymbol{H}_{\mathrm{MLS}}(\rho, \phi) = -\hat{z}I_{\mathrm{MLS}}(\omega)\frac{\omega\epsilon_{\mathrm{MLS}}}{4}$$
$$\times \begin{cases} \sum_{n=0}^{\infty} \tau_n J_n(k_{\mathrm{MLS}}\rho)H_n^{(2)}(k_{\mathrm{MLS}}\rho_s)\cos[n(\phi-\phi_s)] \\ \qquad \text{for } \rho \leq \rho_s \\ \sum_{n=0}^{\infty} \tau_n J_n(k_{\mathrm{MLS}}\rho_s)H_n^{(2)}(k_{\mathrm{MLS}}\rho)\cos[n(\phi-\phi_s)] \\ \qquad \text{for } \rho \geq \rho_s \end{cases}$$

$$(29)$$

The electric field corresponding to the magnetic field (29) follows from the application of the Maxwell-Amperes law

$$\nabla \times \boldsymbol{H} = j\omega\epsilon\boldsymbol{E} \longrightarrow \boldsymbol{E} = \frac{1}{j\omega\epsilon}\left[\hat{\rho}\frac{1}{\rho}\frac{\partial H_z}{\partial\phi} - \hat{\phi}\frac{\partial H_z}{\partial\rho}\right] \quad (30)$$

One thus obtains

$$\boldsymbol{E}_{\mathrm{MLS}}(\rho,\phi) = \frac{I_{\mathrm{MLS}}(\omega)}{4j}$$

$$\times \begin{cases} \hat{\rho}\frac{1}{\rho}\sum_{n=0}^{\infty}\tau_n n J_n(k_{\mathrm{MLS}}\rho)H_n^{(2)}(k_{\mathrm{MLS}}\rho_{\mathrm{s}})\,\sin[n(\phi-\phi_{\mathrm{s}})] \\ +\hat{\phi}k_{\mathrm{MLS}}\sum_{n=0}^{\infty}\tau_n J_n'(k_{\mathrm{MLS}}\rho)H_n^{(2)}(k_{\mathrm{MLS}}\rho_{\mathrm{s}}) \\ \qquad\times\cos[n(\phi-\phi_{\mathrm{s}})] \text{ for } \rho\le\rho_{\mathrm{s}} \\ \hat{\rho}\frac{1}{\rho}\sum_{n=0}^{\infty}\tau_n n J_n(k_{\mathrm{MLS}}\rho_{\mathrm{s}})H_n^{(2)}(k_{\mathrm{MLS}}\rho)\,\sin[n(\phi-\phi_{\mathrm{s}})] \\ +\hat{\phi}k_{\mathrm{MLS}}\sum_{n=0}^{\infty}\tau_n J_n(k_{\mathrm{MLS}}\rho_{\mathrm{s}})H_n^{(2)'}(k_{\mathrm{MLS}}\rho) \\ \qquad\times\cos[n(\phi-\phi_{\mathrm{s}})] \text{ for } \rho\ge\rho_{\mathrm{s}} \end{cases}$$
$$(31)$$

where the derivative symbol

$$' = \frac{\partial}{\partial(k_{\mathrm{MLS}}\rho)}$$

As indicated, the prime indicates partial differentiation of the cylindrical wave functions with respect to its entire argument. This operation is applied using the chain rule [178]:

$$\frac{\mathrm{d}}{\mathrm{d}x}Z_p(\alpha x) = \frac{\mathrm{d}}{\mathrm{d}x}(\alpha x)\frac{\mathrm{d}}{\mathrm{d}(\alpha x)}Z_p(\alpha x) = \alpha Z'(\alpha x) \quad (32)$$

where Z_p can be the Bessel function, J_p, Neumann function, Y_p, or Hankel function of first or second kind of order p, $H_p^{(1,2)}$, and α is an arbitrary constant. Consequently, the derivative of a cylindrical wave function with respect to its entire argument is easily performed by combining [9, (IV-18), (IV-19)] and leads to the general relation

$$\frac{\mathrm{d}}{\mathrm{d}(\alpha x)}Z_p(\alpha x) = \frac{1}{2}\left[Z_{p-1}(\alpha x) - Z_{p+1}(\alpha x)\right] \quad (33)$$

which leads to a simple implementation of the field expressions in MATLAB.

5) FIELDS

The scattered fields in Regions 1–5, the radiated fields in Region 6, and the fields radiated by the MLS: (29), (30), in Region 1 constitute the expressions of the total fields in these regions. The scattered field can also be expanded in terms of the cylindrical multipolar expansion [9], [30]. It is advantageous to note first the following. The scattered magnetic and electric fields in Regions 2-5 are composed of traveling waves propagating in the positive and negative radial directions and are described by a summations of Bessel functions of first kind and order n, $J_n(k\rho)$, and Neumann functions of order n, $Y_n(k\rho)$. Those in Region 1 are described by a summation of only the Bessel functions because the Neumann functions are singular at the origin. In Region 6, the magnetic and electric fields are represented simply by outward propagating waves. These waves are properly described by Hankel Functions of the second kind and

order n, i.e., $H_n^{(2)}(k\rho)$, for the assumed $\exp(j\omega t)$ time convention. Therefore, it follows that the scattered magnetic fields in Regions 1–6 with $\ell = 2,\ldots,5$ can be expressed as

$$\boldsymbol{H}^{1\mathrm{s}}(\rho,\phi) = -\hat{z}I_{\mathrm{MLS}}(\omega)\frac{\omega\epsilon_1}{4}$$
$$\times\sum_{n=0}^{\infty}\tau_n A_n^1 J_n(k_1\rho)\cos[n(\phi-\phi_{\mathrm{s}})]$$

$$\boldsymbol{H}^{\ell\mathrm{s}}(\rho,\phi) = -\hat{z}I_{\mathrm{MLS}}(\omega)\frac{\omega\epsilon_\ell}{4}$$
$$\times\sum_{n=0}^{\infty}\tau_n\left[A_n^\ell J_n(k_\ell\rho) + B_n^\ell Y_n(k_\ell\rho)\right]$$
$$\times\cos[n(\phi-\phi_{\mathrm{s}})]$$

$$\boldsymbol{H}^{6\mathrm{s}}(\rho,\phi) = -\hat{z}I_{\mathrm{MLS}}(\omega)\frac{\omega\epsilon_6}{4}$$
$$\times\sum_{n=0}^{\infty}\tau_n A_n^6 H_n^{(2)}(k_6\rho)\cos[n(\phi-\phi_{\mathrm{s}})] \quad (34)$$

where A_n^p, $p = 1,\ldots,6$, and B_n^q, $q = 2,\ldots,5$, represent the ten unknown expansion coefficients. The associated scattered electric fields in Regions 1–6 with $\ell = 2,\ldots,5$ are

$$\boldsymbol{E}^{1\mathrm{s}} = \frac{I_{\mathrm{MLS}}(\omega)}{4j}\left\{\hat{\rho}\frac{1}{\rho}\sum_{n=0}^{\infty}\tau_n n A_n^1 J_n(k_1\rho)\sin[n(\phi-\phi_{\mathrm{s}})]\right.$$
$$\left. + \hat{\phi}k_1\sum_{n=0}^{\infty}\tau_n A_n^1 J_n'(k_1\rho)\cos[n(\phi-\phi_{\mathrm{s}})]\right\}$$

$$\boldsymbol{E}^{\ell\mathrm{s}} = \frac{I_{\mathrm{MLS}}(\omega)}{4j}$$
$$\times\left\{\hat{\rho}\frac{1}{\rho}\sum_{n=0}^{\infty}\tau_n n\left[A_n^\ell J_n(k_\ell\rho) + B_n^\ell Y_n(k_\ell\rho)\right]\sin[n(\phi-\phi_{\mathrm{s}})]\right.$$
$$\left. + \hat{\phi}k_\ell\sum_{n=0}^{\infty}\tau_n\left[A_n^\ell J_n'(k_\ell\rho) + B_n^\ell Y_n'(k_\ell\rho)\right]\cos[n(\phi-\phi_{\mathrm{s}})]\right\}$$

$$\boldsymbol{E}^{6\mathrm{s}} = \frac{I_m(\omega)}{4j}\left\{\hat{\rho}\frac{1}{\rho}\sum_{n=0}^{\infty}\tau_n n A_n^6 H_n^{(2)}(k_6\rho)\sin[n(\phi-\phi_{\mathrm{s}})]\right.$$
$$\left. + \hat{\phi}k_6\sum_{n=0}^{\infty}\tau_n A_n^6 H_n^{(2)'}(k_6\rho)\cos[n(\phi-\phi_{\mathrm{s}})]\right\} \quad (35)$$

These expressions for the magnetic and electric fields are valid for an arbitrary position of the MLS in Region 1. Because the MLS is located in the core, Region 1, the total magnetic field in Regions 1–6 with $\ell = 2,\ldots,5$ is

$$\boldsymbol{H}_{\mathrm{tot}}^{(1)} = \boldsymbol{H}^{1\mathrm{s}} + \boldsymbol{H}_{\mathrm{MLS}}$$
$$\boldsymbol{H}_{\mathrm{tot}}^{(\ell)} = \boldsymbol{H}^{\ell\mathrm{s}}$$
$$\boldsymbol{H}_{\mathrm{tot}}^{(6)} = \boldsymbol{H}^{6\mathrm{s}} \quad (36)$$

The same holds true for the total electric field $\boldsymbol{E}_{\mathrm{tot}}^i$, $i = 1,2,3,4,6$. These total magnetic and electric field expressions are used to determine the unknown expansion coefficients by applying the electromagnetic boundary conditions across each interface. To simplify the discussion, the total and scattered field designators will appear only when necessary below.

6) SOLUTION

In order to determine the expansion coefficients, the electromagnetic boundary conditions for the magnetic and electric fields at the cylindrical interfaces between Regions 1 to 6 are enforced. They require the continuity of the tangential components of the total magnetic and electric fields at each interface [9]. The component of the total magnetic field which is tangential at those cylindrical interfaces is the z-component, while that of the electric field is the ϕ-component.

At the inner surface, $\rho = r_1$, the continuity boundary conditions applied to the total fields require

$$H_z^1(\rho = r_1, \phi) = H_z^2(\rho = r_1, \phi)$$
$$E_\phi^1(\rho = r_1, \phi) = E_\phi^2(\rho = r_1, \phi) \tag{37}$$

which result in the first system of equations

$$\epsilon_1 J_n(k_1 r_1) A_n^1 - \epsilon_2 J_n(k_2 r_1) A_n^2 - \epsilon_2 Y_n(k_2 r_1) B_n^2$$
$$= -\epsilon_1 J_n(k_1 \rho_s) H_n^{(2)}(k_1 r_1)$$
$$k_1 J_n'(k_1 r_1) A_n^1 - k_2 J_n'(k_2 r_1) A_n^2 - k_2 Y_n'(k_2 r_1) B_n^2$$
$$= -k_1 J_n(k_1 \rho_s) H_n^{(2)\prime}(k_1 r_1) \tag{38}$$

At the surface $\rho = r_\ell$, with $\ell = 2, \ldots, 4$ the continuity boundary conditions require

$$H_z^\ell(\rho = r_\ell, \phi) = H_z^{\ell+1}(\rho = r_\ell, \phi)$$
$$E_\phi^\ell(\rho = r_\ell, \phi) = E_\phi^{\ell+1}(\rho = r_\ell, \phi) \tag{39}$$

which result in the second, third and fourth system of equations

$$\epsilon_\ell J_n(k_\ell r_\ell) A_n^\ell + \epsilon_\ell Y_n(k_\ell r_\ell) B_n^\ell$$
$$- \epsilon_{\ell+1} J_n(k_{\ell+1} r_\ell) A_n^{\ell+1} - \epsilon_{\ell+1} Y_n(k_{\ell+1} r_\ell) B_n^{\ell+1} = 0$$
$$k_\ell J_n'(k_\ell r_\ell) A_n^\ell + k_\ell Y_n'(k_\ell r_\ell) B_n^\ell$$
$$- k_{\ell+1} J_n'(k_{\ell+1} r_\ell) A_n^{\ell+1} - k_{\ell+1} Y_n'(k_{\ell+1} r_\ell) B_n^{\ell+1} = 0 \tag{40}$$

Lastly, at the outermost surface $\rho = r_5$, the continuity boundary conditions require

$$H_z^5(\rho = r_5, \phi) = H_z^6(\rho = r_5, \phi)$$
$$E_\phi^5(\rho = r_5, \phi) = E_\phi^6(\rho = r_5, \phi) \tag{41}$$

which result in the fifth and last system of equations

$$\epsilon_5 J_n(k_5 r_5) A_n^5 + \epsilon_5 Y_n(k_5 r_5) B_n^5 - \epsilon_6 H_n^{(2)}(k_6 r_5) A_n^6 = 0$$
$$k_5 J_n'(k_5 r_5) A_n^5 + k_5 Y_n'(k_5 r_5) B_n^5 - k_6 H_n^{(2)\prime}(k_6 r_5) A_n^6 = 0 \tag{42}$$

The sets of equations (38), (40) and (42) yield a system of ten linear equations with respect to the ten expansion coefficients that can be written as

$$M_n C_n = \Lambda_n, \quad n = 1, 2, 3, 4, 5 \ldots \tag{43}$$

The matrix M contains the information about the materials and geometry that defines the amplitudes of each of the cylindrical modes in each region. The excitation vector Λ_n is defined by the MLS expansion coefficients. The vector C_n contains the unknown scattered field expansion coefficients.

The matrix equation (43) can be inverted for the unknown coefficients as

$$C_n = [M_n]^{-1} \Lambda_n \tag{44}$$

The results to be presented below were obtained by implementing this required matrix inverse in MATLAB using the "left-division operator \" as $C_n = M_n \backslash \Lambda_n$. It is an efficient, well-behaved numerical method that is recommended by MathWorks. In the actual numerical implementation, the mode summations in the field expressions had to be truncated to the finite truncation limit N, i.e., the number of modes, which led to a solvable $N \times N$ matrix equation.

7) DIRECTIVITY

In order to calculate the directivity, the total radiated power per unit angle in the far-field of the source must be determined. The far-field expressions of the fields are obtained by using the large argument approximation of the Hankel function [178, Ch. 9]:

$$H_n^{(2)}(x) \approx \sqrt{\frac{2}{\pi x}} e^{-j(x - n\frac{\pi}{2} - \frac{\pi}{4})}, \quad |x| \to \infty \tag{45}$$

In particular, the far-field approximation of the total magnetic field in Region 6 is

$$H_{total}^{ff}(\rho, \phi) = \lim_{\rho \to \infty} H^{6s}(\rho, \phi) \approx -\hat{z} I_{MLS} \frac{\omega \epsilon_6}{4}$$
$$\times \left\{ \sqrt{\frac{2}{\pi k_6}} e^{j\frac{\pi}{4}} \frac{e^{-jk_6 \rho}}{\sqrt{\rho}} \right\} \sum_{n=0}^{\infty} \tau_n j^n A_6^n \cos[n(\phi - \phi_s)] \tag{46}$$

Since the far field is transverse electromagnetic (TEM), the far-field relation $E_\phi^{ff} = \eta_0 H_z^{ff}$ simplifies calculating the total power radiated into the far field. Let S_∞ be the far-field cylindrical surface that encloses the combined MLS and cylindrical meta-structure. The time-averaged total radiated power can then be written with the far-field approximations of the total electric and magnetic fields in Region 6, $(E_{tot}^{ff}, H_{tot}^{ff})$, as:

$$P_{rad} = \frac{1}{2} \oint_{S_\infty} \Re\left\{ E_{tot}^{ff} \times \left(H_{tot}^{ff} \right)^* \right\} \cdot ds$$
$$= \frac{\eta_0}{2} \int_0^{2\pi} \left| H_{tot}^{ff}(\rho, \phi) \right|^2 \rho \, d\phi \tag{47}$$

where $ds = \hat{\rho} \rho \, d\phi$ is the outward pointing normal differential "surface" element of S_∞. As a result, the total radiated power (47) becomes

$$P_{rad} = \frac{\eta_0}{2} \int_0^{2\pi} \left| H_{tot}^{ff}(\rho, \phi) \right|^2 \rho d\phi = \frac{\eta_0}{2} \left(I_{MLS} \frac{\omega \epsilon_0}{4} \right)^2$$
$$\times \frac{2}{\pi k_0} \sum_{n=0}^{\infty} \tau_n^2 \left| A_n^6 \right|^2 \int_0^{2\pi} \cos^2 [n(\phi - \phi_s)] \, d\phi$$
$$= I_{MLS}^2 \frac{\omega \epsilon_0}{8} \sum_{n=0}^{\infty} \tau_n \left| A_n^6 \right|^2 \tag{48}$$

where the orthogonality of the basis (cosine) functions:

$$\int_0^{2\pi} \cos^2[n(\phi - \phi_s)] \, d\phi = \begin{cases} 2\pi & \text{for} \quad n = 0 \\ \pi & \text{otherwise} \end{cases}$$

has been used. The expression (48) is, of course, truncated to N terms when it is numerically evaluated. The 2D directivity, i.e., the radiation intensity in the far-field in the direction ϕ divided by the total radiated power per unit angle, i.e., $P_{\text{rad}}/(2\pi)$, takes the form:

$$D(\phi) = \frac{2\pi\rho \left|\boldsymbol{H}_{\text{tot}}^{\text{ff}}(\rho, \phi)\right|^2}{\int_0^{2\pi} \left|\boldsymbol{H}_{\text{tot}}^{\text{ff}}(\rho, \phi)\right|^2 \rho \, d\phi} \tag{49}$$

Since

$$\left|\boldsymbol{H}_{\text{tot}}^{\text{ff}}(\rho, \phi)\right|^2 = \left(I_{\text{MLS}} \frac{\omega\epsilon_0}{4}\right)^2 \frac{2}{\pi k_0} \left(\frac{1}{\sqrt{\rho}}\right)^2$$
$$\times \left|\sum_{n=0}^{\infty} \tau_n j^n A_n^6 \cos[n(\phi - \phi_s)]\right|^2$$

$$\int_0^{2\pi} \left|\boldsymbol{H}_{\text{tot}}^{\text{ff}}(\rho, \phi)\right|^2 \rho \, d\phi = \left(I_{\text{MLS}} \frac{\omega\epsilon_0}{4}\right)^2 \frac{4}{k_0} \sum_{n=0}^{\infty} \tau_n \left|A_n^6\right|^2$$

the directivity (49) takes the multipolar form:

$$D(\phi) = \frac{\left|\sum_{n=0}^{\infty} \tau_n j^n A_n^6 \cos[n(\phi - \phi_s)]\right|^2}{\sum_{n=0}^{\infty} \tau_n \left|A_n^6\right|^2} \tag{50}$$

As demonstrated in [169], the maximum of the directivity obtainable in a two-dimensional (2D) system capable of radiating N multipoles is

$$D_{N,\text{max}}^{\text{2D}} = 2N + 1 \tag{51}$$

It is linear in N rather than the quadratic nature of the 3D bound (1). This difference arises from the extra degrees of freedom tied to the third dimension. Furthermore, it was also demonstrated that the 2D upper bound on the directivity for an ideal, lossless, uniformly-illuminated system in terms of its size is

$$D_{\text{2D,ub}} = \frac{2\pi W_{\text{eff}}}{\lambda_0} \tag{52}$$

i.e., it is proportional to the effective width, W_{eff}, of the 1D aperture. This 2D bound is in direct correspondence with the 3D area version (1).

For the symmetric cylindrical structure in Fig. 7 whose outer radius is r_5, the transverse width is simply its diameter, i.e., $W_{\text{eff}} = 2 r_5$. Consequently, a system with r_5 being λ_0, $\lambda_0/2$ and $\lambda_0/4$ is superdirective if its maximum directivity is greater than:

$$D_{\text{2D,ub}}^{\lambda_0} = 4\pi = 12.56 = 10.99 \, \text{dB}$$
$$D_{\text{2D,ub}}^{\lambda_0/2} = 2\pi = 6.28 = 7.98 \, \text{dB}$$
$$D_{\text{2D,ub}}^{\lambda_0/4} = \pi = 3.14 = 4.97 \, \text{dB} \tag{53}$$

Furthermore, as discussed in [169], the general bounds are attained with a needle-beam solution which can be realized

with Dirac-delta function-based coefficients. In particular, the cylinder expansion closure relation can be written in the distribution form [179]

$$\delta(\phi - \phi_0) = \frac{1}{2\pi} + \frac{1}{\pi} \sum_{m=1}^{\infty} \cos[m(\phi - \phi_0)] \tag{54}$$

This suggests that a needle-like outcome for an N-layer structure could be achieved by having the coefficients of the fields in its exterior region become:

$$A_{0,\delta}^{N+1} = \frac{1}{2\pi}$$
$$A_{m,\delta}^{N+1} = \frac{1}{\tau_m \pi j^m} \cos[m(\phi_{\text{max}} - \phi_s)] \quad \text{for } m > 0 \tag{55}$$

where ϕ_{max} is the desired direction of the maximum directivity. In particular, the directivity for an N-layer problem with the sum truncated to $M + 1$ terms, $0, 1, \ldots, M$ then becomes

$$D_M(\phi) \approx \frac{\left|1 + 2\sum_{m=1}^{M} \cos[m(\phi_{\text{max}} - \phi_s)] \cos[m(\phi - \phi_s)]\right|^2}{1 + 2\sum_{m=1}^{N} |\cos[m(\phi_{\text{max}} - \phi_s)]|^2} \tag{56}$$

With the desire in the example to have the meta-structure system convert the line source field into a directive beam along the $+x$-axis, one has $\phi_{\text{max}} = \phi_s = 0$. Since then $\phi_{\text{max}} - \phi_s = 0$, one then has $1 + 2\sum_{m=1}^{M} 1 = 1 + 2M$, and the directivity becomes

$$D_M(\phi) \approx \frac{\left|1 + 2\sum_{m=1}^{M} \cos(m\phi)\right|^2}{1 + 2M} \tag{57}$$

One recognizes immediately from (54) that as $M \to \infty$ in (57), needle radiation in the $\phi = 0$ direction is obtained, i.e., $D_{M\to\infty}(\phi) \propto \delta(\phi)$. The maximum directivity for a finite number of multipoles M is

$$D_{M,\text{max}}(\phi = 0) \approx \frac{\left|1 + 2\sum_{m=1}^{M} 1\right|^2}{1 + 2M} = 2M + 1 \tag{58}$$

which recovers the theoretical maximum in 2D.

A comparison of the directivities (in dB units) as functions of the observation angle ϕ exhibited by the $M = 5$, 20, and 100, multipole cases is shown in Fig. 8. The maximum directivity in each case is determined to be 10.41 dB (11), 16.13 dB (41) and 23.03 dB (201), confirming the $2M + 1$ upper bound. The FTBR for each case is, respectively, 20.83, 32.26, and 46.06 dB. The $N = 100$ case is clearly beginning to exhibit a needle-like, unidirectional behavior.

C. A 2D MULTIPOLE REALIZATION OF A SUPERDIRECTIVE ANTENNA

As noted in [168], Oseen was keenly interested in how a tiny atom might absorb a large electromagnetic wave as an equivalent photon and, consequently, the alternate translation of his paper's title as "pinprick" radiation might make
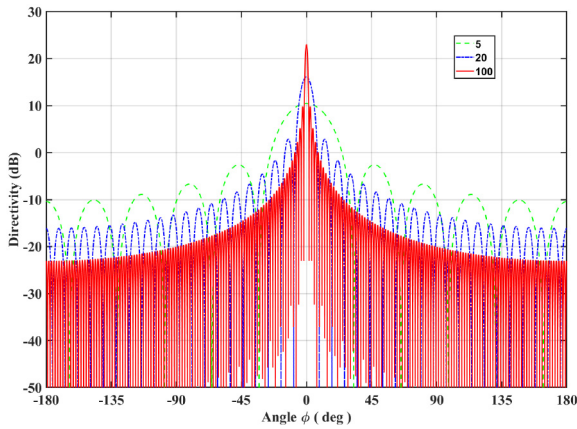
FIGURE 8. Comparison of the directivity arising from the superposition of the $M + 1$ multipoles with $M = 5, 20, 100$ and the Dirac-delta based weights (coefficients).

more historical sense. The reciprocal problem of transmitting a needle-like radiation pattern from a small source has stimulated many physics, if not many more engineering discussions. The role of superdirectivity in radio astronomy and in particle physics was discussed by Casimir and Puppi [180] and Wheeler [181]. They too emphasized the possibility that the effective receiving cross-section of a radio telescope or an atom could be extremely large in comparison to its physical size. This concept has been demonstrated more recently with plasmonic particles whose strong reactive scattering components extend to large distances and redirect the power passing through a large area of an incoming plane wave and force it to flow towards the scatterer [17], [18], [95], [149].

The engineering of the emission of electromagnetic fields from finite sources was intensely studied in the 1940's and 1950's soon after Oseen's publication. Both endfire [182] and broadside [183] pattern enhancements from different array configurations were considered initially. La Paz and Miller [184] purported to show that the maximum directivity from an aperture of a given size was fixed, but then Bouwkamp and De Bruijn [185] correctly demonstrated that there was no theoretical limit on the directivity from an aperture of any size. Dolph realized that one could control the sidelobe levels of the pattern by properly weighting (Chebyshev polynomial tapering) the amplitudes of the element excitations [186]. Dolph [187] and Riblet [188] illustrated that such amplitude tapering has an associated cost of widening the mainlobe of the pattern. However, it was quickly shown by Yaru [189] that the current distribution solutions that produce superdirective beams from arrays generally are ill-posed [190], i.e., small variations of the large positive and negative variations of the excitation amplitudes required to achieve the effect led to its disappearance in practice. In fact, Casimir [180] and Wheeler [181] noted this practical difficulty and believed that one would never go beyond combining a dipole and a quadrupole mode together in practice. Nonetheless, this goal has also been achieved with sub-wavelength dielectric and

plasmonic particles [127], [137], [151]–[154]. There have been and continue to be many examples of optimizing the directivity from an antenna system with constraints on its various other performance characteristics to circumvent the ill-posedness of the "super" outcome [191]–[195].

The concept of a transmitting antenna realizing a far-field needle radiation pattern is also intimately connected to subwavelength imaging, i.e., being able to resolve two small objects separated by subwavelength distances [196], [197]. Moreover, superdirectivity has been shown to lead to enhanced channel capacity in multiple input - multiple output (MIMO) systems [198]–[201]. Thus, superdirectivity concepts become yet again important as nano-technology applications flourish and the Internet of Things (IoT) comes to fruition. One simply would like to have electrically small, highly directive receiving or transmitting antennas (whether they are macro, micro or even nano) for numerous wireless applications.

A useful operational definition of superdirectivity, e.g., as emphasized by Hansen [202], [203], is to achieve a directivity greater than that obtained with the same antenna configuration being uniformly excited (constant amplitude and phase). As noted, the 2D directivity upper bound (51) was derived on the basis of this definition. Several subwavelength-sized 5-layer cylindrical antenna cases are presented to demonstrate the efficacy of the meta-structure in achieving high directivity and even superdirective results. In particular, it is shown that the HOMs facilitate this outcome. The values (53) will be used to determine if a case is superdirective or not.

Being a 2D problem, the forward direction is taken to be along the $+x$-axis where $\phi = 0°$. Three meta-structures with unidirectional forward-directed beams and one with a backward-directed beam are considered. The forward and backward cases have the outer radius $r_5 = 1.0\lambda_0$. The remaining two forward cases have $r_5 = \lambda_0/2$, and $\lambda_0/4$. In all of the forward-directed cases, the MLS is positioned along the $+x$-axis in Region 1 at the distance ρ_s. In the backward-directed case, the MLS is located in the exterior of the meta-structure along the $-x$-axis as it was in [169]. It is shared to illustrate a super-backscattering configuration.

The same optimization procedure employed in [169] that utilized the MATLAB *fminmax* routine was used to manually optimize r_i for $i = 1, 2, 3, 4$; the relative permittivities $\varepsilon_{\ell r}$ for $\ell = 1, \ldots, 5$; and the source location $(\rho_s, 0°)$ for all four cases. Given the number of adjustable variables (10), there are simply a very large number of possible solutions. The software could not provide a global maximum despite many cost function attempts. Optimizing with respect to the magnitude squared of the directivity relative to the reference delta-function based analytical solution yielded the best results with much human intervention. As a result, the design efforts have been rather cumbersome and laborious.

The $1.0\lambda_0$ forward-beam case is considered first. The relative permittivities in each region are $\varepsilon_{1r} = -0.289$, $\varepsilon_{2r} = 0.289$, $\varepsilon_{3r} = -0.292$, $\varepsilon_{4r} = 0.348$, $\varepsilon_{5r} = -0.528$, and with
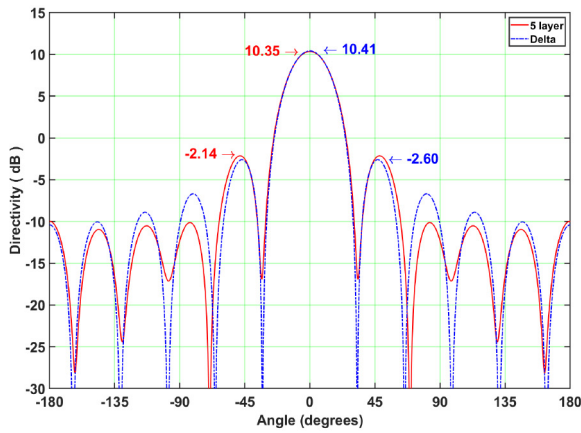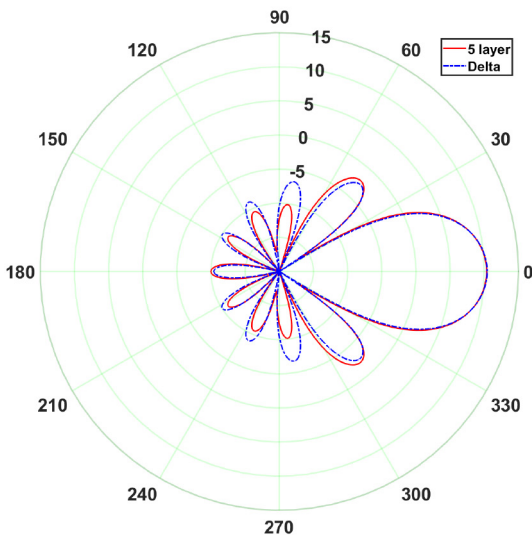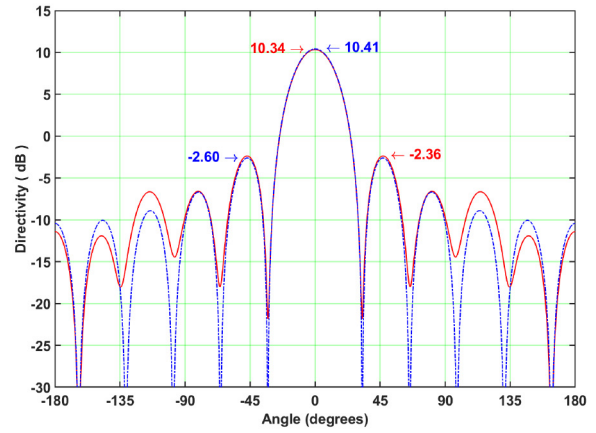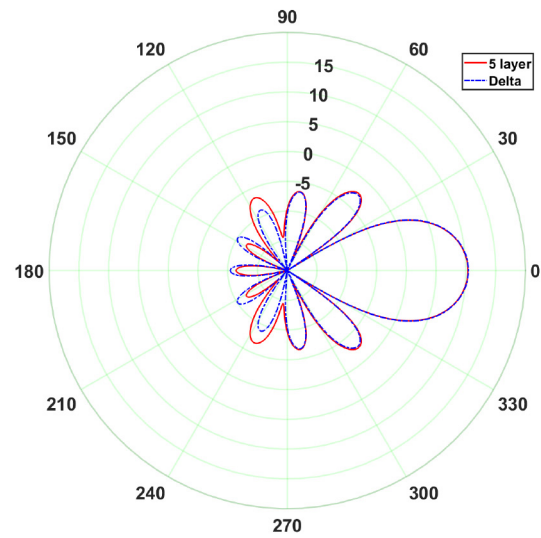
FIGURE 9. Comparison of the directivity of the 5-layer, $r_5 = 1.0\lambda_0$ metastructure and the ideal Dirac-delta based results. (a) xy-plot. (b) Polar plot, $D_{max} = 10.35$ dB.

FIGURE 10. Comparison of the directivity of the 5-layer, $r_5 = 0.5\lambda_0$ metastructure and the ideal Dirac-delta based results. (a) xy-plot. (b) Polar plot, $D_{max} = 10.34$ dB.

$r_5 = 1.0 \; \lambda_0$, the interior radii are $r_1 = 0.10 \; r_5, r_2 = 0.30 \; r_5, r_3 = 0.53 \; r_5, r_4 = 0.84 \; r_5$. The source is located at $\rho_s = 0.5 \; r_1$. It is immediately apparent that both ENG and DPS regions were required for the desired outcome for this case. However, other 2D superdirective configurations with positive-only dielectric constants have been demonstrated [169] and have been emphasized in 3D with HDC materials in related spherical multilayered geometries [176].

The directivity results are shown in Fig. 9 for the combination of the multipoles $0, 1, \ldots, 5$ in comparison to the ideal delta-based ones. As was emphasized in [169], the number of HOMs that contribute substantially to the results is essentially the same as the number of layers, i.e., $M = N$. The peak (ideal) directivity is 10.35 (10.41) dB, the first side lobe level is -2.14 (-2.60) dB, and the FTBR is 20.32 (20.83) dB. The optimized metastructure results are seen to be reasonably close to the ideal values. While not superdirective because

the peak value is just shy of the bound (53) by 0.64 dB, the peak directivity is indeed high for the size of the structure.

The $0.50\lambda_0$ forward-directed case has similar performance characteristics. The relative permittivities in each region are $\varepsilon_{1r} = -0.60, \varepsilon_{2r} = 0.60, \varepsilon_{3r} = -5.0, \varepsilon_{4r} = 0.644, \varepsilon_{5r} = -0.46$, and with $r_5 = 0.50 \; \lambda_0$, the interior radii are $r_1 = 0.10 \; r_5, r_2 = 0.272 \; r_5, r_3 = 0.45 \; r_5, r_4 = 0.80 \; r_5$. The source is located at $\rho_s = 0.54 \; r_1$ The directivity results are shown in Fig. 10 in comparison to the ideal ones for the same combination of the multipoles $0, 1, \ldots, 5$. The peak (ideal) directivity is 10.34 (10.41) dB, the first side lobe level is -2.36 (-2.60) dB, and the FTBR is 21.75 (20.83) dB. These results indicate that the pattern is superdirective according to (53), i.e., 10.34 dB is greater than the 7.98 dB value by 2.36 dB.

Since it is the first example herein of a superdirective antenna, the total magnetic field intensity distribution near
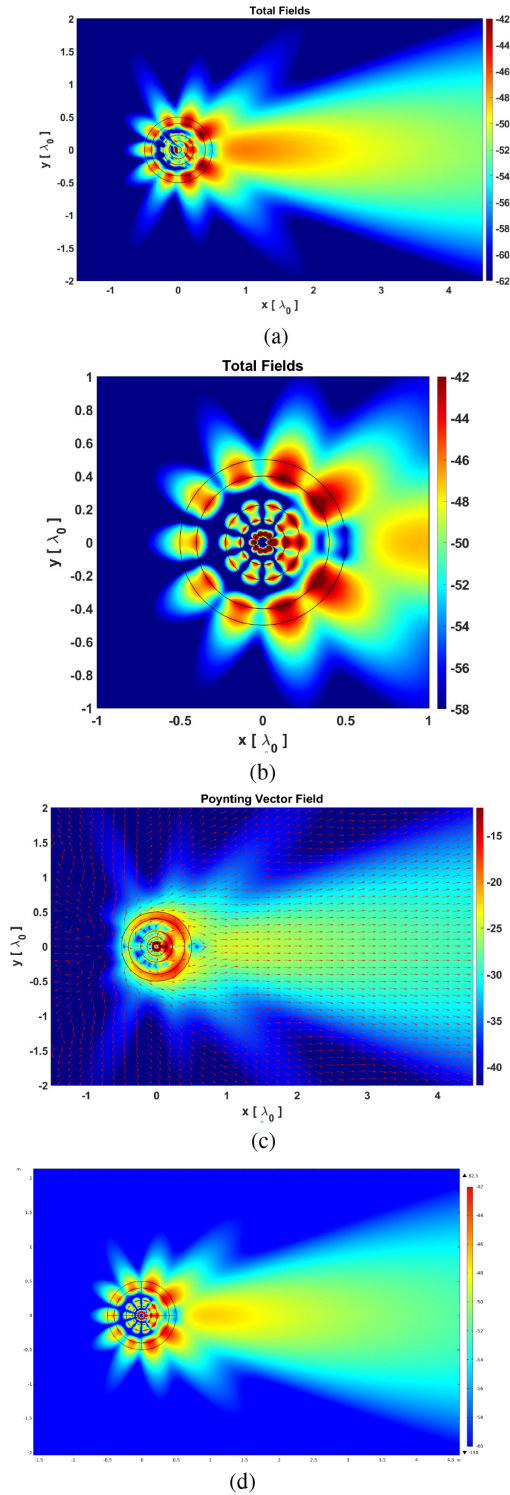
(a)

(b)

(c)

(d)

FIGURE 11. The intensity distributions and power flow near the 5-layer, $r_5 = 0.5\lambda_0$ metastructure. (a) Intensity: $10 \times \log_{10}(|H_z^{total}|^2)$. (b) Zoom-in of the intensity. (c) Poyntings vector field superimposed on the intensity distribution. (d) COMSOL simulated intensity. The color-bar values in all cases are given in dB. The x, y and color-bar values in (d) are identical to those in (a).

(a)

(b)

FIGURE 12. Comparison of the directivity of the 5-layer, $r_5 = 0.25\lambda_0$ metastructure and the ideal Dirac-delta based results. (a) xy-plot. (b) Polar plot, $D_{max} = 9.46$ dB.

the metastructure is presented in Fig. 11(a). A zoom-in of this intensity figure is given in Fig. 11(b). The presence of the HOMs is clear, notably the $M = 5$ mode. Its presence allows
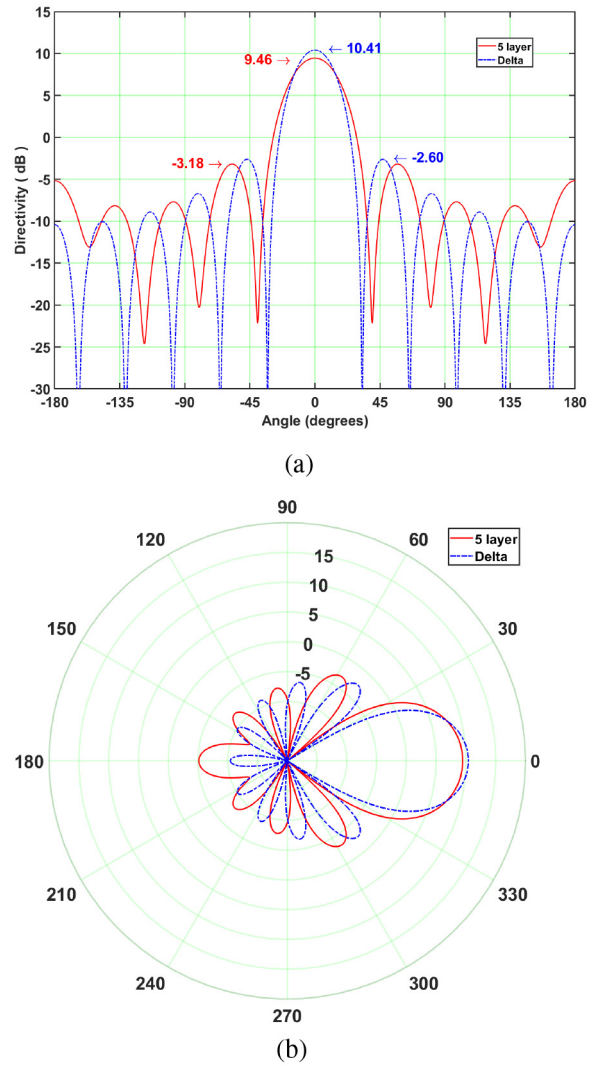
the peak directivity to approach the upper bound. Moreover, the interference of all of the modes yields the very low field levels in the back direction. The corresponding Poyntings vector field imposed on the distribution of its magnitude is given in Fig. 11(c). The definitive flow of power in the peak directivity direction is clearly seen.

To provide an independent confirmation of the analytical results, the problem was solved with COMSOL Multi-physics [204]. The simulated intensity distribution is presented in Figs. 11(d). Quite clearly, the result is quite close to the analytical one. The peak directivity was 10.09 dB and the FTBR is 21.75 dB.

The $0.25\lambda_0$ forward radiating case is considered as the remaining forward-directed one. The relative permittivities in region are $\varepsilon_{1r} = -10.0$, $\varepsilon_{2r} = 10.0$, $\varepsilon_{3r} = -4.75$, $\varepsilon_{4r} = 5.0$, $\varepsilon_{5r} = -0.6228$, and with $r_5 = 0.25\,\lambda_0$ the interior radii are $r_1 = 0.10\ r_5$, $r_2 = 0.265\ r_5$, $r_3 = 0.44\ r_5$, $r_4 = 0.84\ r_5$. The source is located at $\rho_s = 0.65\ r_1$ The directivity results are
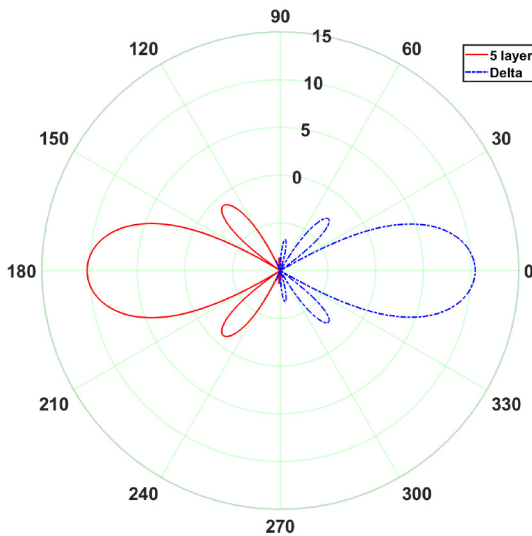
FIGURE 13. The directivity arising from the superposition of the multipoles with the MLS positioned in the exterior of the 5-layer, $r_5 = 1.0\lambda_0$ meta-structure at $(\rho_s, \phi_s) = (1.06\, r_5, 180°)$, $D_{max} = 10.25$ dB.

FIGURE 14. Three wire quadrupole antenna configuration.

shown in Fig. 9 for the same combination of the multipoles $0, 1, \ldots, 5$ in comparison to the ideal ones. The peak (ideal) directivity is 9.46 (10.41) dB, the first side lobe level is -3.18 (-2.60) dB. The FTBR is 14.62 (20.83) dB. These results indicate that the pattern is superdirective according to (53), i.e., 9.46 dB is greater than the 4.97 dB value by 4.49 dB.

Finally, the $1.0\lambda_0$ backward-directed case with the MLS exterior to the meta-structure is considered simply as a superbackscatter and for comparison with the corresponding forward-directed one. The coordinates of the MLS are $(\rho_s, \phi_s) = (1.06\, r_5, 180°)$, i.e., it is located just exterior to the meta-structure along the $-x$-axis. The relative permittivities in the various regions are $\varepsilon_{1r} = -0.92$, $\varepsilon_{2r} = 0.92$, $\varepsilon_{3r} = -1.20$, $\varepsilon_{4r} = 1.20$, $\varepsilon_{5r} = -0.29$, and with $r_5 = 1.0\,\lambda_0$ the interior radii are $r_1 = 0.10\,\lambda_0$, $r_2 = 0.30\,\lambda_0$, $r_3 = 0.70\,\lambda_0$, $r_4 = 0.90\,\lambda_0$. The directivity results are shown in Fig. 13 for the combination of the multipoles $0, 1, \ldots, 5$ in comparison to the ideal forward directed ones. The peak directivity is 10.25 dB, the first side lobe level is -0.97 dB, and the FTBR with respect to the peak directivity direction, $\phi = 180°$, is 19.60 dB. The first sidelobe level is higher than its value in the forward-directed case; the HOM set is not as effective in achieving the same level of destructive interference away from the peak direction. When the radius r_5 becomes even smaller, e.g., $\lambda/10$ as was considered in [169], backward-directed beam cases have been found to be more common with the brute force optimization approach for such an exterior source configuration.

VI. GENERATING MULTIPOLES
A wide variety of electrically small Huygens dipole antennas (HDAs) have been developed recently. These unidirectional antennas are based on the near-field resonant parasitic (NFRP) paradigm [205]. 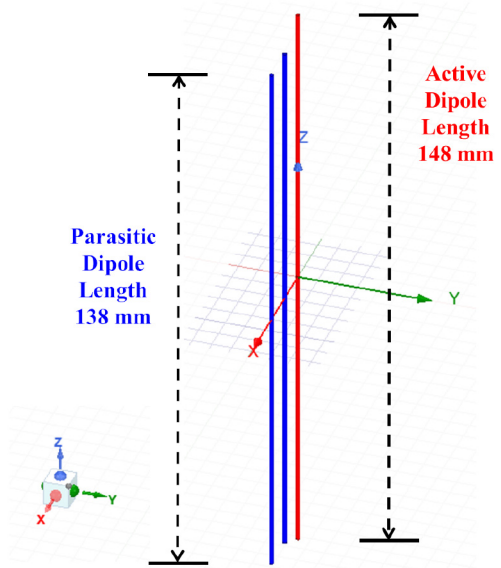They are realized with the described balanced, in-phase electric and magnetic dipole NFRP elements. They are efficient and are readily matched to the specific impedance of a source or device such as a rectifying circuit or sensor. Examples include basic passive and active; multi-band and multi-functional; frequency-agile and other reconfigurable feature systems [166], [206]–[224]. As examples of electrically small antennas, many of these systems have been recently reviewed [225]. The unidirectional ME dipole antennas are larger examples of magnetic-electric dipole-based systems [226]–[230]. Other dipole-based systems include quasi-isotropic antennas in which the electric and magnetic dipoles are 90° out-of-phase, e.g., [231], and omnidirectional antennas in which they are in-phase and parallel to each other [232].

While multipoles are quite interesting theoretically and, as demonstrated, facilitate rather exotic phenomena when complex materials are introduced, can one design antenna structures that will directly radiate HOM fields and/or their combinations? There have not been many multipole antennas discussed in the literature. One of the oldest ones that I have found is associated with the discussion of the equivalence theorem by Rumsey [170], in which he considered both electric and magnetic cylindrical quadrupole concepts along with the related dipole ones. Furthermore, we have recently demonstrated a unidirectional broadside-radiating quadrupole antenna [233] based on the wire concepts shared next.

A. WIRE-BASED MULTIPOLES
A basic HOM electric antenna that could radiate a quadrupole mode and/or its combination with a dipole mode is readily realized with wires. Consider the 3-wire configuration shown in Fig. 14. The frequencies of interest are taken to be very near to 1.0 GHz at which the free-space wavelength

is $\lambda_0 = 300$ mm. Each wire is parallel to the z-axis and has a 0.5 mm radius. All three dipoles were taken to be perfect electric conductors (PECs) and, hence, the system is lossless for simplicity.

The wire along the z-axis is the driven element. It is centered with respect to the origin and is 148 mm long, i.e., it is almost a half-wavelength long. It has a 1.0 mm gap cut out from its center. A lumped source is introduced in this gap in the ANSYS EDT (Electronics Desktop) v2021-R1 (formerly HFSS, High Frequency Structure Simulator) simulation model. No major attempts to achieve significant matching levels in the examples below were made. The impedance of the lumped source was adjusted in each case to match that of the driven element.

The other two wires are 138 mm long and centered along the x-axis. There is a 10 mm ($\lambda_0/30$) separation between each wire. The driven wire excites these two NFRP wires. The nearest parasitic wire will be referred to as Dipole1 and the second as Dipole2. The markers $m1$ and $m2$ found in all of the patterns of these wire-based cases represent the directivity at $\phi = 0°$ (along the +x-direction) and $\phi = 180°$ (along the −x-direction), respectively.

Note that one major concept related to this discussion that many researchers in the physics, optics, and antennas communities have gotten incorrect is that two nearby parallel wires, half-wavelength in size (particularly considered in optics-nano meta-designs) will radiate a magnetic dipole, e.g., [71], [234]. As illustrated above, below and in [233], this configuration produces a quadrupole field. Why has there been some confusion? Recall that Fig. 2 shows that while the electric vector field created broadside to a dipole current element has the same orientation on opposite sides of it, the electric vector field of an electric quadrupole (EQ) element has the opposite orientation. Furthermore, it was indicated with (5) to be the same for a magnetic dipole (MD) element.

The telling difference between the MD and EQ patterns is that the MD one has a donut shape with its null being along the dipole's direction and the EQ one has basically a null plane orthogonal to the plane containing the two dipole elements. Consequently, the vector directions of the fields are not a sufficient indicator of the mode. The other issue is that when one simulates a MTM or MTS that has a two-wire unit cell, the structure is actually infinite along the directions parallel to the wires. The "gremlin" at infinity provides the turning currents there that one would have in an authentic loop of current, i.e., the combined infinite current and return current paths emulate a loop current. There is no actual turning current available (and the displacement currents at either end are not strong enough) to produce the magnetic dipole response for a pair of finite length conductors. Because there is a turning current in a U-shaped conductor, it does yield a magnetic dipole response. Moreover, it also produces dipole and other HOM responses of different strengths [62].

The simulated responses of the three-wire system are presented in Fig. 15. It is intuitive that Dipole1 would be expected to have a current induced on it that flows in the
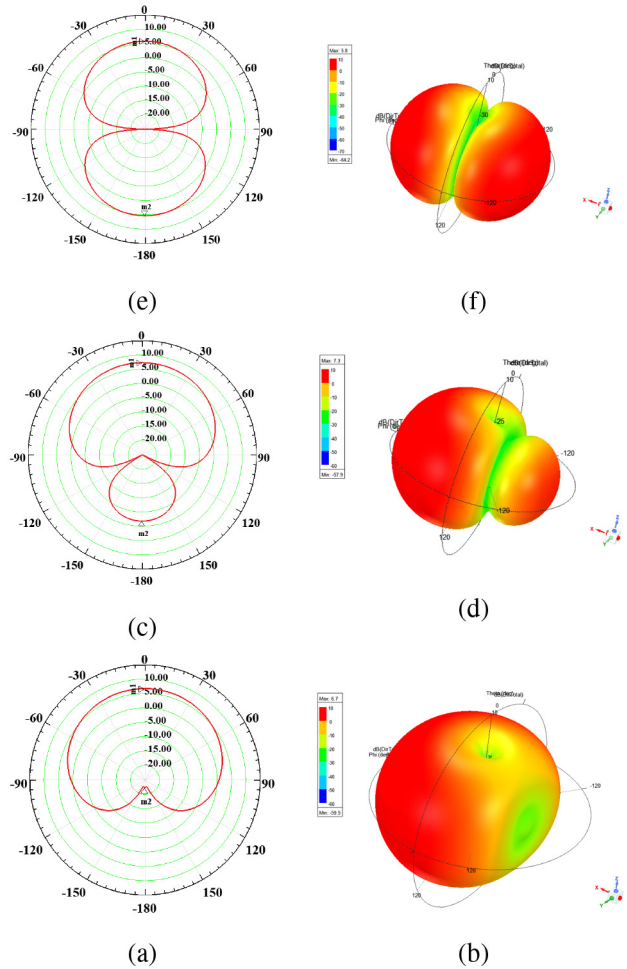

(e)

(f)

(c)

(d)

(a)

(b)

FIGURE 15. The 2D and 3D directivity patterns of the 3-wire configuration. (a), (b) 1.0453 GHz. (c), (d) 1.0075 GHz. (e), (f) 0.9825 GHz. All data is given in dB.

direction opposite to the one on the driven element. The 2D and 3D directivity patterns for the impedance matched resonance at 1.0453 GHz are shown in Figs. 15(a) and 15(b), respectively. The quadrupole pattern is clearly seen. The unexpected feature is that while the currents on the two parasitics at this resonance are opposite and quite large, those on the driven element are comparatively much smaller. The quadrupole pattern is thus formed primarily by the two NFRP elements. The current direction on the driven dipole and Dipole2 are the same whereas it is opposite on Dipole1. The patterns are a slight distortion from ideal since $m1 = 5.18$ dB and $m2 = 5.97$ dB, i.e., the lobe in the −x-direction is slightly larger. This is simply caused by unequal current magnitudes on the parasitics and the small current magnitude on the driven element.

Similarly, the 2D and 3D directivity patterns for the three-wire system at 1.0075 and 0.9825 GHz are presented, respectively, in Figs. 15(c), (d) and 15(e), (f). The 1.0075 patterns are the result of strong currents on the driven dipole, but the same current directions on both Dipole1 and Dipole2 in opposition to them. Those on Dipole2 are larger than the
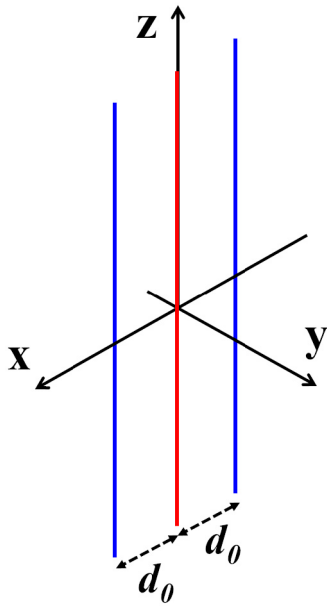
FIGURE 16. 3-wire array configuration. The length and radius of all 3 wires are 141.0 mm and 0.5 mm, respectively. Their different colors simply indicate which element is on the z-axis (red) and which are offset from it (blue). The elements are separated by the distance d_0.

ones on Dipole1. The patterns thus represent an unbalanced dipole and quadrupole combination that leads to the consequent and noticeable back lobe seen in Figs. 15(c), (d). The peak directivity is 7.26 dB and the FTBR = 9.01 dB. Again, the FTBR = $D(\phi = 0°)/D(\phi = 180°)$ for this configuration.

The 0.9825 GHz patterns are the result again of strong currents on the driven dipole and opposite but same current directions on Dipole1 and Dipole2. However, those of Dipole2 are now only slightly larger than those on Dipole1. On the other hand, the currents on the driven dipole are much larger than those in the 1.0075 case. A more balanced dipole and quadrupole response results which leads to the very good cardioid patterns observed in Figs. 15(e), (f). The peak directivity is 6.71 dB and the FTBR = 28.58 dB.

The 3-wire system allows another interesting study – that of a 3 wire array in which all of the elements are excited independently. All 3 electric dipoles are oriented parallel to the z-axis; the center wire is coincident with it. The other two are separated symmetrically from it along the x-axis by the distance d_0. This configuration is shown in Fig. 16. It facilitates a direct comparison of one dipole, the difference-quadrupole, and their combination as they were considered with the elemental dipole configurations in Section V. Moreover, in contrast to the previous 3-wire active-parasitic case, this system has the dipole and difference-quadrupole phase centers being coincident. Each dipole is excited with a 1.0 GHz ($\lambda_0 = 299.79$ mm) source. Each has the length $L_{FLD} = 141.0$ mm $= 0.47 \lambda_0$.

The analytical model of the directivity was constructed in MATLAB using the well-known formulas for the finite-length z-oriented electric dipole [9, (4-62b)] whose pattern

is specifically:

$$\mathcal{P}_{FLD} = 2 \frac{\cos\left[\frac{k_0 L_{FLD}}{2} \cos\theta\right] - \cos\left(\frac{k_0 L_{FLD}}{2}\right)}{\sin\theta} \quad (59)$$

The amplitudes of the center and offset dipoles are A_{ED}, A_{QD+}, and A_{QD-}, respectively. Setting the difference-quadrupole amplitudes to be: $A_{QD+} = -A_{QD-} = A_{QD}$, the array factor becomes

$$AF_{3-\text{wire array}}(\theta, \phi) = A_{ED} + 2jA_{EQ}\sin(+jk_0d_0\sin\theta\cos\phi) \quad (60)$$

In contrast to the usual process of wanting to maximize the gain of the array, I choose to optimize to ensure that there is no backlobe in the xy-plane, i.e., to have $AF_{3-\text{wire array}}(\theta = \pi/2, \phi = \pi) = 0$. This criterion is clearly satisfied if

$$A_{ED} = +2jA_{EQ}\sin(+jk_0d_0) \quad (61)$$

To further simplify the example, I take $A_{ED} = +j$ and $A_{EQ} = 1.0$ and solve for the d_0 that satisfies this constraint. One finds $d_0 = 0.0833 \lambda_0$.

The directivity patterns in the E (zx)-plane and H (xy)-plane are presented in Fig. 17. The peak direction in all three cases was along the endfire direction, which was selected to be along the +x-axis. With $A_{ED} = 1.0$ and $A_{EQ} = 0$, the peak magnitude of the dipole configuration is 2.10 dB. With $A_{ED} = 0.0$ and $A_{EQ} = 1.0$, the peak magnitude of the difference-quadrupole configuration is 5.84 dB. With $A_{ED} = +j$ and $A_{EQ} = 1.0$, the peak magnitude of the dipole-quadrupole configuration is 6.59 dB. The FTBR value in the difference-quadrupole and dipole-quadrupole cases is infinite. In contrast to the previous HDA versions, one clearly sees that the patterns in the principle zx-plane which contains the dipoles and the principle xy-plane orthogonal to that plane are different. As one would expect because the electrical length of the array is only 0.167 λ_0, the H-plane patterns are broader than the E-plane ones.

It is interesting and important to emphasize that the dipole and difference-quadrupole elements must be out-of-phase by 90° to obtain the desired null backlobe. This fact in the analytical N-element Huygens multipole systems was not immediately apparent because the amplitudes were normalized to obtain the needle-like outcome. Because each difference-N-multipole result comes from the derivative of the (N − 1)-multipole, they are actually different by a factor of +j as explicitly shown in this dipole-quadrupole example. It was not an explicit issue in the previous 3-wire case because two of the elements were parasitic wires. The difference in electrical lengths of the wires in the cardioid pattern case provided the necessary phase differences to obtain its very low backlobe. On the other hand, the explicit phase difference in the amplitudes is needed in this 3-active wire system because of the desire for the 3 dipoles to work together in a controlled collaboration.

The numerical (ANSYS EDT) model differs from the analytical one simply by the facts that the wires have a thickness,
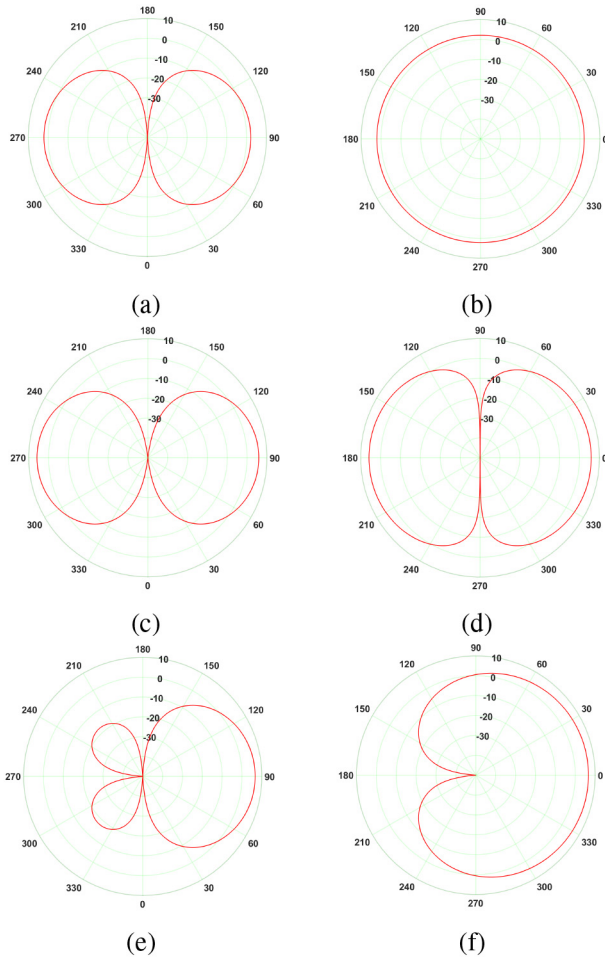
FIGURE 17. The 3-wire array directivity patterns (dB). (a) Dipole E-plane. (b) Dipole H-plane. (c) Quadrupole E-plane. (d) Quadrupole H-plane. (e) Dipole-quadrupole E-plane. (f) Dipole-quadrupole H-plane.
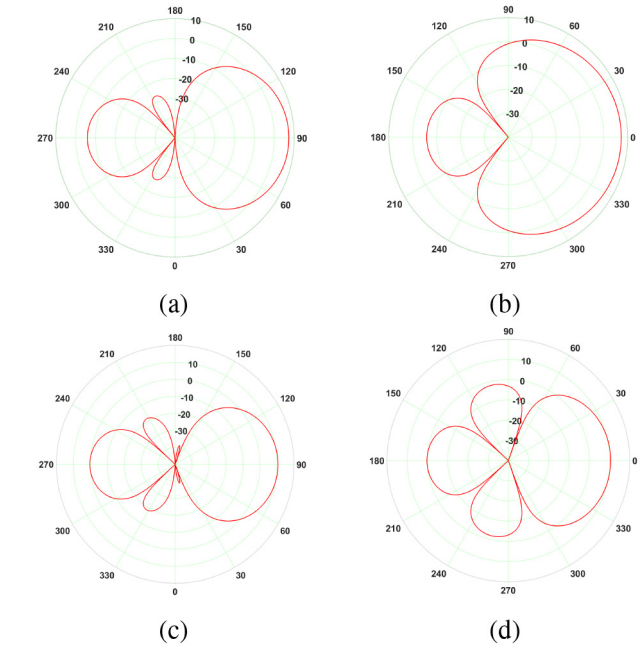

FIGURE 18. Directivity patterns (dB) for the 3-wire array. The ED-EQ array when $d_0 = 0.025\lambda_0$: (a) E-plane, (b) H-plane. The superdirective array with $d_0 = 0.01\lambda_0$: (c) E-plane, (d) H-plane.

a lumped source is explicitly present in each, and the interactions of the dipoles are taken into account by the software. The radius of each dipole was 0.5 mm and d_0 was rounded off to 25.0 mm. The lumped source was integrated across a 0.5 mm gap that was cut in the center of each dipole.

The numerical electric dipole, difference-quadrupole and dipole-quadrupole cases were simulated separately. The patterns of the dipole and difference-quadrupole cases at 1.0 GHz have the same shape as the analytical ones. Their peak directivity was 2.44 dB and 6.20 dB, respectively. The radiation efficiency was near unity. The patterns of the combined dipole-quadrupole (ED-EQ) system were obtained with the dipole's current amplitude being $A_{ED} = 1.0\underline{/101°}$ and the current amplitude of the difference-quadrupole $A_{EQ} = +1.0$. They were very similar to the analytical patterns except for the fact that there were tiny backlobes. In particular, the peak directivity was 6.88 dB and the FTBR was 45.45 dB in both the E- and H-planes. Thus, the numerical results were in very good agreement with the analytical ones. Note that the phase of the center dipole was slightly different from 90°; its value was found by manually minimizing the backlobe level using the ANSYS EDT edit source feature.

The analytical model was also used to determine the maximum directivity of the ED-EQ 3-wire array at 1.0 GHz. With $d_0 \to 0$, it is 7.47 dB. Moreover, it was used to explore as a comparison, the patterns that could be obtained with a specified small separation distance between the dipoles rather than guaranteeing an infinite FTBR. For instance, it was taken to be $d_0 = \lambda_0/40$ in order that the array's total length be $\lambda_0/20$. With $A_{EQ} = +1.0$ and d_0 fixed, the magnitude of A_{ED} was scanned to study at which value it yielded the peak directivity and minimum backlobe. The peak directivity, 7.46 dB, occurred when $A_{ED} = 0.13\,j$, i.e., it required the dipole field strength to be lower and better matched to that of the quadrupole. However, the FTBR was quite poor being only 7.68 dB, i.e., the backlobe level was only -0.22 dB. A -66.95 dB backlobe occurred when $A_{ED} = 0.313\,j$, but the peak directivity was low, being only 6.63 dB. An attractive in-between case with $A_{ED} = +0.2\,j$ yields 7.26 dB for the peak directivity with a 13.15 dB FTBR. The E- and H-plane directivity patterns for this last case are presented in Figs. 18(a) and (b), respectively. The presence of nontrivial backlobes is immediately apparent. It is now quite clear from all of these 3-wire dipole-quadrupole array results that the penalty for a higher peak value is a larger backlobe, i.e., the desired unidirectional performance must be sacrificed to some degree. Nevertheless, many of their properties are quite attractive given how short the overall array length is. A prototype experiment is being planned to further explore the potential of these types of mixed-multipole wire-based configurations.

The investigation of the superdirective properties of arrays has a long engineering electromagnetics history.

Uzkov provided a superdirective bound for linear endfire dipole arrays of closely spaced elements [235]. The subsequent investigations of such super-directive endfire dipole arrays both in theory and experiment have confirmed this bound [236]–[242]. The excitation amplitudes required to attain a superdirective result for the 3-wire system with $d_0 = 0.01 \lambda_0$ were obtained using (A.13), (A.14) and the associated dipole footnote of [236]. This method follows from pattern optimization analyses, e.g., [243], [244]. It yielded: $A_{\text{QD}-} = 10^{+3} \times (-2.34446 - 0.11760i\ j)$, $A_{\text{ED}} = 10^{+3} \times (4.68296 + 0.29463\ j)$, and $A_{\text{QD}+} = 10^{+3} \times (-2.34071 - 0.17717\ j)$. The E- and H-plane directivity patterns for this superdirective case are presented in Figs. 18(c) and (d), respectively. The peak directivity is indeed the 3-element bound: 10.54, but the FTBR is only 10.29. While the forward beam in the E-plane is narrower and, hence, more directive than the dipole-quadrupole case, the backlobe and back sidelobe levels are noticeably higher. Note that all of the indicated decimal places and the interelement spacing that is even smaller than the reasonable FTBR ED-EQ example were required or the patterns degraded. Moreover, note the extremely large positive and negative amplitudes required in this very densely packed array, i.e., this example nicely illustrates the sensitivity of this particular superdirective configuration and the general reason for the historical stigma associated with superdirective arrays.

To further appreciate the performance choices one can make with multipole designs, let us return to a two-element elemental dipole array. It readily clarifies the tradeoffs between the optimized cardioid FTBR system and the supergain-based peak directivity one. Thus, consider again the system with two elemental electric dipoles oriented along the y-axis in opposite directions, centered with respect to the origin, and separated along the z-axis from the origin by the distance d_z. The corresponding two element array factor is:

$$AF_{\text{quad}}(\theta, \phi) = A_+ e^{j k d_z \cos \theta} - A_- e^{j k d_z \cos \theta} \quad (62)$$

One then simply wants $AF_{\text{quad}}(\theta = \pi, \phi) = 0$ to obtain a zero backlobe. This is readily achieved, independent of the size of $k d_z$, with the amplitude relation:

$$A_+ = A_- e^{+j 2 k d_z} \quad (63)$$

Note that the magnitude of both dipoles are the same; only a phase difference is required. Setting $A_- = 1.0$ and, hence, $A_+ = \exp(+j 2 k d_z)$, the directivity patterns shown in Fig. 19(a) and (b) were obtained with $k d_z = 0.005$. The cardioid outcome is quite clear, i.e., the peak of the directivity is along the +z-direction and the FTBR $= \infty$. The peak value is 6.32 dB and the sidelobe level in the back direction is −11.74 dB, i.e., it is 18.06 dB below the peak value. To illustrate that the effect is maintained even with a factor of 10 larger $k d_z$ value, i.e., with $k d_z = 0.05$, the peak value is 6.31 dB and the sidelobe level in the back direction is −11.73 dB (18.04 dB below the peak value). Note that with $A_+ = \exp(-j 2 k d_z)$, the patterns are inverted and the peak of the cardioid pattern is then along the −z-axis.
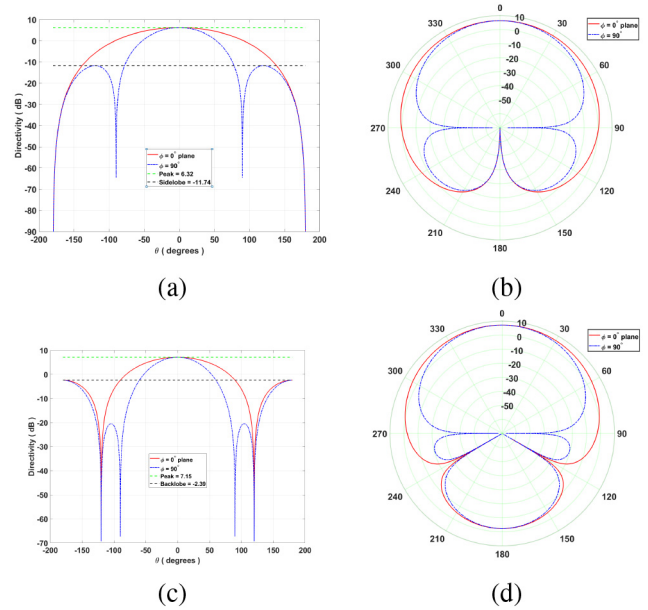

FIGURE 19. Directivity patterns (dB) in both principle planes for optimized two-element dipole arrays based on the quadrupole concepts. The no-backlobe solution: Directivity (a) xy-plot, and (b) pattern. The maximum directivity solution: Directivity (a) xy-plot, and (b) pattern.

On the other hand, the two-element dipole array version of the supergain endfire solution [236] is a straightforward matrix calculation. A simple approximation to that result when $k d_z \ll 1$ was obtained:

$$A_+ \approx A_- e^{+j k d_z} \quad (64)$$

Again with $A_- = 1.0$, one then has $A_+ \approx \exp(+j k d_z)$. The directivity patterns shown in Fig. 19(c) and (d) are obtained with $k d_z = 0.005$ and begin to deteriorate for larger values. The peak directivity, 7.15 dB, is indeed along the +z-axis. However, notice the large backlobe. Its level is −2.39 dB, only 9.54 dB below the peak value. It is further noted that these maximum directivity patterns can be inverted to have the peak along the −z-axis. However, the coefficients are a bit more complicated. This outcome is obtained for $k d_z \ll 1$ with $A_+ \approx 1.0 - \exp(+j k d_z)$ and $A_- \approx \exp(+j k d_z) A_+$.

These two-element cases again clearly illustrate the tradeoff between the maximum FTBR and maximum directivity goals in such multipole designs. Moreover, it must be emphasized that the cardioid result was independent of the smallness of the $k d_z$ value, In contrast, the peak directivity case, as an example of this type of superdirective system, requires it and would suffer from the noted sensitivity issues in practice.

The optimization of circular arrays of dipole elements to attain superdirective behavior under various constraint conditions also has a long history, e.g., [245], [246]. Taking into account their sensitivity to fabrication and positioning errors has helped lead to a variety of interesting superdirective systems over many past decades. The superdirective potential of circular arrays of wire dipoles has been re-discovered

recently in the physics community in relation to multipoles with the desire to achieve very high-Q systems, e.g., [247]. Harrington [248] studied similar high-Q systems from a more general network theory approach. Moreover, it is actually interesting to learn that the IEEE signals and sensors communities have published extensively on superdirective acoustic and electromagnetic circular *receiving* arrays designed specifically using multipole or, equivalently, eigenbeam concepts, e.g., [249]. For instance, there are a variety of optimized beamformers to achieve superdirective outcomes in the presence of signal-to-noise (SNR) constraints based on the superpositions of a number of different orders of eigenbeams. It will be interesting to consider the analogous concepts to develop higher-order multipole-based beamformers for 5G and beyond transmitting and receiving systems.

B. EDGE-BASED MULTIPOLES

Another approach to generating HOMs in a straightforward manner is associated with a current hot physics topic: bound states in the continuum (BIC). A BIC state represents a wave solution that remains localized even though it coexists with a continuous spectrum of radiating waves that can carry energy away. Quasi-BIC states are those with very high-Q, but not infinite. While BIC has its origins in quantum mechanics, it has recently been used, for example, to develop a variety of optics applications associated with Mie-tronics [250], [251].

I believe that the engineering electromagnetics community has studied numerous quasi-BIC systems for decades, i.e., open resonators whose window to the continuum is tiny. Consider, for instance, the 3D or 2D aperture coupling problems of a perfect electric conductor (PEC) spherical shell with a circular aperture (open sphere) [33], [40], [41] or an infinite PEC circular cylinder with an infinite axial slit (open cylinder) [37]–[39], [252]. The interior modes of these open spheres or cylinders are discrete positive energy states and those exterior to it form a continuum of energy states. The hole or slit facilitates the coupling of the discrete and continuum states. Different objects in the interior modify the frequencies of the discrete states, i.e., the resonant modes of the structure.

While the interior resonant modes of an open scatterer become "hidden" when its aperture becomes closed, they still remain an issue when method-of-moments (MOM)-based CEM tools are used to calculate the fields in its exterior region. This issue was uncovered in the early days of CEM in regards to the then popular electric field integral equation (EFIE) approach [253]–[256]. It was found that bodies with closed conducting regions still support their set of discrete interior resonances when simulating their exterior behavior. This physical fact had originally given rise to numerical problems near these frequencies. They were found to be connected to the eigenmodes of the null space of the EFIE kernel with the boundary conditions associated, in particular, with the scattering objects.

The original aperture coupling studies were targeted to radar cross section and high power microwave (HPM) lethality and susceptibility issues associated with back-door coupling. Studies included both linear [38], [41] and nonlinear [257] interior elements as their properties and the size of the openings changed. The most recent investigation [252] considered passive and active metamaterial-based loadings. The basic physics associated with the edges of those openings and the confined states are of relevance to the HOM discussion.

The physics and engineering discussion will focus on the sphere case. Consider the fields scattered from the holey sphere (open resonator) when it is excited by a wave incident on it from a source in its exterior region. The currents induced on the sphere radiate the scattered fields. However, field singularities are present because of the edges of the hole (edge conditions, [258, Ch. 4]). To properly model the scattered fields with a mode-matching analysis, an infinite number of modes must be used to properly model the edge singularities to obtain the exact solution. A finite number of modes can lead to very useful approximate solutions when the HOMs have little influence on the results. The Riemann-Hilbert-based dual-series solution approach which was developed to analyze both the open sphere and cylinder problems handled their edge singularities by building them into the solution process. The interesting electromagnetics was that if the frequency of the incident field matched one of the interior resonant modes or an incident pulse contained it in its spectrum and even if the aperture was very small, energy would couple into the sphere and, as a consequence, the scattered field would contain information about that resonant mode. Similarly, if fields were excited in the interior of the resonator, the fields radiated into its exterior would have the wavelength of the resonant mode that created it. As the size of the aperture went to near zero, the amount of time for the ring-down of the cavity, i.e., the time over which the energy escaped from the cavity went to infinity, the lowest order mode being the last to exit the cavity. Another point of view is that the Q of the open resonator becomes extremely large as the aperture narrows and the Q value for the fundamental mode is the largest.

The presence of metallic and dielectric bodies within the cavity impacts the resonant modes and their resonance frequencies. As a consequence, the radiated fields contains information about those interior structures. Because of the edge singularities, the fields near the edges could be quite large, even to the point of causing breakdown in air. The resulting plasma in the aperture would decouple the interior and exterior regions. These aspects are all the hallmarks of a BIC/quasi-BIC system.

The engineering question then is whether or not one could use the HOMs excited by such edge-singularity fields to attain radiated fields having high directivities. Investigating a plane wave excited electrically small plasmonic nanoantenna (core-shell nanoparticle) version of the open sphere, we found that one could obtain highly directive near-fields
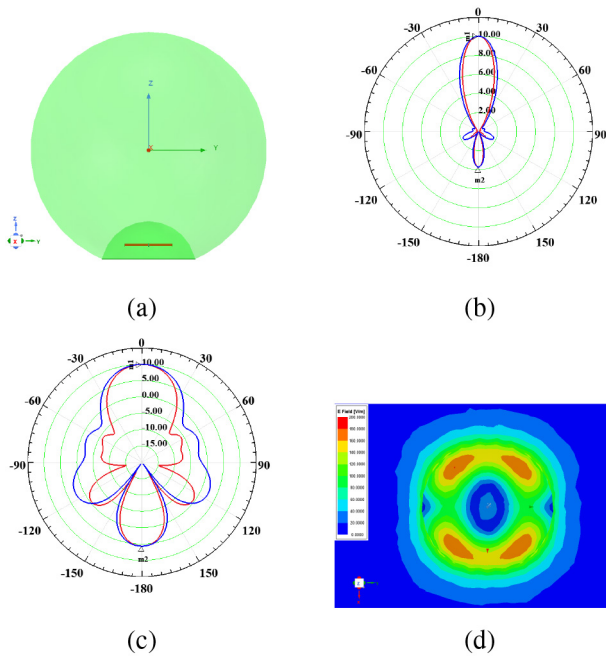
FIGURE 20. Dipole fed ceramic holey sphere radiator. (a) Side view of the configuration. (b) 2D directivity patterns (linear). (c) 2D directivity patterns (dB). (d) Electric field distribution in xy-plane within and near to the structure. Red and blue curves: patterns in the principle $\phi = 0°$ and $\phi = 90°$ planes, respectively.
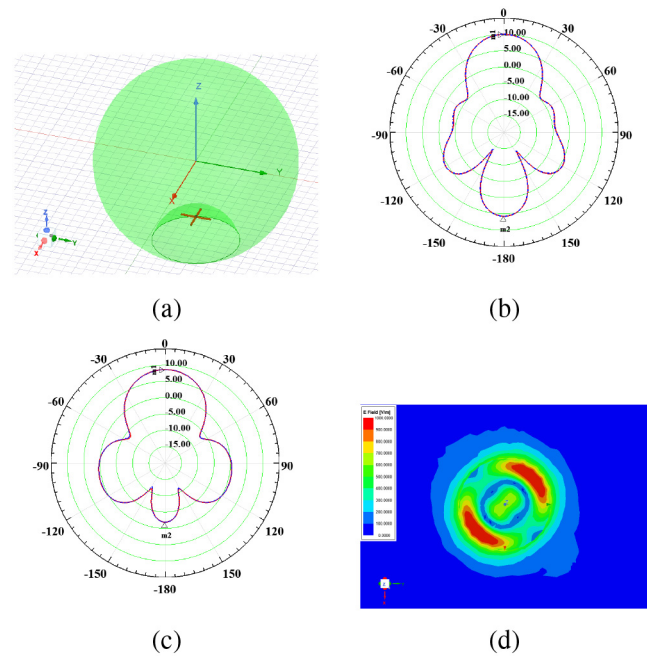
FIGURE 21. Cross-dipole fed ceramic holey sphere radiator (a) Isometric view of the configuration. (b) Directivity patterns (dB) at 16.8 GHz. (c) Directivity patterns (dB) at 17.8 GHz. (d) Electric field distribution in xy-plane within and near to the structure at 17.8 GHz. Red and blue curves: patterns in the principle $\phi = 0°$ and $\phi = 90°$ planes, respectively.

from such an open resonator [150]. These nanobeamer results compared very favorably to the localized nanojets produced by the plane wave excitation of the HOMs of electrically large dielectric spheres. However, because it was electrically small, the HOM effects gracefully degraded as the observation point moved into the far field and a dipole far-field pattern was finally obtained. On the other hand, it was demonstrated that HOMs impact the near- and far-field directivities and beam steering capabilities in the 2D passive and active open cylinder cases [252].

In contrast, it has been demonstrated that a dipole-excited, electrically large, ceramic-based sphere with a spherical notch cut from it does produce HOMs and consequent high directivity patterns in its far field [259], [260]. While the singularities at a dielectric edge are weaker than those at a metallic one, they nevertheless create HOMs. Guessing some specific details, the problem was reconsidered and simulated with the ANSYS EDT software. The configuration and its simulated performance are presented in Fig. 20. A sphere with radius $R_{cut} = 2.0$ mm was cut from a $MgO - TiO_2$ sphere with a dielectric constant of 16 and 1.5×10^{-4} loss tangent and with a radius $R_{sphere} = 5.0$ mm. The cut-out sphere was centered at $z = -R_{sphere}$. A dipole antenna oriented along the y-axis and centered along the z-axis was located at $d_{offset} = 1.0$ mm from the point $(0, 0, -R_{sphere})$. The radius and length of the dipole were, respectively, $r_{dipole} = 0.05$ mm and $L_{dipole} = 2.0$ mm. A gap of length $L_{gap} = 0.05$ mm was cut from the dipole and centered with respect to the z-axis. A lumped source was placed in this gap to excite the dipole at $f_{source} = 16.8$ GHz

($\lambda_{source} = 17.84$ mm). The dipole arms were taken to be PECs. Unlike the original models, no attempt to achieve matching to a 50-Ω source was made since the matching level has no impact on the directivity. The markers $m1$ and $m2$ found in all of the patterns presented for these cases represent the directivity at $\theta = 0°$ (along the +z-direction) and $\theta = 180°$ (along the −z-direction), respectively.

The 2D directivity patterns in the two principal planes (red curve, $\phi = 0°$, and blue curve, $\phi = 90°$) are presented in a linear scale, as they were depicted in [260], in Fig. 20(b) and in a dB scale in Fig. 20(c). The distribution of the magnitude of the electric field in the xy-plane is shown in Fig. 20(d). The markers in Figs. 20(b) and 20(c) are, respectively, $m1 = 10.02$, $m2 = 3.71$, and $m1 = 10.02$ dB, $m2 = 5.71$ dB. The system is electrically large with $ka = 2\pi R_{sphere}/\lambda_{source} = 1.76$. While the patterns in the linear scale are quite attractive, their dB versions indicates that while a large peak directivity along the +z-axis occurs, the back-lobe along the −z-axis is also large. The FTBR is only 4.31 dB. Moreover, the patterns are not symmetric in both principle planes because the source is linearly polarized and, hence, the system is not azimuthally symmetric. Taking the cross-section of the sphere, $A_{eff} = \pi R_{sphere}^2$ as its effective area, the resulting peak directivity is greater that $4\pi A_{eff}/\lambda_{source}^2 = 4.92$ dB. Thus, the system is superdirective. As the mode formed in the $MgO - TiO_2$ shown in Fig. 20(d) illustrates, a HOM is indeed responsible for the high peak directivity.

To explore the problem a bit further, the cross-dipole excitation configuration shown in Fig. 21(a) was simulated. The

design parameters of the dipoles were the same as in the single dipole case except that $L_{gap} = 0.12$ mm to prevent the two orthogonal dipoles from intersecting. The configuration parameters were modified slightly, i.e., $R_{sphere} = 5.0$ mm, $R_{cut} = 2.2$ mm and $d_{offset} = 1.8$ mm. The directivity patterns shown in Fig. 21(b) at 16.8 GHz confirm the symmetric cross-dipole excitation leads to azimuthally symmetric patterns. The markers are $m1 = 9.15$ dB, $m2 = 5.42$ dB. The FTBR is only 3.95 dB. On the other hand, it was found that a much improved FTBR value could be obtained with the penalty of a decrease in the peak directivity simply by changing the operating frequency. The directivity patterns obtained at $f_{source} = 17.8$ GHz ($\lambda_{source} = 16.84$ mm) are shown in Fig. 21(c). The markers are $m1 = 8.62$ dB, $m2 = -1.89$ dB. This symmetric system is also superdirective, but the FTBR is 10.51 dB. Both are attractive outcomes. The mode difference between the two configurations can be seen from Fig. 21(d). A lower order mode that is formed in the $MgO - TiO_2$ structure is responsible for the lower peak directivity and much improved FTBR results.

Several passive and active 2D and 3D cylindrical nano-antenna structures in which angular sectors have been removed simultaneously from both their plasmonic shells and dielectric cores have been studied [261]. Dipole or unidirectional patterns can be obtained with proper positioning of the exciting source both in the near and far fields. Moreover, as illustrated in 2D [252] and in 3D [259], [260], beam steering can be achieved by rotating the position of the exciting source with respect to the symmetry axis of the structure. The electric and magnetic dipole modes of a cylindrical dielectric resonator antenna (DRA) with a sector cut out of it confirmed the predicted the unidirectional properties of their combination [262].

Despite the high directivity and the fact that the peak directivity does not droop too much over the interval between the peak directivity and adequate FTBR frequencies, the patterns themselves change considerably over it. A closer look at Fig. 20(c) and Fig. 21(b) clearly reveals the influence of multiple modes on the patterns. Changing the frequency changes the amplitudes of the many modes that have been excited through the edge singularities. Since the far-field patterns are constituted as the superposition of the fields radiated by them, changes to their contributions to the net result causes non-trivial variations in the patterns. Nonetheless, like with the optimized metamaterial-inspired multilayered cylinder system, it is hoped that this negative feature could be resolved with proper sculpting of the high dielectric constant material to tailor the edge singularities or again considering structures formed with many concentric spherical layers with different dielectric constants *and* with appropriate spherical or cylindrical or conical cuts.

C. SINGLE-PORT MULTIPOLE ANTENNAS

As has been noted, it is difficult to find EM antennas in the literature that radiate a specific multipole. In a attempt to
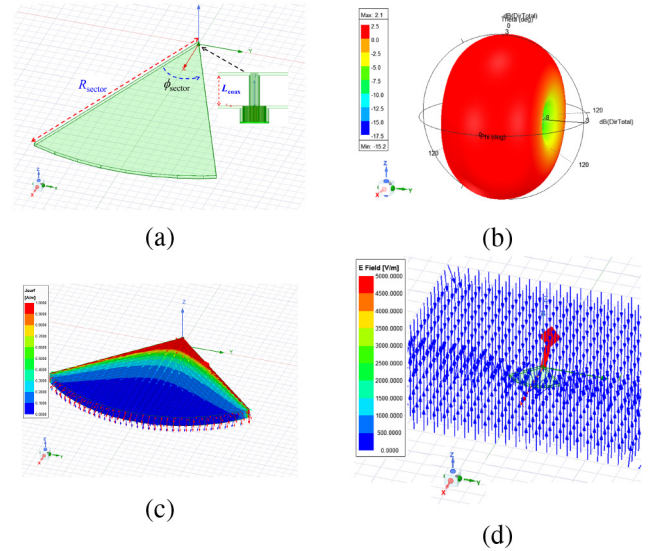

FIGURE 22. 1-arc sector antenna simulation results at 300 MHz. (a) Isometric view of the configuration. (b) 3D directivity pattern (dB). (c) Surface current magnitudes and vector field on the structure. (d) Near-field electric vector field. The single large red vector originates from the mouth of the coax.

determine if it would be straightforward to develop a single-port multipole antenna, the initial design shown in Fig. 22 was considered. It consists of two $\phi_{sector} = 45°$ copper sectors centered with respect to the x-axis and separated from each other with respect to the z-axis. The radius of the sectors is $R_{sector} = 100$ mm $= \lambda_0/10$. It is fed by an air-filled 50–Ω coaxial line. The inner end of the bottom sector is terminated on the outer conductor of the coax. The inner end of the top sector is terminated on the center conductor of the coax. The sectors are joined at their outer ends by a copper arc of vertical edge-to-edge length $= 6.75$ mm. The sides of the sector are open as illustrated in the inset of Fig. 22(a). Thus, the antenna is extremely low profile having a height $\lambda_0/148.15$. All of these copper pieces are 0.5 mm thick. The coax-length below the bottom conductor is taken to be 3.0 mm to minimize its computational burden. The source frequency is taken to be 300 MHz simply for convenience because its free space wavelength is $\lambda_0 = 1.0$ m.

This 1-arc sector antenna radiates as a magnetic dipole that is oriented along the +y-axis. Its 3D directivity pattern is shown in Fig. 22(b). The magnitude of the surface currents on the copper sector plates shown in Fig. 22(c) clearly indicate that they are concentrated mainly near their edges. The surface current vector field flows from the inner end of the top surface, down over the edge surface and then back under towards the outer wall of the coax. This forms the loop current corresponding to the magnetic dipole. The electric vector field in the region near the antenna is shown in Fig. 22(d). The net result is clearly vertically polarized (VP). It is interesting that the vector field has the orientation expected for the y-oriented magnetic dipole, but it extends further from the physical antenna as though the dipole element was much longer.
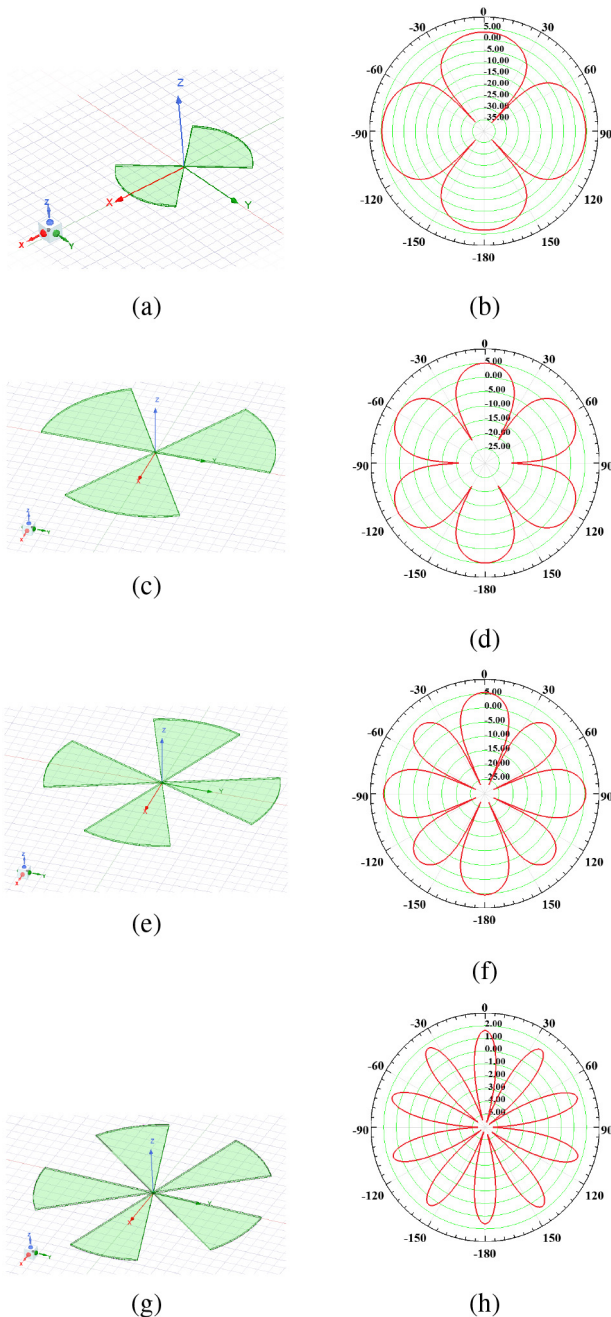
(a)

(b)

(c)

(d)

(e)

(f)

(g)

(h)

FIGURE 23. N-arc sector antenna simulation results at 300 MHz. (a) Isometric view of the 2-arc configuration. (b) 2D ($\theta = 90°$) pattern of this quadrupole configuration. (c) Isometric view of the 3-arc configuration. (d) 2D ($\theta = 90°$) pattern of this hexapole configuration. (e) Isometric view of the 4-arc configuration. (f) 2D ($\theta = 90°$) pattern of this octopole configuration. (g) Isometric view of the 5-arc configuration. (h) 2D ($\theta = 90°$) pattern of this decapole configuration.

The configurations of the N-arc sector VP antennas with $N = 2, 3, 4, 5$ and their patterns in the xy-plane ($\theta = 90°$) are shown in Fig. 23. The quadrupole ($N = 2$, $\phi_{sector} = 90°$), hexapole ($N = 3$, $\phi_{sector} = 60°$), octopole ($N = 4$, $\phi_{sector} = 45°$), and decapole ($N = 5$, $\phi_{sector} = 30°$) patterns are clearly seen. The radius of each sector in the $N = 2$ case was $R_{sector} = 250$ mm. It was $R_{sector} = 500$ mm in the $N = 3, 4, 5$ cases. It was found that as the number
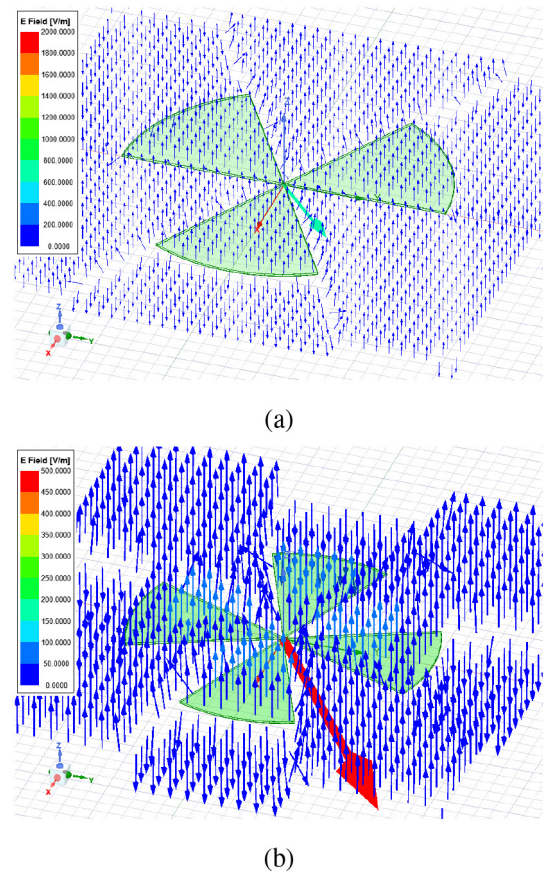

(a)

(b)

FIGURE 24. Electric field vectors near the N-arc sector VP antennas. (a) $N = 3$. (b) $N = 4$. The single, large blue and red vector in (a) and (b), respectively, originates from the mouth of the coax.

of sectors increased, the desire for better definition of the nulls was obtained with necessarily longer sectors and finer azimuthal angle samples. Nevertheless, given the character of the patterns, a set of single-port multipole antennas has been achieved.

Because of the $\cos N\phi$ nature of these patterns, an array of appropriately weighted N-pole antennas could produce a highly directive beam as indicated in the discussion of the N-layered meta-structured cylinder system. While the angular nature of the cancellations of the individual multipole patterns when they are superimposed is clear from (54), to see how the vector fields would cancel can be ascertained from Fig. 24. The electric fields near the hexapole and octopole antennas are presented (note that the single large vector in each subfigure originates at the mouth of the coax). One can clearly see the VP nature of the electric fields. Moreover, one can see how those fields are opposite over the metal sectors and air sectors. An appropriate superposition and orientation of the N-sector antennas could enhance and decrease the electric field strengths over the specified sectors of the azimuthal plane. However, note that unlike the 2D and 3D material-based structures with which $2N + 1$ (linear) and $N^2 + 2N$ (quadratic) enhancements were obtained, the directivities actually decrease some with the N-sector antennas
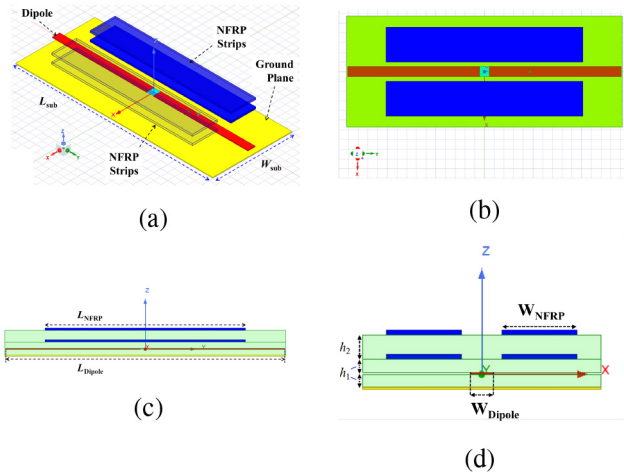
FIGURE 25. 28 GHz Quadrupole antenna with a ground plane. (a) Isometric view of the configuration. (b) Top view. (c) Side view. (d) End view.

as N increases. This feature is a direct consequence of generating all the sector beams at once, i.e., the source power is distributed to each sector (e.g., [146]). If all of the input power was distributed into only one sector, it is expected that these cylindrical-based sector antennas should, according to (51), have their directivity increase linearly with N.

D. USEFUL MULTIPOLE ADVANTAGE

Recall that it is difficult to achieve a very low-profile dipole antenna near to and parallel to a ground plane because its image in the opposite direction cancels the fields it radiates. As noted, similar issues generally arise with superdirective systems such as the circular array of dipole antennas. The cancellation leads to a very poor radiation efficiency. It is for this reason that artificial magnetic conductors (AMCs) were one of the first successful antenna applications of metamaterials [263]–[265]. Because the image of a horizontal dipole over an AMC is in the same direction, a theoretical factor of 2 advantage in the radiated field amplitude is obtained. On the other hand, as demonstrated with the 3-wire example and the quadrupole antenna developed in [233], these cancellation issues could be managed for HOM systems.

Recall also that a magnetic dipole parallel to a ground plane has its image in the same direction. As was noted, the same is true for an electric quadrupole, i.e., the electric multipole of order $M + 1$ will have the same image direction as a magnetic multipole of order M, for $M = 1, 2, \ldots$ Could one then obtain a high directivity, low profile HOM antenna over a ground plane in practice?

Consider the 28 GHz ($\lambda_0 = 10.7068$ mm) quadrupole antenna system shown in Fig. 25. This three substrate-layer configuration consists of a driven dipole, four NFRP elements, and a ground plane. The three dielectric layers are taken to be Rohacell with a dielectric constant of 1.06 and a 2×10^{-4} loss tangent. The Rohacell layers resting on the ground plane and on the dipole are $h_1 = 0.127$ mm thick. The top Rohacell layer is $h_2 = 0.0232$ mm thick.

The ground plane and all of the substrates have the same horizontal size: $L_{\text{sub}} = L_{\text{ground}} = 0.531 \lambda_0 = 5.684$ mm and $W_{\text{sub}} = W_{\text{ground}} = 0.213 \lambda_0 = 2.2875$ mm. The ground plane, dipole and NFRP elements are modeled as copper. The driven dipole lies on the xy-plane. The ground plane and dipole are both 0.017 mm thick. The horizontal size of the driven dipole is $L_{dipole} = 5.64$ mm and $W_{dipole} = 0.2098$ mm. A 0.2 mm long gap is cut out from the dipole symmetrically with respect to its center. A 50-Ω lumped source lies across this gap. The NFRP elements are planar strips that have $L_{NFRP} = 4.06$ mm and $W_{NFRP} = 0.72$ mm and are 0.05 mm thick. They are symmetrically offset from the y-axis by a horizontal distance from it to their inside edge of 0.195 mm along the x-direction.

The ground plane and the lower substrate are absent in the basic quadrupole antenna case. It is taken to be the reference design. It is a two-substrate layer version of the 28 GHz single-substrate layer quadrupole antenna reported in [233]. It can be considered as a 5 element variation of the 3-wire quadrupole case. The total height of the basic two-layer quadrupole antenna is $\lambda_0/25.13 = 0.426$ mm. It is $\lambda_0/18.78 = 0.570$ mm for the 3-layer ground-plane based quadrupole antenna. Hence, both are low-profile designs.

The simulated performance characteristics of the reference quadrupole antenna are presented in Fig. 26. The minimum $|S_{11}|$ value in Fig. 26(a) occurs at 28 GHz with $|S_{11}|_{\text{min}} = -22.02$ dB. The -10 dB bandwidth is 219 MHz (0.78%). Note that like a magnetic dipole antenna, this fundamental resonance of the quadrupole antenna is an antiresonance. As shown in Fig. 26(b), a quasi-unidirectional beam is generated at 28 GHz. The peak directivity marker, $m1 = 7.01$ dB, occurs along the +z-axis, i.e., along the broadside direction. The opposite directivity marker along the $-z$-axis is $m2 = -0.56$ dB. Thus, the FTBR is 7.57 dB. The overall (radiation) efficiency at 28 GHz is 96.5% (97.1%). Note that the 2D pattern in the $\phi = 0°$ plane is broader than the $\phi = 90°$ one because the antenna is narrower (longer) along the x-axis (y-axis). The 3D directivity pattern is presented in Fig. 26(c). The previously noted null plane of the quadrupole pattern is clearly seen.

The simulated performance characteristics of the ground-plane based quadrupole antenna are presented in Fig. 27. Note that the lower substrate and ground plane were simply introduced into the basic quadrupole antenna design without any further considerations. The minimum $|S_{11}|$ value in Fig. 26(a) occurs at 28.04 GHz with $|S_{11}|_{\text{min}} = -10.27$ dB. As shown in Fig. 26(b), a unidirectional beam is generated at 28 GHz. The peak directivity marker, $m1 = 6.68$ dB, occurs along the +z-axis, i.e., the broadside direction. The opposite directivity marker $m2 = -11.27$ dB. Thus, the FTBR is 17.95 dB. The overall (radiation) efficiency at 28 GHz is 81.2% (94.8%). The peak directivity at 28.2 GHz is higher at 6.97 dB and its FTBR is 30 dB. However, the overall (radiation) efficiency drops to only 18.7% (76.3%) because of the increased impedance mismatch and the currents being more concentrated on the NFRP elements alone causing
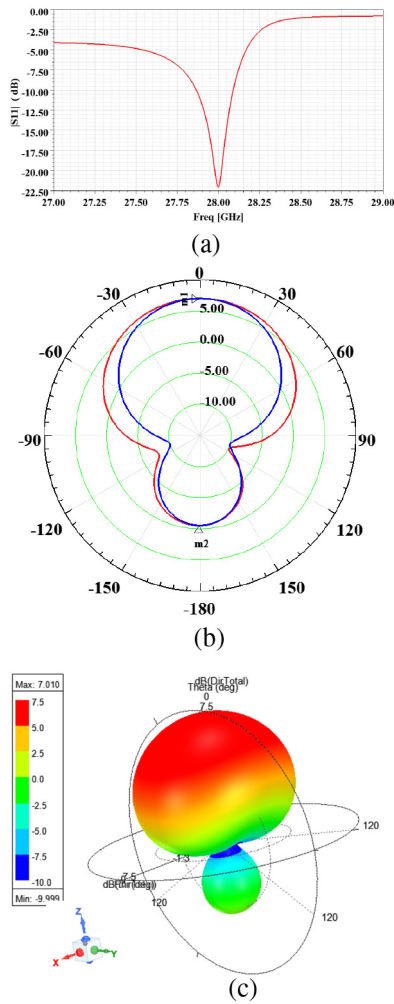
FIGURE 26. Simulated performance characteristics of the two-substrate layer 28 GHz quadrupole antenna. (a) $|S_{11}|$ values as a function of the source frequency. (b) 2D directivity patterns at 28 GHz in the two principle vertical planes. Red: $\phi = 0°$, blue: $\phi = 90°$. (c) 3D directivity pattern at 28 GHz.

FIGURE 27. Simulated performance characteristics of the three-substrate layer, ground plane backed, 28 GHz quadrupole antenna. (a) $|S_{11}|$ values as a function of the source frequency. (b) 2D directivity patterns at 28 GHz in the two principle vertical planes. Red: $\phi = 0°$, blue: : $\phi = 90°$. (c) 3D directivity pattern at 28 GHz.

some radiated field cancellation to occur. While the maximum directivity, 7.24 dB, occurs at 28.3 GHz, the overall (radiation) efficiency is yet even smaller: 2.8% (40.3%).

Note again that the 2D pattern in the $\phi = 0°$ plane is broader than the $\phi = 90°$ one because the antenna is narrower (longer) along the x-axis (y-axis). Moreover, its beamwidth is substantially broader than the stand-alone quadrupole case; it accounts for the lower peak directivity value and the significantly larger FTBR. The 3D directivity pattern is presented in Fig. 26(c). Its Huygens cardioid shape is immediately identified.

In spite of the fact that the impedance match deteriorated some when the bottom Rohacell layer and ground plane were integrated with the basic quadrupole antenna, the radiated field performance of the three-layer quadrupole design with the ground plane is quite appealing. As one would expect, optimization to attain the best impedance match, maximum directivity, and FTBR values simultaneously when taking into consideration all of the practical material and feed
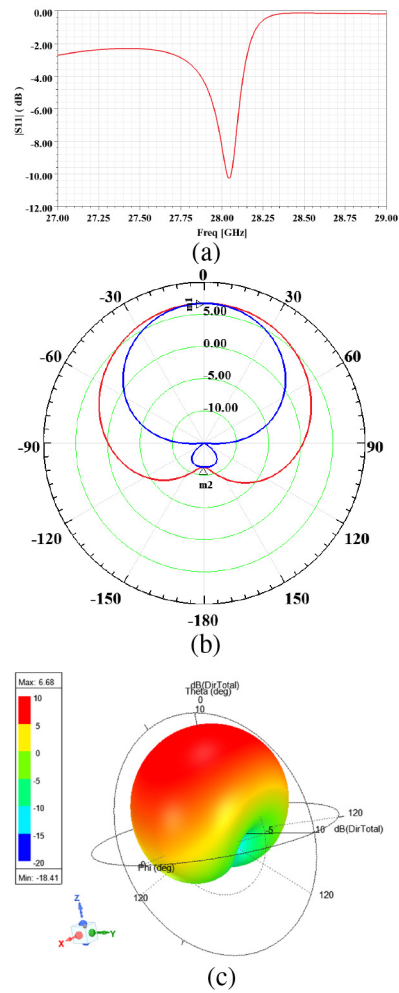
issues would be required to obtain the best performance for any prototype design. This very simple, unidirectional, high directivity HOM design may be of interest as well at even higher 5G frequencies. As demonstrated in [233], the basic quadrupolar design can be scaled readily to other frequency bands.

E. CAUTIONARY REALISTIC ISSUES

One major aspect of multipoles not yet critiqued is the issue of bandwidth. As was demonstrated when early meta-structures were being analyzed [55], [56], [146], the natural bandwidth of the N-th multipole decreases substantially as N increases. The same issue arises with HOMs in dielectric-based resonators. On the other hand, the measured bandwidth of the dipole-excited holey dielectric sphere appears to have been quite reasonable [260] as is that of the quadrupole antenna [233]. While there are many narrowband EM applications, e.g., battery-free wirelessly power sensor networks [221], communication systems generally desire

as much bandwidth as possible. Because reasonable bandwidths have been obtained for active unidirectional systems based on electric and magnetic dipoles, i.e., non-Foster circuit augmented HDAs [209], [266], [267], it is anticipated that active multipole radiators will overcome their potential narrow bandwidth stigma.

Another major issue, usually highlighted in any discussion of superdirective systems in addition to bandwidth, is the overall efficiency. The difference approach to creating multipoles when the distance between the various dipole elements is negligibly small leads to poor overall efficiencies. This outcome is caused by the need for opposite oriented currents on the juxtaposed elements. While the PEC-based 3-wire quadrupole system has a overall (radiation) efficiency of 100% (100%) in all cases as it should, those cases were re-simulated with copper wires and an impedance matched lumped source. The overall (radiation) efficiency of the 3-wire Huygens case at 0.9825 MHz only dropped to 75.0% (97.2%), which is still quite reasonable, i.e., it clearly did not become negligible. Similarly, the overall (radiation) efficiency of the quadrupole version at 1.0453 GHz and the quasi-Huygens at 1.0075 GHz became 48.9% (64.3%) and 39.0% (95.3%), respectively. The overall efficiency of the quasi-Huygens case suffered the most as a consequence of the current distributions on the now lossy wires. On the other hand, both the reference and ground-plane quadrupole 28 GHz designs had very acceptable overall and radiation efficiencies.

Despite the commonly considered drawbacks, there are clearly unique opportunities for HOMs and their potentially narrow bandwidths. EM system applications have a much wider breadth than just wireless communications. Recall that a narrow bandwidth corresponds to a high quality factor Q. High-Q structures are advantageous for filter and absorber designs. A very recent example that uses core-shell multipoles and their high-Q properties to achieve pass-band filters [84] and another that presents an all-dielectric perfect absorber [85] illustrate this point. A much older example is the use of cylindrical and spherical high-Q cavities as energy storage devices for microwave compression applications associated, for instance, with particle accelerators [268]–[270].

VII. CONCLUSION

A review of multipoles and the recent resurgence of interest in them for EM radiating and scattering systems was presented. In particular, their advantages to obtain enhanced, unidirectional performance were identified and emphasized. Even though multipolar analyses of canonical versions of those systems are a foundational aspect of advanced electromagnetics in academia and analytical solutions of them were the mainstay in modeling and understanding practical applications in the last century, CEM simulations rapidly displaced them. CEM parameter studies have become the normal approach to complex problems with generally little

thought to analysis. While the physics and optics communities have rediscovered multipoles as tools for modeling a variety of metamaterials and Mie-tronic structures, the current engineering electromagnetic community has yet to embrace their utility for advanced antenna concepts for a number of reasons. Nevertheless, several examples were presented that suggest mixtures of multipoles may, in fact, have useful practical benefits.

Quadrupole and other higher-order multipoles (HOMs) were described; superdirective systems enabled with them were demonstrated. The optimized five-layer 2D cylinder system illustrated the ability to use a set of HOMs to approach the theoretical 2D directivity bound. Edge-singularities associated with localized BIC examples illustrated another approach to generating and utilizing a mixture of multipoles to attain higher directivities. A 3-wire system demonstrated Huygens quadrupolar-based results. A low-profile quadrupolar antenna with and without a ground plane present illustrated how one can take advantage of multipole image currents in the ground plane. Single port multipolar antennas were introduced. Advantages and drawbacks of these and other HOM-based concepts were discussed.

While systems depending on higher order mode resonances in high dielectric constant material-based structures have been considered over the years, there has been little vigorous interest because of the associated very high losses and realization difficulties in addition to their very narrow bandwidths. However, material technologies have dramatically improved in the last decade and very low loss, high dielectric constant materials are now available. Moreover, manufacturing processes have likewise improved that facilitate their integration with rather complex metallic and dielectric structures. Opportunities abound for multipolar concepts. The many referenced nanotechnology-based systems clearly illustrate this. It may indeed be an appropriate juncture for engineering electromagnetics practitioners to revisit multipolar concepts for future EM-based systems requiring, for example, enhanced directivity performance or very high-Q properties and, thus, to have mixtures-of-multipoles as an asset in their EM toolboxes.

REFERENCES

[1] T. S. Rappaport *et al.*, "Millimeter wave mobile communications for 5G cellular: It will work!" *IEEE Access*, vol. 1, pp. 335–349, 2013.

[2] M. Shafi *et al.*, "5G: A tutorial overview of standards, trials, challenges, deployment, and practice," *IEEE J. Sel. Areas Commun.*, vol. 35, no. 6, pp. 1201–1221, Jun. 2017.

[3] W. Hong *et al.*, "Multibeam antenna technologies for 5G wireless communications," *IEEE Trans. Antennas Propag.*, vol. 65, no. 12, pp. 6231–6249, Dec. 2017.

[4] Z. Zhang *et al.*, "6G wireless networks: Vision, requirements, architecture, and key technologies," *IEEE Veh. Technol. Mag.*, vol. 14, no. 3, pp. 28–41, Sep. 2019.

[5] H. Tataria, M. Shafi, A. F. Molisch, M. Dohler, H. Sjöland, and F. Tufvesson, "6G wireless systems: Vision, requirements, challenges, insights, and opportunities," *Proc. IEEE*, vol. 109, no. 7, pp. 1166–1199, Jul. 2021.

[6] Y. J. Guo and R. W. Ziolkowski, *Advanced Antenna Array Engineering for 6G and Beyond Wireless Communications*, 1st ed. Hoboken, NJ, USA: Wiley, 2021.

[7] Y. J. Guo and R. W. Ziolkowski, *Antenna and Array Technologies for Future Wireless Ecosystems*, 1st ed. Hoboken, NJ, USA: Wiley, 2022.

[8] J. D. Krauss, *Antennas*, 2nd ed. New York, NY, USA: McGraw–Hill, 1988.

[9] C. A. Balanis, *Antenna Theory: Analysis and Design*, 4th ed. Hoboken, NJ, USA: Wiley, 2016.

[10] R. F. Harrington, "On the gain and beamwidth of directional antennas," *IRE Trans. Antennas Propag.*, vol. 6, no. 3, pp. 219–225, 1958.

[11] R. F. Harrington, "Effect of antenna size on gain, bandwidth, and efficiency," *J. Res. Nat. Bureau Stand.*, vol. 64, no. 1, pp. 1–12, Jan./Feb. 1960.

[12] C. Bouwkamp and H. Casimir, "On multipole expansions in the theory of electromagnetic radiation," *Physica*, vol. 20, nos. 1–6, pp. 539–554, 1954.

[13] J. D. Jackson, *Classical Electrodynamics*. Hoboken, NJ, USA: Wiley, 1962.

[14] A. J. Devaney and E. Wolf, "Multipole expansions and plane wave representations of the electromagnetic field," *J. Math. Phys.*, vol. 15, no. 2, pp. 234–244, 1974.

[15] M. Pigeon, A. Clemente, C. Delaveaud, and L. Rudant, "Analysis of Harrington limit for electrically small antenna directivity," in *Proc. 8th Eur. Conf. Antennas Propag. (EuCAP)*, The Hague, The Netherlands, Apr. 2014, pp. 2921–2925.

[16] A. D. Yaghjian, "Sampling criteria for resonant antennas and scatterers," *J. Appl. Phys.*, vol. 79, no. 10, pp. 7474–7482, 1996.

[17] C. F. Bohren, "How can a particle absorb more than the light incident on it?" *Amer. J. Phys.*, vol. 51, no. 4, pp. 323–327, 1983.

[18] H. Paul and R. Fischer, "Light absorption by a dipole," *Soviet Phys. Uspekhi*, vol. 26, no. 10, pp. 923–926, 1983.

[19] W. Lin, R. W. Ziolkowski, and J. Huang, "Electrically small, low profile, highly efficient, Huygens dipole rectennas for wirelessly powering Internet-of-Things (IoT) devices," *IEEE Trans. Antennas Propag.*, vol. 67, no. 6, pp. 3670–3679, Jun. 2019.

[20] L. J. Chu, "Physical limitations of omni-directional antennas," *J. Appl. Phys.*, vol. 19, no. 12, pp. 1163–1175, Dec. 1948.

[21] J. S. McLean, "A re-examination of the fundamental limits on the radiation Q of electrically small antennas," *IEEE Trans. Antennas Propag.*, vol. 44, no. 5, pp. 672–676, May 1996.

[22] S. R. Best, "Low Q electrically small linear and elliptical polarized spherical dipole antennas," *IEEE Trans. Antennas Propag.*, vol. 53, no. 3, pp. 1047–1053, Mar. 2005.

[23] A. D. Yaghjian and S. R. Best, "Impedance, bandwidth, and Q of antennas," *IEEE Trans. Antennas Propag.*, vol. 53, no. 4, pp. 1298–1324, Apr. 2005.

[24] P.-S. Kildal, "Fundamental directivity and efficiency limitations of single- and multi-port antennas," in *Proc. 2nd Eur. Conf. Antennas Propag.*, Nov. 2007, pp. 16–25.

[25] P.-S. Kildal and S. R. Best, "Further investigations of fundamental directivity limitations of small antennas with and without ground planes," in *Proc. IEEE Antennas Propag. Soc. Int. Symp.*, San Diego, CA, USA, Jul. 2008, pp. 1–4.

[26] P.-S. Kildal, E. Martini, and S. Maci, "Degrees of freedom and maximum directivity of antennas: A bound on maximum directivity of nonsuperreactive antennas," *IEEE Antennas Propag. Mag.*, vol. 59, no. 4, pp. 16–25, Aug. 2017.

[27] R. F. Harrington, *Time-Harmonic Electromagnetic Fields*. New York, NY, USA: McGraw–Hill, 1961.

[28] E. J. J. Bowman, T. B. A. Senior, and P. L. E. Uslenghi, *Electromagnetic and Acoustic Scattering by Simple Shapes*. Amsterdam, The Netherlands: North-Holland Publ. Company, 1969.

[29] W. C. Chew, *Waves and Fields in Inhomogeneous Media*. New York, NY, USA: Van Nostrand Reinhold, 1990.

[30] C. A. Balanis, *Advanced Engineering Electromagnetics*, 2nd ed. Hoboken, NJ, USA: Wiley, 2012.

[31] S. J. Orfanidis, *Electromagnetic Waves and Antennas*. Piscataway, NJ, USA: Rutgers Univ., 2014.

[32] D. E. Barrick, W. D. Stuart, and C. K. Krichbaum, *Radar Cross Section Handbook: Volumes 1 & 2*, G. T. Ruck, Ed. New York, NY, USA: Plenum Press, 1970.

[33] R. W. Ziolkowski, "New electromagnetic resonance effects associated with cavity-backed apertures," *Radio Sci.*, vol. 22, no. 4, pp. 449–454, Jul./Aug. 1987.

[34] A. Yaghjian and R. Wittmann, "The receiving antenna as a linear differential operator: Application to spherical near-field scanning," *IEEE Trans. Antennas Propag.*, vol. AP-33, no. 11, pp. 1175–1185, Nov. 1985.

[35] A. D. Yaghjian, "Three-dimensional planar surface-current equivalence theorem with application to receiving antennas as linear differential operators," *Radio Sci.*, vol. 37, no. 2, pp. 1–10, 2002.

[36] T. Hansen, "Formulation of spherical near-field scanning for electromagnetic fields in the time domain," *IEEE Trans. Antennas Propag.*, vol. 45, no. 4, pp. 620–630, Apr. 1997.

[37] W. A. Johnson and R. W. Ziolkowski, "The scattering of an H-polarized plane wave from an axially slotted infinite cylinder: A dual series approach," *Radio Sci.*, vol. 19, no. 1, pp. 275–291, Jan./Feb. 1984.

[38] R. W. Ziolkowski, W. A. Johnson, and K. F. Casey, "Applications of Riemann-Hilbert problem techniques to electromagnetic coupling through apertures," *Radio Sci.*, vol. 19, no. 6, pp. 1425–1431, Nov./Dec. 1984.

[39] R. Ziolkowski and J. Grant, "Scattering from cavity-backed apertures: The generalized dual series solution of the concentrically loaded E-pol slit cylinder problem," *IEEE Trans. Antennas Propag.*, vol. 35, no. 5, pp. 504–528, May 1987.

[40] R. W. Ziolkowski and W. A. Johnson, "Electromagnetic scattering of an arbitrary plane wave from a spherical shell with a circular aperture," *J. Math. Phys.*, vol. 28, no. 6, pp. 1293–1314, 1987.

[41] R. W. Ziolkowski, D. P. Marsland, L. F. Libelo, and G. E. Pisane, "Scattering from an open spherical shell having a circular aperture and enclosing a concentric dielectric sphere," *IEEE Trans. Antennas Propag.*, vol. 36, no. 7, pp. 985–999, Jul. 1988.

[42] R. E. Raab and O. L. De Lange, *Multipole Theory in Electromagnetism: Classical, Quantum, and Symmetry Aspects, With Applications*. Oxford, U.K.: Clarendon Press, 2005.

[43] E. Heyman and A. Devaney, "Time-dependent multipoles and their application for radiation from volume source distributions," *J. Math. Phys.*, vol. 37, no. 2, pp. 682–692, 1996.

[44] A. Shlivinski and E. Heyman, "Time-domain near-field analysis of short-pulse antennas—Part I. Spherical wave (multipole) expansion," *IEEE Trans. Antennas Propag.*, vol. 47, no. 2, pp. 271–279, Feb. 1999.

[45] A. Moroz. "Scattering from a Multilayered Sphere." Aug. 2021. [Online]. Available: http://www.wave-scattering.com/codes.html

[46] T. Hinamoto and M. Fujii. "Multipole Expansion for Nanophotonics (MENP)." Aug. 18, 2021. [Online]. Available: https://github.com/Hinamooon/MENP

[47] N. Engheta and R. W. Ziolkowski, *Metamaterials: Physics and Engineering Explorations*. Hoboken, NJ, USA: Wiley, 2006.

[48] C. L. Holloway, E. F. Kuester, J. A. Gordon, J. O'Hara, J. Booth, and D. R. Smith, "An overview of the theory and applications of metasurfaces: The two-dimensional equivalents of metamaterials," *IEEE Antennas Propag. Mag.*, vol. 54, no. 2, pp. 10–35, Apr. 2012.

[49] R. W. Ziolkowski and F. Auzanneau, "Passive artificial molecule realizations of dielectric materials," *J. Appl. Phys.*, vol. 82, no. 7, pp. 3195–3198, 1997.

[50] R. W. Ziolkowski and F. Auzanneau, "Artificial molecule realization of a magnetic wall," *J. Appl. Phys.*, vol. 82, no. 7, pp. 3192–3194, 1997.

[51] F. Auzanneau and R. W. Ziolkowski, "Theoretical study of synthetic bianisotropic materials," *J. Electromagn. Waves Appl.*, vol. 12, no. 3, pp. 353–370, 1998.

[52] F. Auzanneau and R. W. Ziolkowski, "Microwave signal rectification using artificial composite materials composed of diode-loaded electrically small dipole antennas," *IEEE Trans. Microw. Theory Techn.*, vol. 46, no. 11, pp. 1628–1637, Nov. 1998.

[53] R. W. Ziolkowski and A. D. Kipple, "Reciprocity between the effects of resonant scattering and enhanced radiated power by electrically small antennas in the presence of nested metamaterial shells," *Phys. Rev. E, Stat. Phys. Plasmas Fluids Relat. Interdiscip. Top.*, vol. 72, no. 3, 2005, Art. no. 036602.

[54] A. Alù and N. Engheta, "Polarizabilities and effective parameters for collections of spherical nanoparticles formed by pairs of concentric double-negative, single-negative, and/or double-positive metamaterial layers," *J. Appl. Phys.*, vol. 97, no. 9, 2005, Art. no. 094310.

[55] S. Arslanagić, R. W. Ziolkowski, and O. Breinbjerg, "Analytical and numerical investigation of the radiation and scattering from concentric metamaterial cylinders excited by an electric line source," *Radio Sci.*, vol. 42, no. 6, pp. 1–22, Dec. 2007.

[56] S. Arslanagić, R. W. Ziolkowski, and O. Breinbjerg, "Analytical and numerical investigation of the radiation from concentric metamaterial spheres excited by an electric Hertzian dipole," *Radio Sci.*, vol. 42, no. 6, Dec. 2007, Art. no. RS6S16.

[57] R. W. Ziolkowski and A. D. Kipple, "Application of double negative materials to increase the power radiated by electrically small antennas," *IEEE Trans. Antennas Propag.*, vol. 51, no. 10, pp. 2626–2640, Oct. 2003.

[58] Z. Ruan and S. Fan, "Superscattering of light from subwavelength nanostructures," *Phys. Rev. Lett.*, vol. 105, no. 1, Jul. 2010, Art. no. 013901.

[59] Z. Ruan and S. Fan, "Design of subwavelength superscattering nanospheres," *Appl. Phys. Lett.*, vol. 98, no. 4, Jan. 2011, Art. no. 043101.

[60] A. Mirzaei, A. E. Miroshnichenko, I. V. Shadrivov, and Y. S. Kivshar, "Superscattering of light optimized by a genetic algorithm," *Appl. Phys. Lett.*, vol. 105, no. 1, 2014, Art. no. 011109.

[61] A. Alù and N. Engheta, "Achieving transparency with plasmonic and metamaterial coatings," *Phys. Rev. E, Stat. Phys. Plasmas Fluids Relat. Interdiscip. Top.*, vol. 72, no. 1, 2005, Art. no. 16623.

[62] S. Mühlig, C. Menzel, C. Rockstuhl, and F. Lederer, "Multipole analysis of meta-atoms," *Metamaterials*, vol. 5, nos. 2–3, pp. 64–73, 2011.

[63] P. Grahn, A. Shevchenko, and M. Kaivola, "Electromagnetic multipole theory for optical nanomaterials," *New J. Phys.*, vol. 14, no. 9, Sep. 2012, Art. no. 93033.

[64] P. C. Waterman, "Symmetry, unitarity, and geometry in electromagnetic scattering," *Phys. Rev. D*, vol. 3, no. 4, pp. 825–839, Aug. 1971.

[65] J. Petschulat *et al.*, "Understanding the electric and magnetic response of isolated metaatoms by means of a multipolar field decomposition," *Opt. Exp.*, vol. 18, no. 14, pp. 14454–14466, Jul. 2010.

[66] R. Guo *et al.*, "Multipolar coupling in hybrid metal–dielectric metasurfaces," *ACS Photon.*, vol. 3, no. 3, pp. 349–353, 2016.

[67] R. Dezert, P. Richetti, and A. Baron, "Complete multipolar description of reflection and transmission across a metasurface for perfect absorption of light," *Opt. Exp.*, vol. 27, no. 19, pp. 26317–26330, Sep. 2019.

[68] M. Decker *et al.*, "High-efficiency dielectric Huygens' surfaces," *Adv. Opt. Mater.*, vol. 3, no. 6, pp. 813–820, 2015.

[69] J. B. Pendry, "Negative refraction makes a perfect lens," *Phys. Rev. Lett.*, vol. 85, no. 18, pp. 3966–3969, 2000.

[70] V. M. Shalaev, "Optical negative-index metamaterials," *Nat. Photon.*, vol. 1, no. 1, pp. 41–48, 2007.

[71] T. A. Klar, A. V. Kildishev, V. P. Drachev, and V. M. Shalaev, "Negative-index metamaterials: Going optical," *IEEE J. Sel. Topics Quantum Electron.*, vol. 12, no. 6, pp. 1106–1115, Nov./Dec. 2006.

[72] W. Liu and Y. S. Kivshar, "Multipolar interference effects in nanophotonics," *Philos. Trans. Royal Soc. A*, vol. 375, no. 2090, Mar. 2017, Art. no. 20160317.

[73] R. Alaee, C. Rockstuhl, and I. Fernandez-Corbaton, "Exact multipolar decompositions with applications in nanophotonics," *Adv. Opt. Mat.*, vol. 7, no. 1, 2019, Art. no. 1800783.

[74] C. L. Holloway, E. F. Kuester, J. Baker-Jarvis, and P. Kabos, "A double negative (DNG) composite medium composed of magnetodielectric spherical particles embedded in a matrix," *IEEE Trans. Antennas Propag.*, vol. 51, no. 10, pp. 2596–2603, Oct. 2003.

[75] M. S. Wheeler, J. S. Aitchison, and M. Mojahedi, "Three-dimensional array of dielectric spheres with an isotropic negative permeability at infrared frequencies," *Phys. Rev. B, Condens. Matter*, vol. 72, no. 19, 2005, Art. no. 193103.

[76] V. Yannopapas and A. Moroz, "Negative refractive index metamaterials from inherently non-magnetic materials for deep infrared to terahertz frequency ranges," *J. Condens. Matter Phys.*, vol. 17, no. 25, pp. 3717–3734, 2005.

[77] A. Ahmadi and H. Mosallaei, "Physical configuration and performance modeling of all-dielectric metamaterials," *Phys. Rev. B*, vol. 77, no. 4, 2008, Art. no. 045104.

[78] Q. Zhao, J. Zhou, F. Zhang, and D. Lippens, "Mie resonance-based dielectric metamaterials," *Mat. Today*, vol. 12, no. 12, pp. 60–69, 2009.

[79] S. Ghadarghadr and H. Mosallaei, "Coupled dielectric nanoparticles manipulating metamaterials optical characteristics," *IEEE Trans. Nanotechnol.*, vol. 8, no. 5, pp. 582–594, Sep. 2009.

[80] J.-M. Geffrin *et al.*, "Magnetic and electric coherence in forward- and back-scattered electromagnetic waves by a single dielectric subwavelength sphere," *Nat. Commun.*, vol. 3, no. 1, pp. 1–8, 2012.

[81] J. Cheng, D. Ansari-Oghol-Beig, and H. Mosallaei, "Wave manipulation with designer dielectric metasurfaces," *Opt. Lett.*, vol. 39, no. 21, pp. 6285–6288, 2014.

[82] M. Decker and I. Staude, "Resonant dielectric nanostructures: A low-loss platform for functional nanophotonics," *J. Opt.*, vol. 18, no. 10, 2016, Art. no. 103001.

[83] J. A. Gordon and R. W. Ziolkowski, "Colors generated by tunable plasmon resonances and their potential application to ambiently illuminated color displays," *Solide State Commun.*, vol. 146, nos. 5–6, pp. 228–238, 2008.

[84] A. Monti, A. Alú, A. Toscano, and F. Bilotti, "Design of high-Q passband filters implemented through multipolar all-dielectric metasurfaces," *IEEE Trans. Antennas Propag.*, vol. 69, no. 8, pp. 5142–5147, Aug. 2021.

[85] R. Xu and J. Takahara, "All-dielectric perfect absorber based on quadrupole modes," *Opt. Lett.*, vol. 46, no. 15, pp. 3596–3599, Aug. 2021.

[86] J. A. Gordon and R. W. Ziolkowski, "The design and simulated performance of a coated nano-particle laser," *Opt. Exp.*, vol. 15, no. 5, pp. 2622–2653, Mar. 2007.

[87] A. K. Sarychev and G. Tartakovsky, "Magnetic plasmonic metamaterials in actively pumped host medium and plasmonic nanolaser," *Phys. Rev. B, Condens. Matter*, vol. 75, no. 8, 2007, Art. no. 85436.

[88] Y. Sivakn, S. Xiao, U. K. Chettiar, A. V. Kildishev, and V. M. Shalaev, "Frequency-domain simulations of a negative-index material with embedded gain," *Opt. Exp.*, vol. 17, no. 26, pp. 24060–24074, Dec. 2009.

[89] A. Fang, T. Koschny, M. Wegener, and C. Soukoulis, "Self-consistent calculation of metamaterials with gain," *Phys. Rev. B, Condens. Matter*, vol. 79, no. 24, 2009, Art. no. 241104.

[90] S. Xiao *et al.*, "Loss-free and active optical negative-index metamaterials," *Nature*, vol. 466, no. 7307, pp. 735–738, 2010.

[91] J. Geng, R. W. Ziolkowski, R. Jin, and X. Liang, "Numerical study of the near-field and far-field properties of active open cylindrical coated nanoparticle antennas," *IEEE Photon. J.*, vol. 3, no. 6, pp. 1093–1110, Dec. 2011.

[92] J. Geng, R. W. Ziolkowski, R. Jin, and X. Liang, "Detailed performance characteristics of vertically polarized, cylindrical, active coated nano-particle antennas," *Radio Sci.*, vol. 47, no. 2, pp. 1–21, Apr. 2012.

[93] J. A. Gordon and R. W. Ziolkowski, "Investigating functionalized active coated nanoparticles for use in nano-sensing applications," *Opt. Exp.*, vol. 15, no. 20, pp. 12562–12582, Oct. 2007.

[94] S. Arslanagić and R. W. Ziolkowski, "Active coated nanoparticle excited by an arbitrarily located electric Hertzian dipole-resonance and transparency effects," *J. Opt.*, vol. 12, no. 2, 2010, Art. no. 024014.

[95] S. D. Campbell and R. W. Ziolkowski, "Impact of strong localization of the incident power density on the nano-amplifier characteristics of active coated nano-particles," *Opt. Commun.*, vol. 285, no. 16, pp. 3341–3352, 2012.

[96] S. D. Campbell and R. W. Ziolkowski, "The performance of active coated nanoparticles based on quantum-dot gain media," *Adv. OptoElectron.*, vol. 2012, Sep. 2012, Art. no. 368786, doi: 10.1155/2012/368786.

[97] S. Arslanagić and R. Ziolkowski, "Influence of active nano particle size and material composition on multiple quantum emitter enhancements: Their enhancement and jamming effects," *Progr. Electromagn. Res.*, vol. 149, pp. 85–99, Sep. 2014.

[98] R. Thorsen and S. Arslanagić, "Higher order mode excitation in eccentric active nano-particles for tailoring of the near-field radiation," in *Proc. 9th Int. Congr. Adv. Electromagn. Mater. Microw. Opt. (METAMATERIALS)*, 2015, pp. 307–309.

[99] S. Arslanagić and R. W. Ziolkowski, "Cylindrical and spherical active coated nanoparticles as nanoantennas: Active nanoparticles as nanoantennas," *IEEE Antennas Propag. Mag.*, vol. 59, no. 6, pp. 14–29, Dec. 2017.

[100] S. Arslanagić and R. E. Jacobsen, "Active coated nano rod antennas for enhanced and directive scattering phenomena," *EPJ Appl. Metamater.*, vol. 6, p. 19, Oct. 2019.

[101] R. Ø. Thorsen and S. Arslanagić, "Eccentrically-layered active coated nano-particles for directive near-and far-field radiation," *Photonics*, vol. 2, no. 3, pp. 773–794, 2015.

[102] S. Arslanagić and R. W. Ziolkowski, *Passive and Active Nano Cylinders for Enhanced and Directive Radiation and Scattering Phenomena*. London, U.K.: Inst. Eng. Technol., 2020, ch. 2, pp. 53–102.

[103] J. A. Gordon and R. W. Ziolkowski, "CNP optical metamaterials," *Opt. Exp.*, vol. 16, no. 9, pp. 6692–6716, Apr. 2008.

[104] A. G. Curto, T. H. Taminiau, G. Volpe, M. P. Kreuzer, R. Quidant, and N. F. Van Hulst, "Multipolar radiation of quantum emitters with nanowire optical antennas," *Nat. Commun.*, vol. 4, no. 1, pp. 1–7, 2013.

[105] D. Smirnova and Y. S. Kivshar, "Multipolar nonlinear nanophotonics," *Optica*, vol. 3, no. 11, pp. 1241–1255, Nov. 2016.

[106] B. Sain, C. Meier, and T. Zentgraf, "Nonlinear optics in all-dielectric nanoantennas and metasurfaces: A review," *Adv. Photon.*, vol. 1, no. 2, 2019, Art. no. 24002.

[107] K. Koshelev and Y. Kivshar, "Dielectric resonant metaphotonics," *ACS Photon.*, vol. 8, no. 1, pp. 102–112, 2020.

[108] A. I. Kuznetsov, A. E. Miroshnichenko, Y. H. Fu, J. Zhang, and B. Luk-Yanchuk, "Magnetic light," *Sci. Rep.*, vol. 2, no. 1, pp. 1–6, 2012.

[109] I. Staude et al., "Tailoring directional scattering through magnetic and electric resonances in subwavelength silicon nanodisks," *ACS Nano*, vol. 7, no. 9, pp. 7824–7832, 2013.

[110] A. I. Kuznetsov, A. E. Miroshnichenko, M. L. Brongersma, Y. S. Kivshar, and B. Luk-Yanchuk, "Optically resonant dielectric nanostructures," *Science*, vol. 354, no. 6314, 2016, Art. no. aag2472.

[111] S. Kruk and Y. Kivshar, "Functional meta-optics and nanophotonics governed by Mie resonances," *ACS Photon.*, vol. 4, no. 11, pp. 2638–2649, 2017.

[112] W. Chen, Q. Yang, Y. Chen, and W. Liu, "Global Mie scattering: Polarization morphologies and the underlying topological invariant," *ACS Omega*, vol. 5, no. 23, pp. 14157–14163, 2020.

[113] V. E. Babicheva and A. B. Evlyukhin, "Multipole lattice effects in high refractive index metasurfaces," *J. Appl. Phys.*, vol. 129, no. 4, 2021, Art. no. 040902.

[114] R. Won, "Into the 'Mie-tronic' era," *Nat. Photon.*, vol. 13, pp. 585–587, Aug. 2019.

[115] H. Caglayan, S.-H. Hong, B. Edwards, C. R. Kagan, and N. Engheta, "Near-infrared metatronic nanocircuits by design," *Phys. Rev. Lett.*, vol. 111, no. 7, 2013, Art. no. 073904.

[116] Y. Li, I. Liberal, C. D. Giovampaola, and N. Engheta, "Waveguide metatronics: Lumped circuitry based on structural dispersion," *Sci. Adv.*, vol. 2, no. 6, 2016, Art. no. e1501790.

[117] T. Kaelberer, V. Fedotov, N. Papasimakis, D. Tsai, and N. Zheludev, "Toroidal dipolar response in a metamaterial," *Science*, vol. 330, no. 6010, pp. 1510–1512, 2010.

[118] V. A. Fedotov, A. Rogacheva, V. Savinov, D. P. Tsai, and N. I. Zheludev, "Resonant transparency and non-trivial non-radiating excitations in toroidal metamaterials," *Sci. Rep.*, vol. 3, no. 1, pp. 1–5, 2013.

[119] A. A. Basharin et al., "Dielectric metamaterials with toroidal dipolar response," *Phys. Rev. X*, vol. 5, no. 1, 2015, Art. no. 011036.

[120] N. Papasimakis, V. Fedotov, V. Savinov, T. Raybould, and N. Zheludev, "Electromagnetic toroidal excitations in matter and free space," *Nat. Mater.*, vol. 15, no. 3, pp. 263–271, 2016.

[121] V. Savinov, N. Papasimakis, D. Tsai, and N. Zheludev, "Optical anapoles," *Commun. Phys.*, vol. 2, no. 1, pp. 1–4, 2019.

[122] I. Fernandez-Corbaton, S. Nanz, and C. Rockstuhl, "On the dynamic toroidal multipoles from localized electric current distributions," *Sci. Rep.*, vol. 7, no. 1, pp. 1–8, Aug. 2017.

[123] J. Mun, S. So, J. Jang, and J. Rho, "Describing meta-atoms using the exact higher-order polarizability tensors," *ACS Photon.*, vol. 7, no. 5, pp. 1153–1162, 2020.

[124] C. Liu et al., "Characteristics of electric quadrupole and magnetic quadrupole coupling in a symmetric silicon structure," *New J. Phys.*, vol. 22, no. 2, 2020, Art. no. 023018.

[125] S. Raza, "Slow light using magnetic and electric Mie resonances," *Opt. Lett.*, vol. 45, no. 5, pp. 1260–1263, 2020.

[126] N. Bonod, "Controlling spontaneous emission with dielectric optical antennas," in *Dielectric Metamaterials*. Cambridge, U.K.: Elsevier, 2020, pp. 109–144.

[127] I. M. Hancu, A. G. Curto, M. Castro-López, M. Kuttge, and N. F. van Hulst, "Multipolar interference for directed light emission," *Nano Lett.*, vol. 14, no. 1, pp. 166–171, 2014.

[128] V. E. Babicheva and A. B. Evlyukhin, "Interplay and coupling of electric and magnetic multipole resonances in plasmonic nanoparticle lattices," *MRS Commun.*, vol. 8, no. 3, pp. 712–717, 2018.

[129] V. E. Babicheva and A. B. Evlyukhin, "Analytical model of resonant electromagnetic dipole-quadrupole coupling in nanoparticle arrays," *Phys. Rev. B, Condens. Matter*, vol. 99, no. 19, 2019, Art. no. 195444.

[130] C. Liu et al., "Beyond dipole excitation: The performance of quadrupole-based Huygens' metasurface," *Opt. Lett.*, vol. 45, no. 17, pp. 4847–4850, 2020.

[131] E. Jones, "Paraboloid reflector and hyperboloid lens antennas," *Trans. IRE Antennas Propag.*, vol. 2, no. 3, pp. 119–127, Jul. 1954.

[132] A. W. Love, "Some highlights in reflector antenna development," *Radio Sci.*, vol. 11, nos. 8–9, pp. 671–684, Aug./Sep. 1976.

[133] M. Kerker, D.-S. Wang, and C. Giles, "Electromagnetic scattering by magnetic spheres," *J. Opt. Soc. America*, vol. 73, no. 6, pp. 765–767, 1983.

[134] A. Alù and N. Engheta, "How does zero forward-scattering in magnetodielectric nanoparticles comply with the optical theorem?" *J. Nanophoton.*, vol. 4, no. 1, 2010, Art. no. 041590.

[135] I. Liberal, I. Ederra, R. Gonzalo, and R. W. Ziolkowski, "Superbackscattering from single dielectric particles," *J. Opt.*, vol. 17, no. 7, 2015, Art. no. 072001.

[136] I. Liberal, I. Ederra, R. Gonzalo, and R. W. Ziolkowski, "A multipolar analysis of near-field absorption and scattering processes," *IEEE Trans. Antennas Propag.*, vol. 61, no. 10, pp. 5184–5199, Oct. 2013.

[137] R. Alaee, R. Filter, D. Lehr, F. Lederer, and C. Rockstuhl, "A generalized Kerker condition for highly directive nanoantennas," *Opt. Lett.*, vol. 40, no. 11, pp. 2645–2648, 2015.

[138] A. Pors, S. K. Andersen, and S. I. Bozhevolnyi, "Unidirectional scattering by nanoparticles near substrates: Generalized Kerker conditions," *Opt. Exp.*, vol. 23, no. 22, pp. 28808–28828, 2015.

[139] X. M. Zhang, Q. Zhang, S. J. Zeng, Z. Z. Liu, and J.-J. Xiao, "Dual-band unidirectional forward scattering with all-dielectric hollow nanodisk in the visible," *Opt. Lett.*, vol. 43, no. 6, pp. 1275–1278, 2018.

[140] W. Liu and Y. S. Kivshar, "Generalized Kerker effects in nanophotonics and meta-optics," *Opt. Exp.*, vol. 26, no. 10, pp. 13085–13105, 2018.

[141] H. K. Shamkhi et al., "Transverse scattering and generalized Kerker effects in all-dielectric Mie-resonant metaoptics," *Phys. Rev. Lett.*, vol. 122, no. 19, 2019, Art. no. 193905.

[142] S. Campione, L. I. Basilio, L. K. Warne, and M. B. Sinclair, "Tailoring dielectric resonator geometries for directional scattering and Huygens' metasurfaces," *Opt. Exp.*, vol. 23, no. 3, pp. 2293–2307, 2015.

[143] J. Y. Lee, A. E. Miroshnichenko, and R.-K. Lee, "Simultaneously nearly zero forward and nearly zero backward scattering objects," *Opt. Exp.*, vol. 26, no. 23, pp. 30393–30399, 2018.

[144] K. Fan, I. V. Shadrivov, A. E. Miroshnichenko, and W. J. Padilla, "Infrared all-dielectric Kerker metasurfaces," *Opt. Exp.*, vol. 29, no. 7, pp. 10518–10526, 2021.

[145] S. Oldenburg, G. Hale, J. Jackson, and N. Halas, "Light scattering from dipole and quadrupole nanoshell antennas," *Appl. Phys. Lett.*, vol. 75, no. 8, pp. 1063–1065, 1999.

[146] A. Alù and N. Engheta, "Enhanced directivity from subwavelength infrared/optical nano-antennas loaded with plasmonic materials or metamaterials," *IEEE Trans. Antennas Propag.*, vol. 55, no. 11, pp. 3027–3039, Nov. 2007.

[147] S. Arslanagić and R. W. Ziolkowski, "Directive properties of active coated nano-particles," *Adv. Electromagn.*, vol. 1, no. 1, pp. 57–64, 2012.

[148] W. Liu, A. E. Miroshnichenko, D. N. Neshev, and Y. S. Kivshar, "Broadband unidirectional scattering by magneto-electric core-shell nanoparticles," *ACS Nano*, vol. 6, no. 6, pp. 5489–5497, 2012.

[149] S. D. Campbell and R. W. Ziolkowski, "Simultaneous excitation of electric and magnetic dipole modes in a resonant core-shell particle at infrared frequencies to achieve minimal backscattering," *IEEE J. Sel. Top. Quantum Electron.*, vol. 19, no. 3, May/Jun. 2013, Art. no. 4700209.

[150] S. Campbell and R. W. Ziolkowski, "Near–field directive beams from passive and active asymmetric optical nanoantennas," *IEEE J. Sel. Top. Quantum Electron.*, vol. 12, no. 4, Jul./Aug. 2015, Art. no. 4800112.

[151] E. Poutrina and A. Urbas, "Multipole analysis of unidirectional light scattering from plasmonic dimers," *J. Opt.*, vol. 16, no. 11, 2014, Art. no. 114005.

[152] W. Liu, J. Zhang, B. Lei, H. Ma, W. Xie, and H. Hu, "Ultra-directional forward scattering by individual core-shell nanoparticles," *Opt. Exp.*, vol. 22, no. 13, pp. 16178–16187, 2014.

[153] R. R. Naraghi, S. Sukhov, and A. Dogariu, "Directional control of scattering by all-dielectric core-shell spheres," *Opt. Lett.*, vol. 40, no. 4, pp. 585–588, 2015.

[154] E. Poutrina and A. Urbas, "Multipolar interference for non-reciprocal nonlinear generation," *Sci. Rep.*, vol. 6, Apr. 2016, Art. no. 25113.

[155] W. Liu, B. Lei, J. Shi, and H. Hu, "Unidirectional superscattering by multilayered cavities of effective radial anisotropy," *Sci. Rep.*, vol. 6, no. 1, pp. 1–9, 2016.

[156] I. Liberal, I. Ederra, R. Gonzalo, and R. W. Ziolkowski, "Induction theorem analysis of resonant nanoparticles: Design of a Huygens source nanoparticle laser," *Phys. Rev. Appl.*, vol. 1, no. 4, May 2014, Art. no. 044002.

[157] W. Liu, "Ultra-directional super-scattering of homogenous spherical particles with radial anisotropy," *Opt. Exp.*, vol. 23, no. 11, pp. 14734–14743, 2015.

[158] S. I. Azzam *et al.*, "Single and multi-mode directional lasing from arrays of dielectric nanoresonators," *Laser Photon. Rev.*, vol. 15, no. 3, 2021, Art. no. 2000411.

[159] J. Li, A. Salandrino, and N. Engheta, "Optical spectrometer at the nanoscale using optical Yagi–Uda nanoantennas," *Phys. Rev. B, Condens. Matter*, vol. 79, no. 19, 2009, Art. no. 195104.

[160] T. Kosako, Y. Kadoya, and H. F. Hofmann, "Directional control of light by a nano-optical Yagi–Uda antenna," *Nat. Photon.*, vol. 4, no. 5, pp. 312–315, 2010.

[161] J. Sun, E. Timurdogan, A. Yaacobi, E. S. Hosseini, and M. R. Watts, "Large-scale nanophotonic phased array," *Nature*, vol. 493, no. 7431, pp. 195–199, 2013.

[162] D. Dregely, K. Lindfors, M. Lippitz, N. Engheta, M. Totzeck, and H. Giessen, "Imaging and steering an optical wireless nanoantenna link," *Nat. Commun.*, vol. 5, p. 4354, Jul. 2014.

[163] I. Liberal, I. Ederra, R. Gonzalo, and R. W. Ziolkowski, "Superbackscattering nanoparticle dimers," *Nanotechnology*, vol. 26, no. 27, 2015, Art. no. 274001.

[164] I. Liberal, I. Ederra, R. Gonzalo, and R. W. Ziolkowski, "Superbackscattering antenna arrays," *IEEE Trans. Antennas Propag.*, vol. 63, no. 5, pp. 2011–2021, May 2015.

[165] D. Dobrykh *et al.*, "Multipole engineering for enhanced backscattering modulation," *Phys. Rev. B, Condens. Matter*, vol. 102, no. 19, 2020, Art. no. 195129.

[166] W. Lin and R. W. Ziolkowski, "Theoretical analysis of beam-steerable, broadside-radiating Huygens dipole antenna arrays and experimental verification of an ultrathin prototype for wirelessly powered IoT applications," *IEEE Open J. Antennas Propag.*, vol. 2, pp. 954–967, 2021.

[167] C. W. Oseen, "Die einsteinsche nadelstichstrahlung und die Maxwellschen Gleichungen," *Ann. Phys.*, vol. 374, no. 19, pp. 202–204, 1922.

[168] R. W. Ziolkowski, "Using Huygens multipole arrays to realize uni-directional needle-like radiation," *Phys. Rev. X*, vol. 7, no. 3, 2017, Art. no. 031017.

[169] S. Arslanagić and R. W. Ziolkowski, "Highly subwavelength, superdirective cylindrical nanoantenna," *Phys. Rev. Lett.*, vol. 120, no. 23, 2018, Art. no. 237401.

[170] V. Rumsey, "Some new forms of Huygens' principle," *IRE Trans. Antennas Propag.*, vol. 7, no. 5, pp. S103–S116, Dec. 1959.

[171] W. Chen, J. Fu, Q. Wu, and B. Lv, "Design principle of cylindrical superdirective antenna," *J. Phys. D Appl. Phys.*, vol. 52, no. 49, 2019, Art. no. 495102.

[172] W. Chen, J. Fu, B. Lv, and Q. Wu, "Novel optimizing algorithm of superdirective multi-layered cylindric antenna," *J. Phys. D Appl. Phys.*, vol. 53, no. 40, 2020, Art. no. 405105.

[173] W. Chen, J. Fu, and Q. Wu, "Enhanced superdirectivity of a multi-layered cylinder using a Huygens excitation," *J. Phys. D Appl. Phys.*, vol. 54, no. 2, 2020, Art. no. 025106.

[174] W. Chen, J. Fu, B. Lv, and Q. Wu, "Design of easy-manufacturing superdirective antenna: A theoretical study," *Appl. Opt.*, vol. 59, no. 27, pp. 8302–8309, Sep. 2020.

[175] I. Sushencev, A. A. Shcherbakov, K. Ladutenko, and P. Belov, "Superdirective dielectric spherical multilayer antennae," in *Proc. IEEE Int. Conf. Microw. Antennas Commun. Electron. Syst. (COMCAS)*, Nov. 2019, pp. 1–3.

[176] R. Gaponenko, A. Moroz, I. L. Rasskazov, K. Ladutenko, A. Shcherbakov, and P. Belov, "Harnessing superdirectivity in dielectric spherical multilayer antennas," *Phys. Rev. B, Condens. Matter*, vol. 104, no. 19, 2021, Art. no. 195406.

[177] C. A. Balanis, *Advanced Engineering Electromagnetics*. Hoboken, NJ, USA: Wiley, 1999.

[178] M. Abramowitz and I. A. Stegun, *Handbook of Mathematical Functions*. New York, NY, USA: Dover Publ., 1965.

[179] L. Schwartz, *Mathematics for the Physical Sciences*. Reading, MA, USA: Addison-Wesley, 1966.

[180] H. B. G. Casimir and G. Puppi, *On Supergain Antennae*. Cambridge, MA, USA: Academic, 1968, pp. 73–79.

[181] J. A. Wheeler, *Semiclassical Analysis Illuminates the Connection Between Potential and Bound States and Scattering*. Princeton, NJ, USA: Princeton Univ. Press, 1976, pp. 390–391.

[182] W. W. Hansen and J. R. Woodyard, "A new principle in directional antenna design," *Proc. Inst. Radio Eng.*, vol. 26, no. 3, pp. 333–345, Mar. 1938.

[183] S. A. Schelkunoff, "A mathematical theory of linear arrays," *Bell Syst. Tech. J.*, vol. 22, no. 1, pp. 80–107, Jan. 1943.

[184] L. La Paz and G. A. Miller, "Optimum current distributions on vertical antennas," *Proc. Inst. Radio Eng.*, vol. 31, no. 5, pp. 214–232, May 1943.

[185] C. J. Bouwkamp and N. G. De Bruijn, "The problem of optimum antenna current distribution," *Philips Res. Rep*, vol. 1, no. 2, pp. 135–158, 1946.

[186] C. L. Dolph, "A current distribution for broadside arrays which optimizes the relationship between beam width and side-lobe level," *Proc. Inst. Radio Eng.*, vol. 34, no. 6, pp. 335–348, Jun. 1946.

[187] C. L. Dolph, "Discussion on 'a current distribution for broadside arrays which optimizes the relationship between beam width and side-lobe level,'" *Proc. Inst. Radio Eng.*, vol. 35, no. 5, pp. 489–492, May 1947.

[188] H. J. Riblet, "Note on the maximum directivity of an antenna," *Proc. Inst. Radio Eng.*, vol. 36, no. 5, pp. 620–623, May 1948.

[189] N. Yaru, "A note on super-gain antenna arrays," *Proc. Inst. Radio Eng.*, vol. 39, no. 9, pp. 1081–1085, Sep. 1951.

[190] G. A. Deschamps and H. S. Cabayan, "Antenna synthesis and solution of inverse problems by regularization methods," *IEEE Trans. Antennas Propag.*, vol. AP-20, no. 3, pp. 268–274, May 1972.

[191] Y. T. Lo, S. W. Lee, and Q. H. Lee, "Optimization of directivity and signal-to-noise ratio of an arbitrary antenna array," *Proc. IEEE*, vol. 54, no. 8, pp. 1033–1045, Aug. 1966.

[192] D. K. Cheng, "Optimization techniques for antenna arrays," *Proc. IEEE*, vol. 59, no. 12, pp. 1664–1674, Dec. 1971.

[193] D. Margetis, G. Fikioris, J. M. Myers, and T. T. Wu, "Highly directive current distributions: General theory," *Phys. Rev. E, Stat. Phys. Plasmas Fluids Relat. Interdiscip. Top.*, vol. 58, no. 2, pp. 2531–2547, 1998.

[194] E. Shamonina, K. H. Ringhofer, and L. Solymar, "Configurations optimizing the directivity of planar arrays," *AEU Int. J. Electron. Commun.*, vol. 56, no. 2, pp. 115–119, 2002.

[195] M. Gustafsson and S. Nordebo, "Optimal antenna currents for Q, superdirectivity, and radiation patterns using convex optimization," *IEEE Trans. Antennas Propag.*, vol. 61, no. 3, pp. 1109–1118, Mar. 2013.

[196] G. T. Di Francia, "Super-gain antennas and optical resolving power," *Il Nuovo Cimento*, vol. 9, pp. 426–438, May 2008.

[197] A. M. H. Wong and G. V. Eleftheriades, "Superdirectivity-based superoscillatory waveform design: A practical path to far-field sub-diffraction imaging," in *Proc. 8th Eur. Conf. Antennas Propag. (EuCAP)*, 2014, pp. 1340–1344.

[198] M. L. Morris, M. A. Jensen, and J. W. Wallace, "Superdirectivity in MIMO systems," *IEEE Trans. Antennas Propag.*, vol. 53, no. 9, pp. 2850–2857, Sep. 2005.

[199] N. W. Bikhazi and M. A. Jensen, "The relationship between antenna loss and superdirectivity in MIMO systems," *IEEE Trans. Wireless Commun.*, vol. 6, no. 5, pp. 1796–1802, May 2007.

[200] T.-I. Lee and Y. E. Wang, "A planar multipolar antenna for MIMO applications," in *Proc. IEEE Antennas Propag. Soc. Int. Symp.*, 2007, pp. 2429–2432.

[201] T.-I. Lee and Y. E. Wang, "Mode-based information channels in closely coupled dipole pairs," *IEEE Trans. Antennas Propag.*, vol. 56, no. 12, pp. 3804–3811, Dec. 2008.

[202] R. C. Hansen, "Fundamental limitations in antennas," *Proc. IEEE*, vol. 69, no. 2, pp. 170–182, Feb. 1981.

[203] R. C. Hansen, "Some new calculations on antenna superdirectivity," *Proc. IEEE*, vol. 69, no. 10, pp. 1365–1366, Oct. 1981.

[204] "COMSOL Multi-Physics." Aug. 23, 2021. [Online]. Available: https://www.comsol.com/

[205] R. W. Ziolkowski, P. Jin, and C.-C. Lin, "Metamaterial-inspired engineering of antennas," *Proc. IEEE*, vol. 99, no. 10, pp. 1720–1731, Oct. 2011.

[206] P. Jin and R. W. Ziolkowski, "Metamaterial-inspired, electrically small Huygens sources," *IEEE Antennas Wireless Propag. Lett.*, vol. 9, pp. 501–505, 2010.

[207] R. W. Ziolkowski, "Low profile, broadside radiating, electrically small Huygens source antennas," *IEEE Access*, vol. 3, pp. 2644–2651, 2015.

[208] M.-C. Tang, H. Wang, and R. W. Ziolkowski, "Design and testing of simple, electrically small, low-profile, Huygens source antennas with broadside radiation performance," *IEEE Trans. Antennas Propag.*, vol. 64, no. 11, pp. 4607–4617, Nov. 2016.

[209] M.-C. Tang, T. Shi, and R. W. Ziolkowski, "Electrically small, broadside radiating Huygens source antenna augmented with internal non-Foster elements to increase its bandwidth," *IEEE Antennas Wireless Propag. Lett.*, vol. 16, pp. 712–715, 2016.

[210] M.-C. Tang, T. Shi, and R. W. Ziolkowski, "A study of 28 GHz, planar, multilayered, electrically small, broadside radiating, Huygens source antennas," *IEEE Trans. Antennas Propag.*, vol. 65, no. 12, pp. 6345–6354, Dec. 2017.

[211] M.-C. Tang, B. Zhou, and R. W. Ziolkowski, "Low-profile, electrically small, Huygens source antenna with pattern-reconfigurability that covers the entire azimuthal plane," *IEEE Trans. Antennas Propag.*, vol. 65, no. 3, pp. 1063–1072, Mar. 2017.

[212] M.-C. Tang, Y. Duan, Z. Wu, X. Chen, M. Li, and R. W. Ziolkowski, "Pattern reconfigurable, vertically polarized, low-profile, compact, near-field resonant parasitic antenna," *IEEE Trans. Antennas Propag.*, vol. 67, no. 3, pp. 1467–1475, Mar. 2019.

[213] M.-C. Tang, Z. Wu, T. Shi, and R. W. Ziolkowski, "Electrically small, low-profile, planar, Huygens dipole antenna with quad-polarization diversity," *IEEE Trans. Antennas Propag.*, vol. 66, no. 12, pp. 6772–6780, Dec. 2018.

[214] M. Tang, Z. Wu, T. Shi, H. Zeng, W. Lin, and R. W. Ziolkowski, "Dual-linearly polarized, electrically small, low-profile, broadside radiating, Huygens dipole antenna," *IEEE Trans. Antennas Propag.*, vol. 66, no. 8, pp. 3877–3885, Aug. 2018.

[215] W. Lin and R. W. Ziolkowski, "Electrically small, low-profile, Huygens circularly polarized antenna," *IEEE Trans. Antennas Propag.*, vol. 66, no. 2, pp. 636–643, Feb. 2018.

[216] R. W. Ziolkowski, "Custom-designed electrically small Huygens dipole antennas achieve efficient, directive emissions into air when mounted on a high permittivity block," *IEEE Access*, vol. 7, pp. 163365–163383, 2019.

[217] M. Tang, Z. Wu, T. Shi, and R. W. Ziolkowski, "Dual-band, linearly polarized, electrically small Huygens dipole antennas," *IEEE Trans. Antennas Propag.*, vol. 67, no. 1, pp. 37–47, Jan. 2019.

[218] W. Lin, R. W. Ziolkowski, and J. Huang, "Electrically small, low-profile, highly efficient, Huygens dipole rectennas for wirelessly powering Internet-of-Things devices," *IEEE Trans. Antennas Propag.*, vol. 67, no. 6, pp. 3670–3679, Jun. 2019.

[219] Z. Wu, M. Tang, T. Shi, and R. W. Ziolkowski, "Two-port, dual-circularly polarized, low-profile broadside-radiating electrically small Huygens dipole antenna," *IEEE Trans. Antennas Propag.*, vol. 69, no. 1, pp. 514–519, Jan. 2021.

[220] W. Lin and R. W. Ziolkowski, "Electrically small Huygens antenna-based fully-integrated wireless power transfer and communication system," *IEEE Access*, vol. 7, pp. 39762–39769, 2019.

[221] W. Lin and R. W. Ziolkowski, "Wirelessly powered light and temperature sensors facilitated by electrically small omnidirectional and Huygens dipole antennas," *Sensors*, vol. 19, no. 9, p. 1998, Apr. 2019.

[222] Z. Wu, M. Tang, M. Li, and R. W. Ziolkowski, "Ultralow-profile, electrically small, pattern-reconfigurable metamaterial-inspired Huygens dipole antenna," *IEEE Trans. Antennas Propag.*, vol. 68, no. 3, pp. 1238–1248, Mar. 2020.

[223] W. Lin and R. W. Ziolkowski, "Electrically small Huygens CP rectenna with a driven loop element maximizes its wireless power transfer efficiency," *IEEE Trans. Antennas Propag.*, vol. 68, no. 1, pp. 540–545, Jan. 2020.

[224] W. Lin and R. W. Ziolkowski, "Electrically small, single-substrate Huygens dipole rectenna for ultracompact wireless power transfer applications," *IEEE Trans. Antennas Propag.*, vol. 69, no. 2, pp. 1130–1134, Feb. 2021.

[225] R. W. Ziolkowski, "AWE-inspiring electrically small antennas," *Rev. Electromagn.*, vol. 1, no. 1, pp. 1–29, Jun. 2021.

[226] K.-M. Luk and H. Wong, "A new wideband unidirectional antenna element," *Int. J. Microw. Opt. Technol.*, vol. 1, no. 1, pp. 35–44, 2006.

[227] K.-M. Luk and B. Wu, "The magnetoelectric dipole—A wideband antenna for base stations in mobile communications," *Proc. IEEE*, vol. 100, no. 7, pp. 2297–2307, Jul. 2012.

[228] H.-J. Seo and A. A. Kishk, "Wideband magnetic-electric antenna with linear single OR dual polarization," *Prog. Electromagn. Res.*, vol. 155, pp. 53–61, Mar. 2016.

[229] M. Li, K. Luk, L. Ge, and K. Zhang, "Miniaturization of magneto-electric dipole antenna by using metamaterial loading," *IEEE Trans. Antennas Propag.*, vol. 64, no. 11, pp. 4914–4918, Nov. 2016.

[230] F. Wu and K. M. Luk, "A compact and reconfigurable circularly polarized complementary antenna," *IEEE Antennas Propag. Mag.*, vol. 16, pp. 1188–1191, 2017.

[231] J. Ouyang, Y. Pan, S. Zheng, and P. Hu, "An electrically small planar quasi-isotropic antenna," *IEEE Antennas Wireless Propag. Lett.*, vol. 17, no. 2, pp. 303–306, Feb. 2018.

[232] W. Lin, R. W. Ziolkowski, and T. C. Baum, "28 GHz compact omnidirectional circularly polarized antenna for device-to-device communications in the future 5G systems," *IEEE Trans. Antennas Propag.*, vol. 65, no. 12, pp. 6904–6914, Dec. 2017.

[233] R. Rodriguez-Cano and R. W. Ziolkowski, "Single-layer, unidirectional, broadside-radiating planar quadrupole antenna for 5G IoT applications," *IEEE Trans. Antennas Propag.*, vol. 69, no. 9, pp. 5524–5533, Sep. 2021.

[234] T. Suzuki and H. Asada, "Reflectionless zero refractive index meta-surface in the terahertz waveband," *Opt. Exp.*, vol. 28, no. 15, pp. 21509–21521, Jul. 2020.

[235] A. I. Uzkov, "An approach to the problem of optimum directive antenna design," *Doklady Akademii Nauk SSSR*, vol. 53, no. 1, pp. 35–38, 1946.

[236] E. E. Altshuler, T. H. O'Donnell, A. D. Yaghjian, and S. R. Best, "A monopole superdirective array," *IEEE Trans. Antennas Propag.*, vol. 53, no. 8, pp. 2653–2661, Aug. 2005.

[237] A. D. Yaghjian, T. H. O'Donnell, E. E. Altshuler, and S. R. Best, "Electrically small supergain end-fire arrays," *Rad. Sci.*, vol. 43, no. 3, pp. 1–13, Jun. 2008.

[238] S. R. Best, E. E. Altshuler, A. D. Yaghjian, J. M. McGinthy, and T. H. O'Donnell, "An impedance-matched 2-element superdirective array," *IEEE Antennas Wireless Propag. Lett.*, vol. 7, pp. 302–305, 2008.

[239] A. D. Yaghjian, "Increasing the supergain of electrically small antennas using metamaterials," in *Proc. 3rd Eur. Conf. Antennas Propag.*, 2009, pp. 858–860.

[240] T. Kokkinos and A. P. Feresidis, "Electrically small superdirective endfire arrays of metamaterial-inspired low-profile monopoles," *IEEE Antennas Wireless Propag. Lett.*, vol. 11, pp. 568–571, 2012.

[241] A. Clemente, M. Pigeon, L. Rudant, and C. Delaveaud, "Design of a super directive four-element compact antenna array using spherical wave expansion," *IEEE Trans. Antennas Propag.*, vol. 63, no. 11, pp. 4715–4722, Nov. 2015.

[242] A. Debard, A. Clemente, C. Delaveaud, P. Potier, and P. Pouliguen, "Limitations and optimization of supergain end-fire arrays," in *Proc. 13th Eur. Conf. Antennas Propag. (EuCAP)*, 2019, pp. 1–4.

[243] D. K. Cheng and F. I. Tseng, "Gain optimization for arbitrary antenna arrays," *IEEE Trans. Antennas Propag.*, vol. 13, no. 6, pp. 973–974, Nov. 1965.

[244] R. J. Mailloux, *Phased Array Antenna Handbook*, 2nd ed. Boston, MA, USA: Artech House, 2017.

[245] D. K. Cheng and F. I. Tseng, "Maximisation of directive gain for circular and elliptical arrays," *Proc. Inst. Electr. Eng.*, vol. 114, no. 5, pp. 589–594, 1967.

[246] E. Newman, J. Richmond, and C. Walter, "Superdirective receiving arrays," *IEEE Trans. Antennas Propag.*, vol. AP-26, no. 5, pp. 629–635, Sep. 1978.

[247] D. Vovchuk, S. Kosulnikov, R. E. Noskov, and P. Ginzburg, "Wire resonator as a broadband Huygens superscatterer," *Phys. Rev. B, Condens. Matter*, vol. 102, no. 9, 2020, Art no. 094304.

[248] R. Harrington, "Antenna excitation for maximum gain," *IEEE Trans. Antennas Propag.*, vol. AP-13, no. 6, pp. 896–903, Nov. 1965.

[249] Y. Ma, Y. Yang, Z. He, K. Yang, C. Sun, and Y. Wang, "Theoretical and practical solutions for high-order superdirectivity of circular sensor arrays," *IEEE Trans. Ind. Electron.*, vol. 60, no. 1, pp. 203–209, Jan. 2013.

[250] C. W. Hsu, B. Zhen, A. D. Stone, J. D. Joannopoulos, and M. Soljačić, "Bound states in the continuum," *Nat. Rev. Mater.*, vol. 1, no. 9, pp. 1–13, 2016.

[251] K. Koshelev, A. Bogdanov, and Y. Kivshar, "Engineering with bound states in the continuum," *Opt. Photon. News*, vol. 31, no. 1, pp. 38–45, Jan. 2020.

[252] P. M. Kamiński, R. W. Ziolkowski, and S. Arslanagić, "Riemann-Hilbert technique scattering analysis of metamaterial-based asymmetric 2D open resonators," *EPJ Appl. Metamater.*, vol. 4, p. 14, Dec. 2017.

[253] T. Sarkar and S. Rao, "A simple technique for solving E-field integral equations for conducting bodies at internal resonances," *IEEE Trans. Antennas Propag.*, vol. AP-30, no. 6, pp. 1250–1254, Nov. 1982.

[254] A. F. Peterson, "The 'interior resonance' problem associated with surface integral equations of electromagnetics: Numerical consequences and a survey of remedies," *Electromagnetics*, vol. 10, no. 3, pp. 293–312, 1990.

[255] F. X. Canning, "Protecting EFIE-based scattering computations from effects of interior resonances," *IEEE Trans. Antennas Propag.*, vol. 39, no. 11, pp. 1545–1552, Nov. 1991.

[256] A. F. Peterson, S. L. Ray, and R. Mittra, *Computational Methods for Electromagnetics*. Hoboken, NJ, USA: IEEE-Wiley Press, 1998.

[257] Z. Wu and R. Ziolkowski, "Electromagnetic effects associated with a cavity-backed aperture loaded with nonlinear elements," *Progr. Electromagn. Res.*, vol. 28, pp. 1–16, May 2000.

[258] J. van Bladel, *Singular Electromagnetic Fields and Sources*. Hoboken, NJ, USA: IEEE-Wiley Press, 1991, ch. 4.

[259] A. E. Krasnok, C. R. Simovski, P. A. Belov, and Y. S. Kivshar, "Superdirective dielectric nanoantennas," *Nanoscale*, vol. 6, no. 13, pp. 7354–7361, 2014.

[260] A. E. Krasnok, D. S. Filonov, C. R. Simovski, Y. S. Kivshar, and P. A. Belov, "Experimental demonstration of superdirective dielectric antenna," *Appl. Phys. Lett.*, vol. 104, no. 13, 2014, Art. no. 133502.

[261] S. Arslanagic and R. W. Ziolkowski, "Passive and active nano cylinders for enhanced and directive radiation and scattering phenomena," in *Proc. Nanoantennas Plasmonics Model. Design Fabrication*, 2020, pp. 53–102.

[262] M. Boyuan, J. Pan, S. Huang, D. Yang, and Y.-X. Guo, "Unidirectional dielectric resonator antennas employing electric and magnetic dipole moments," *IEEE Trans. Antennas Propag.*, vol. 69, no. 10, pp. 6918–6923, Oct. 2021.

[263] C. Chang, Y. Qian, and T. Itoh, "Analysis and applications of uniplanar compact photonic bandgap structures," *Progr. Electromagn. Res.*, vol. 41, pp. 211–235, 2003. [Online]. Available: https://www.jpier.org/PIER/pier41/09.02010890.Chang.QI_PI.pdf

[264] A. P. Feresidis, G. Goussetis, S. Wang, and J. C. Vardaxoglou, "Artificial magnetic conductor surfaces and their application to low-profile high-gain planar antennas," *IEEE Trans. Antennas Propag*, vol. 53, no. 1, pp. 209–215, Jan. 2005.

[265] A. Erentok, P. L. Luljak, and R. W. Ziolkowski, "Characterization of a volumetric metamaterial realization of an artificial magnetic conductor for antenna applications," *IEEE Trans. Antennas Propag*, vol. 53, no. 1, pp. 160–172, Jan. 2005.

[266] L. Vincelj, S. Hrabar, and R. Ziolkowski, "Non-Foster self-oscillating Huygens radiator," in *Proc. IEEE Int. Symp. Antennas Propag. North Amer. Radio Sci. Meeting*, Montreal, QC, Canada, Jul. 2020, pp. 521–522.

[267] L. Vincelj, R. W. Ziolkowski, and S. Hrabar, "Experimental demonstration of non-Foster self-oscillating Huygens radiator," in *Proc. 14th Int. Congr. Artif. Mater. Novel Wave Phenomena (Metamaterials)*, New York, NY, USA, Sep./Oct. 2020, pp. 508–510.

[268] R. Alvarez, E. Lauer, D. Birx, D. Scalapino, and D. Byrne, "Application of microwave energy compression to particle accelerators," *Part. Accel.*, vol. 11, no. 3, pp. 125–130, 1981.

[269] Z. Farkas, "RF energy compressor," in *IEEE MTT-S Int. Microw. Symp. Dig.*, May 1980, pp. 84–86.

[270] R. Alvarez, "Microwave energy storage in resonant cavities," Lawrence Livermore Nat. Lab., Livermore, CA, USA, Rep. UCID-19696, 1983.

RICHARD W. ZIOLKOWSKI (Life Fellow, IEEE) received the B.Sc. degree *(magna cum laude)* (Hons.) in physics from Brown University, Providence, RI, USA, in 1974, the M.S. and Ph.D. degrees in physics from the University of Illinois at Urbana–Champaign, Urbana, IL, USA, in 1975 and 1980, respectively, and the Honorary Doctorate degree from the Technical University of Denmark, Kongens Lyngby, Denmark, in 2012.

He is currently a Distinguished Professor with the Global Big Data Technologies Centre, Faculty of Engineering and Information Technologies (FEIT), University of Technology Sydney, Ultimo, NSW, Australia. He became a Professor Emeritus with the University of Arizona in 2018, where he was a Litton Industries John M. Leonis Distinguished Professor with the Department of Electrical and Computer Engineering, College of Engineering and was also a Professor with the College of Optical Sciences. He was the Computational Electronics and Electromagnetics Thrust Area Leader with the Engineering Research Division, Lawrence Livermore National Laboratory before joining the University of Arizona, Tucson, AZ, USA, in 1990. His current research interests include the application of new mathematical and numerical methods to linear and nonlinear problems dealing with the interaction of electromagnetic and acoustic waves with complex linear and nonlinear media, as well as metamaterials, metamaterial-inspired structures, nano-structures, and other classical and quantum applications-specific configurations.

Prof. Ziolkowski was the recipient of the 2019 IEEE Electromagnetics Award (IEEE Technical Field Award). He was the 2014–2015 Australian DSTO Fulbright Distinguished Chair in Advanced Science and Technology. He served as the President of the IEEE Antennas and Propagation Society (AP-S) in 2005 and has had many other AP-S leadership roles. He is also actively involved with the International Union of Radio Science, the European Association on Antennas and Propagation, and the International Society for Optics and Photonics professional societies. He became a Fellow of Optica (formerly, the Optical Society of America, OSA) in 2006 and the American Physical Society in 2016.